Cal Poly

Caltech

SCEC
AN NSF+USGS CENTER

UC Irvine

UCLA

UC Santa Barbara

USC

Comparison of FDHI Fault Displacement Models

Alexandra Sarmiento, P.E., C.E.G.
University of California, Los Angeles

Grigorios Lavrentiadis, Ph.D.
University of California, Los Angeles
California Institute of Technology

Yousef Bozorgnia, Ph.D., P.E., F.ASCE
University of California, Los Angeles

Rui Chen, Ph.D., P.G.
California Geological Survey

Brian S.J. Chiou, Ph.D.
California Department of Transportation

Timothy E. Dawson, C.E.G.
California Geological Survey

Albert Kottke, Ph.D., P.E.
Pacific Gas & Electric Company

Nicolas Kuehn, Ph.D.
University of California, Los Angeles

Chun-Hsiang Kuo, Ph.D.
National Central University
National Center for Research on Earthquake Engineering

Chris Madugo, Ph.D.
Pacific Gas & Electric Company

Christopher W.D. Milliner, Ph.D.
California Institute of Technology

Robb Moss, Ph.D., P.E., F.ASCE
California Polytechnic State University

Kate Thomas
California Geological Survey

Stephen Thompson, Ph.D., C.E.G.
Lettis Consultants International

Yongfei Wang, Ph.D.
Southern California Earthquake Center

Kourosh Younesi, Ph.D., P.E.
Science and Research Branch of Azad University

Arash Zandieh, Ph.D., P.E.
Lettis Consultants International

A report on research conducted with support from Pacific Gas & Electric Company, California High-Speed Rail Authority, California Department of Transportation, Southern California Gas Company, Los Angeles Department of Water and Power, and California Energy Commission.

Report Report GIRS-2022-10
DOI: 10.34948/N3W88V

University of California, Los Angeles (headquarters)

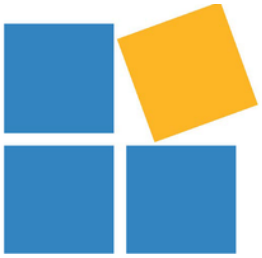

Natural Hazards Risk & Resiliency Research Center

The B. John Garrick Institute for the Risk Sciences

Comparison of FDHI Fault Displacement Models

Alexandra Sarmiento, P.E., C.E.G.
University of California, Los Angeles

Grigorios Lavrentiadis, Ph.D.
University of California, Los Angeles
California Institute of Technology

Yousef Bozorgnia, Ph.D., P.E., F.ASCE
University of California, Los Angeles

Rui Chen, Ph.D., P.G.
California Geological Survey

Brian S.J. Chiou, Ph.D.
California Department of Transportation

Timothy E. Dawson, C.E.G.
California Geological Survey

Albert Kottke, Ph.D., P.E.
Pacific Gas & Electric Company

Nicolas Kuehn, Ph.D.
University of California, Los Angeles

Chun-Hsiang Kuo, Ph.D.
National Central University
National Center for Research on Earthquake Engineering

Chris Madugo, Ph.D.
Pacific Gas & Electric Company

Christopher W.D. Milliner, Ph.D.
California Institute of Technology

Robb Moss, Ph.D., P.E., F.ASCE
California Polytechnic State University

Kate Thomas
California Geological Survey

Stephen Thompson, Ph.D., C.E.G.
Lettis Consultants International

Yongfei Wang, Ph.D.
Southern California Earthquake Center

Kourosh Younesi, Ph.D., P.E.
Science and Research Branch of Azad University

Arash Zandieh, Ph.D., P.E.
Lettis Consultants International

A report on research conducted with support from Pacific Gas & Electric Company, California High-Speed Rail Authority, California Department of Transportation, Southern California Gas Company, Los Angeles Department of Water and Power, and California Energy Commission.

Report GIRS-2022-10

Natural Hazards Risk and Resiliency Research Center
The B. John Garrick Institute for the Risk Sciences
University of California, Los Angeles (Headquarters)

April 2023

ABSTRACT

This report presents comparisons between four new fault displacement amplitude prediction models that were developed through the Fault Displacement Hazard Initiative (FDHI) Project. The comparisons focus on displacements occurring on principal surface ruptures. Three previously published principal fault displacement models commonly used in engineering practice are also included in the comparison with the new models. The new Fault Displacement Models (FDMs) are a significant improvement over existing models in several ways. All FDHI models were developed using a database of 75 events that underwent an extensive and systematic data quality review in coordination with the model developers. The new FDMs also use advanced statistical modeling which, in most cases, includes magnitude scaling breakpoints, separation of between- and within-event aleatory components that are magnitude- and location-dependent, and within-model epistemic uncertainty. Two of the new models are applicable to all styles of faulting, while the other two models are for strike-slip and reverse events, respectively. All new models are applicable between **M** 6.0 and 8.0, where most of the empirical data exist, but some are applicable to lower or higher magnitudes. Similar to previously published models, the new FDMs use earthquake size and normalized position along the rupture as predictor variables.

The quantitative comparisons in this report capture a broad range of scenarios defined by style of faulting, magnitude, normalized rupture position, and predicted percentile. The median predictions in the new models generally vary by a factor of two to three for $\mathbf{M} \geq 6$ for any given normalized position along the rupture and all styles of faulting. The largest differences generally occur at the rupture endpoints, regardless of style of faulting, and at small magnitudes for strike-slip and normal faulting. These differences can be attributed to areas where empirical data are limited or incomplete. Similarly, the new models are most similar for magnitudes that are well-represented in the FDHI Database. For example, median predictions are within a factor of 1.5 for **M** 7.0 strike-slip earthquakes and $\mathbf{M} \leq 6.5$ for reverse events, and within a factor of 1.2 for **M** 7.0 normal events. Improved statistical modeling approaches in the new FDMs also capture the upper and lower tails of the data distributions better than previously published models. Compared to existing models, all new FDMs produce lower 95^{th} percentile predictions at the rupture midpoint for $\mathbf{M} \geq 7.2$ and all styles of faulting. The improved aleatory variability modeling in the FDHI fault displacement models makes them suited for probabilistic fault displacement hazard analysis extending to large return periods, which can be sensitive to the size of the aleatory variability.

ACKNOWLEDGMENTS

Support for this project was provided by the California Energy Commission, Pacific Gas & Electric Company, California High-Speed Rail Authority, California Department of Transportation, Southern California Gas Company, and Los Angeles Department of Water and Power. Multiple individuals and organizations were partners in this project, as is evident from the list of the authors of this report.

The support of these organizations is gratefully appreciated. The opinions, findings, conclusions, or recommendations expressed in this publication are those of the authors and do not necessarily reflect the views of the study sponsors, the Natural Hazards Risk and Resilience Research Center (NHR3), or the Regents of the University of California.

This work was completed through the Fault Displacement Hazard Initiative (FDHI) Project, which is a multi-year, community-based research program. The structured but cooperative nature of the FDHI Project provided a forum for fault displacement modeling teams and database developers to have extensive interactions and fruitful technical discussions, which resulted in higher quality models than each researcher could achieve individually. Acknowledgment and appreciation are given to over 40 researchers and practicing professionals who worked on various parts of the FDHI Project. Their contributions, dedication, and teamwork are greatly appreciated. We also thank Dr. Norman Abrahamson for suggestions and helpful discussions that improved this report.

CONTENTS

LIST OF FIGURES

LIST OF TABLES

1 Introduction

The Fault Displacement Hazard Initiative (FDHI) Project is a multi-year, community-based research project coordinated by the University of California. The objectives of the project are to (i) compile a comprehensive fault rupture and displacement database; and (ii) develop a set of next-generation fault rupture and displacement models. The new database is documented in a separate report available through the Natural Hazards Risk and Resiliency Research Center (NHR3) web site (Sarmiento et al., 2021). The database was compiled in coordination with the model developers, and all data were systematically and repeatedly reviewed for quality and content. Using the new empirical database, four research teams developed new fault displacement amplitude prediction models, which we refer to more generally as Fault Displacement Models (FDMs).

This report provides a comparison of the four new FDMs developed through the FDHI Project. For completeness, three previously published FDMs commonly used in engineering practice are also included in the comparisons. The new and existing FDMs are listed in Table 1.1. Many of the models have formulations for principal and distributed fault displacements; however, the comparisons in this study are for principal rupture displacements only. Technical reports for two of the new models have not been published yet, so Table 1.1 also lists the versioning for each model that served as the basis for the comparisons in this report. The new models will also be published in a peer-reviewed journal. Although the FDHI Project afforded regular interaction and participatory peer review between model development teams, some of the model details could change in response to the journal's peer review process.

We begin with an overview in Chapter 2 that describes the different displacement metrics used in the models and provides a general overview of the model formulations and parameters. Chapter 3 summarizes the data sets used in the development of each model and the recommended applicability ranges for each model. We then present median model predictions (Chapter 4) and compare the aleatory variability between the models for a set of scenarios in Chapter 5. Examples of within-model epistemic uncertainty are shown in Chapter 6, and the key results of this report are summarized in Chapter 7. As the purpose of this report is to compare FDMs, the results do not account for the conditional probability of surface rupture (e.g., Wells and Coppersmith, 1993). Fault Rupture Models (FRMs) that predict the probability of surface rupture are not evaluated in this study.

Table 1.1. Fault displacement models (FDMs) compared in this report.

Status	Model	Abbreviation[(1)]	Versioning
New	Moss et al. (2022)	MEA22	As-Published
New	Kuehn et al. (2022)	KEA22	As-Published
New	Chiou et al. (2022)	CEA22	October 2022[(2)]
New	Lavrentiadis and Abrahamson (2022)	LA22	October 2022[(3)]
Existing	Youngs et al. (2003)	YEA03	As-Published
Existing	Petersen et al. (2011)	PEA11	As-Published
Existing	Moss and Ross (2011)	MR11	As-Published

[(1)] The abbreviation "EA" (*et al.*) is used for models with more than two authors.
[(2)] Report submitted for NHR3 publication.
[(3)] Manuscript submitted for journal publication.

Median comparisons are shown for all magnitudes, normalized positions along rupture, and style of faulting. The aleatory and epistemic comparisons are provided for several scenarios defined by style of faulting, moment magnitude, and normalized position along rupture. While the range of scenarios considered herein is not exhaustive, it is broad enough to demonstrate similarities and differences between the models. Similar to the Next Generation Attenuation (NGA) Program's comparisons for ground motion models (Abrahamson et al., 2008; Gregor et al., 2014, 2022), we provide explanations of key differences, but detailed evaluations of the performance of each model are outside the scope of this report.

The FDHI Project facilitated extensive collaboration among geologists, earthquake engineers, model developers, practicing professionals, end-users, and sponsors. The collaboration occurred in monthly project meetings beginning in June 2018 and several topical working group meetings related to database development, model development, and model comparisons. Each new model team is also participating in the International Atomic Energy Agency (IAEA) probabilistic fault displacement hazard analysis (PFDHA) benchmarking study (Valentini et al., 2021). Detailed evaluations of model strengths and weaknesses conducted through the FDHI Project meetings and IAEA PFDHA benchmarking study informed the discussions and comparisons in this report.

2 Overview of Displacement Metrics and Model Formulations

This chapter provides necessary background to understand the models compared in this report. Displacement metrics are discussed first because not all models use the same metric. Second, a high-level overview of the functional forms and parameters used in the models is provided. The model equations, coefficients, and details on the model development are outside the scope of this discussion but can be found in the source publications listed in Table 1.1. Lastly, we identify which model formulations evaluated in this report because some model developers provide multiple FDMs for the same displacement metric.

2.1 DISPLACEMENT METRICS

Fault displacement amplitude models predict a specific displacement metric. We define *displacement metric* as the set of parameters that describe the type of displacement, and it is similar to the concept of an intensity measure in ground motion models (e.g., RotD50 vs. RotD100). The metric is based on the data used to develop the model, data analysis performed by the modelers, and recommendations from the model developers. For example, the data might be limited to a specific style of faulting, slip component, or type of rupture (e.g., principal or distributed), and the model developer might have post-processed the data to sum displacements on (sub)parallel ruptures. Understanding the displacement metric used by a FDM is necessary to correctly interpret and apply the results, compare results between models, and use alternative models to capture epistemic uncertainty.

The displacement metrics in the FDMs compared in this report are listed in Table 2.1. Most of the models that were developed for a specific style of faulting predict the associated slip component (e.g., the MR11 model was developed for reverse faulting and predicts vertical slip). Surface fault ruptures are commonly classified as principal or distributed (e.g., Coppersmith and Youngs, 2000; Stepp et al., 2001; Youngs et al., 2003; Petersen et al., 2011), and these are usually treated separately in modeling due to different underlying driving mechanisms or geologic structure. Although several model developers provide FDMs for multiple rupture types (viz.,

MEA22, LA22, YEA03, and PEA11), only those related to principal fault ruptures are evaluated in this report (Table 2.1).

Table 2.1. Summary of displacement metrics used in FDMs evaluated in this report.

Model	Style of Faulting[(1)]			Slip Component	Rupture Type
	SS	RV	NM		
MEA22	–	✓	–	Vertical	Principal*, Distributed
KEA22	✓	✓	✓	Net	Aggregated on Principal & Distributed
CEA22	✓	–	–	Net	Aggregated on Principal
LA22	✓	✓	✓	Net	Aggregated on Principal & Distributed*, Principal, Distributed
YEA03	–	–	✓	Vertical	Principal*, Distributed
PEA11	✓	–	–	Lateral	Principal*, Distributed
MR11	–	✓	–	Vertical	Principal

[(1)] SS = Strike-slip; RV = Reverse; NM = Normal.

* Rupture metric evaluated in this report when multiple FDMs are available.

The following sections describe the slip components and rupture types used in the FDMs (Table 2.1). Data set limitations related to the net slip component are summarized and an overview of displacements aggregated across (sub)parallel faults is provided. We note that because the models in Table 2.1 predict a range of displacement metrics, direct comparisons between all models are not possible, and practitioners should be aware of the displacement metrics used in a given model.

2.1.1 Slip Component

Figure 2.1 illustrates the slip vector components that accommodate fault displacement. The net component should be the vector sum of the lateral (fault-parallel), heave (fault-normal), and vertical components. However, the reporting of the slip component measurements in original data sets is commonly incomplete for several reasons. For instance, determining the net component requires reconstructing the pre-rupture configuration of the offset feature in three-dimensional space, which may not always be feasible. In particular, the fault-normal component is usually not reported when deformation is compressional because it is difficult to measure in the field due to the morphology produced by reverse faulting (e.g., hanging-wall collapse, broad warping), but it is often reported in extensional deformation where it is more easily measured. As well, field geology teams may prioritize measuring displacements for the associated style of faulting (e.g., vertical displacements for normal events). Consequently, data sets typically include measurements of either the lateral or vertical component at most sites; sites with measurements for both components are less common, and sites with fault-normal component measurements are rare.

The FDHI Database (Sarmiento et al., 2021) documents the measured slip component and amplitude. Net displacement amplitudes are also reported in the database and are based on the original data set when it is provided; otherwise, the values are calculated from the reported slip components. Approximately 10% of the net displacement values in the FDHI Database are from reported net slip measurements; however, when original data sets provide net displacement values, it is sometimes unclear if the fault-normal component is included or assumed to be nil, particularly for reverse events or measurements in areas of compressional deformation (e.g., restraining steps or bends in strike-slip earthquakes). When net displacement is not reported in original data sets, the values in the FDHI Database are calculated as the vector sum of the reported components. The calculation assumes the values of unreported components is zero and therefore may underestimate the true net displacement. (We note that the FDHI database does include flags for non-zero but unmeasured slip components, and the calculated net displacement values for these measurements are given a lower quality ranking.)

Most of the new FDMs use net slip (Table 2.1). However, it is important to note that the documentation of the net slip component may be incomplete, which can impact the models differently depending on the style of faulting. For example, it is generally more common for strike-slip event data sets to report both lateral and vertical components, and the fault-normal component is usually nil; therefore, net displacement calculations for strike-slip events are usually close to the true net displacement. For normal earthquakes, lateral and fault-normal components might be missing in some net displacement calculations. Finally, for reverse events, both lateral and fault-normal components are commonly under-reported and the calculated net displacement values in the FDHI Database may under-predict the true net displacement.

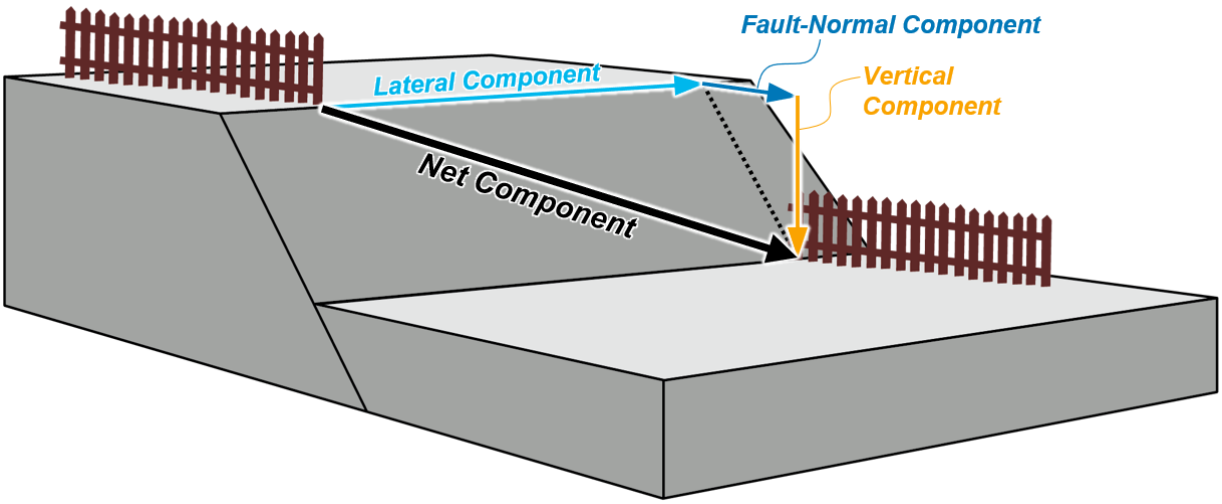

Figure 2.1. Fault displacement slip components. The FDMs predict net slip, lateral slip, or vertical slip components (varies by model). The fault-normal (heave) component is under-reported in empirical data sets; see text for discussion.

2.1.2 Aggregated Displacement

New approaches using displacements summed or aggregated across multiple (sub)parallel ruptures were developed through the FDHI Project. Aggregated displacement was viewed as a more stable metric by some modeler teams to account for effects that are not modeled, such as complex surface rupture patterns with multiple discontinuous or splayed ruptures due to event- and/or site-specific effects. Furthermore, the aggregated displacement approaches account for irregular spacing of displacement measurement sites, which is common in field data sets due to various geologic or logistic factors. The KEA22 model uses an "hourglass-shaped" search window for computing the aggregated value, and the LA22 and CEA22 models use a linear interpolation-based approach for the aggregation. As a result, most of the new models in Table 2.1 included a data pre-processing effort that aggregates displacements across (sub)parallel ruptures. Each team (KEA22, CEA22, and LA22) used a unique method to aggregate the displacements based on data in the FDHI Database.

Figure 2.2 shows a generic example of a pre-processing approach that generates an aggregated displacement value at a position along the nominal surface rupture trend. Using the shaded region on Figure 2.2 as an example, models that predict aggregated displacements would effectively sum the displacements on both principal faults in the shaded area and use this summed value in their model development. (Some models would also include the displacements from distributed ruptures; see Table 2.1.) The shape and dimensions of the shaded region vary between models, and distance limits on linear interpolation of displacements between measurement sites also vary between the models.

To better understand the impact of different displacement aggregation methodologies, an FDHI Working Group was convened to review results from different aggregation approaches for six earthquakes. The results and discussion are in Appendix A. In general, the Working Group found reasonable agreement between the three aggregation models, and we conclude that predictions between these three models (KEA22, CEA22, and LA22) can be compared directly. However, direct comparisons between models that predict aggregated and principal displacements are not possible, except for the LA22 model which provides formulations for both types. To provide a rough idea of the scaling between principal and aggregated displacements, we show the LA22 scaling model in Figure 2.3. The scaling is independent of earthquake size and site location. While the LA22 scaling model agrees well with the principal-to-aggregated displacement ratios for the six events evaluated in Appendix A, it is specific to the LA22 model and should not be applied to other models.

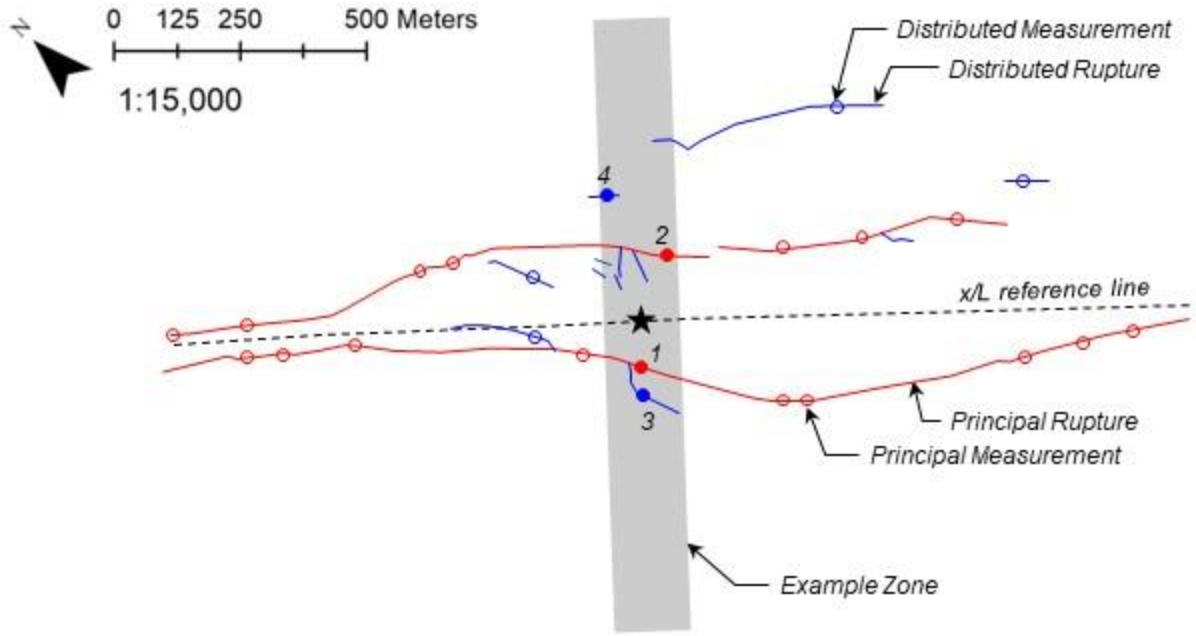

Figure 2.2. Example of generic displacement aggregation approach based on map of surface ruptures (lines) and displacement measurement sites (open and closed circles) from a fictitious earthquake. Star the is location of interest, and four measurement sites are within the shaded example zone. Reference line represents the nominal surface rupture trace for measuring position along rupture. See text for discussion on developing aggregated displacements in the shaded zone.

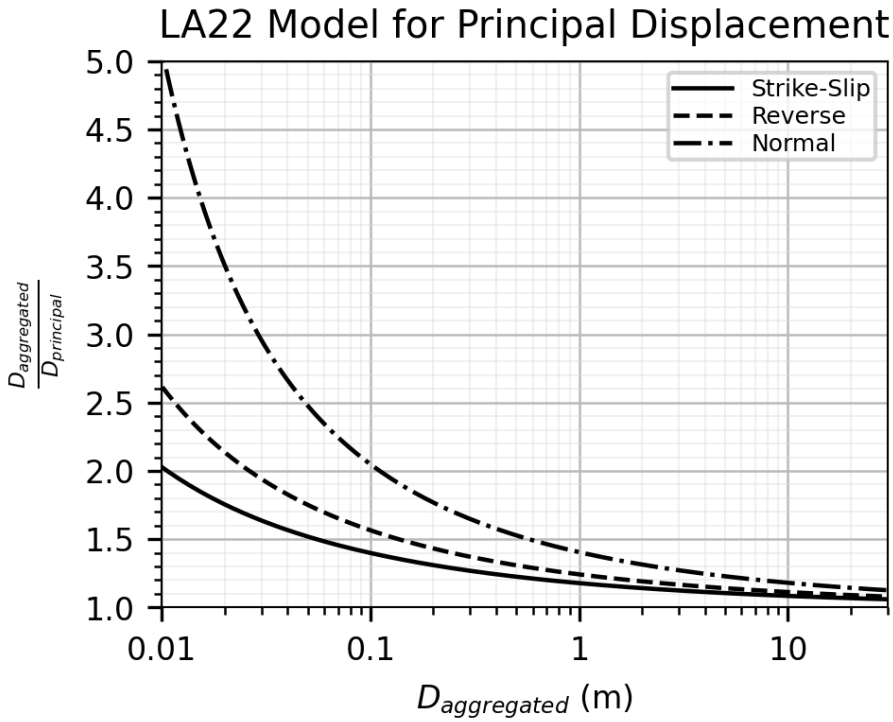

Figure 2.3. Aggregated-to-principal displacement scaling used in the LA22 model.

2.2 MODEL FORMULATIONS AND MODEL PARAMETERS

All FDMs predict displacement amplitude as a probability distribution based on earthquake size and position along the rupture. We use the terms *location scaling* to describe the relative relationship between displacement and the position along the strike of the rupture and *magnitude scaling* to describe the relationship between displacement amplitude and the size of the earthquake. Table 2.2 lists the parameters used in the scaling components of each model.

Location scaling describes the shape of the displacement profile and how the displacement amplitude changes along the rupture length. All models developed displacement profiles from each earthquake data set. Empirical displacement profiles present displacement amplitude as a function of length along the rupture or normalized position along the rupture (Figure 2.4). The normalized position x/L is a distance ratio, where x is the length along the surface rupture and L is the total surface rupture length. Previous studies have found displacement profiles are commonly asymmetric (Hemphill-Haley and Weldon, 1999; Manighetti et al., 2005; Wesnousky, 2008; Youngs et al., 2003). Because the skewness usually cannot be determined a priori, most of the new models predict profile functional forms that are symmetrical about the rupture midpoint ($x/L = 0.5$), which we refer to as *folded*. An exception is the KEA22 model, which used the full (*unfolded*)

normalized rupture length and systematically oriented displacement profiles with the peak left of the rupture midpoint in the model development. Additionally, the CEA22 model team provides an alternative unfolded formulation for applications where asymmetry is appropriate.

All models use some measure of earthquake size to adjust the amplitude of the median profile. The earthquake size is parameterized either (i) directly in the model formulation with moment magnitude or surface rupture length; or (ii) indirectly using a formulation that predicts a normalized displacement. In the latter case, the model is coupled with a scaling relationship for the normalization variable, which is typically the average displacement (AD) or the maximum displacement (MD), to capture the magnitude scaling. Table 2.2 summarizes the parameters used in each model. Most of the new models include a magnitude scaling breakpoint, whereas the existing models used linear magnitude scaling.

The aleatory variability in displacement amplitude is defined through the statistical distribution used in each model. Several different probability distributions are used in FDMs (e.g., lognormal, gamma, beta, and power-normal). Most new models partition the aleatory variability into between- and within-event components, and in most cases, the aleatory variability models are magnitude- and location-dependent. Separating the aleatory variability into between- and within-event components avoids bias towards better-sampled events. Including magnitude- and location-dependence in the aleatory variability models improves hazard estimates because data dispersion is not constant for all magnitudes or positions along the rupture. With the exception of KEA22, all FDMs use a folded normalized rupture position and therefore implicitly include aleatory variability from asymmetry in the empirical displacement profiles; however, the KEA22 authors recommend including the calculations for the complimentary position ($1 - x/L$) with equal weight because profile symmetry/asymmetry is not known a priori, which effectively treats asymmetry as aleatory variability by marginalizing over the location.

Within-model epistemic uncertainty is provided to some extent in all new models. In general, the uncertainty is characterized either with alternative model coefficients, quantified uncertainty on model predictions, or alternative model formulations. This is discussed in more detail in Chapter 6.

Table 2.2. Summary of model parameters for location and magnitude scaling model components.

Model Component	Parameter	MEA22	KEA22	CEA22	LA22	YEA03	PEA11	MR11
Location Scaling	Earthquake magnitude	–	–	–	✓	–	–	–
	Surface rupture length	–	–	–	✓	–	–	–
	Style of faulting	–	✓	–	✓	–	–	–
	Normalized position along rupture	✓	✓	✓	✓	✓	✓	✓
Magnitude Scaling	Earthquake magnitude	*	✓	✓	✓	*	✓	*
	Surface rupture length	–	–	–	✓	–	–	–
	Style of faulting	–	✓	–	✓	–	–	–

* Model predicts normalized displacement; magnitude is captured through scaling relationship for Average Displacement (AD) or Maximum Displacement (MD).

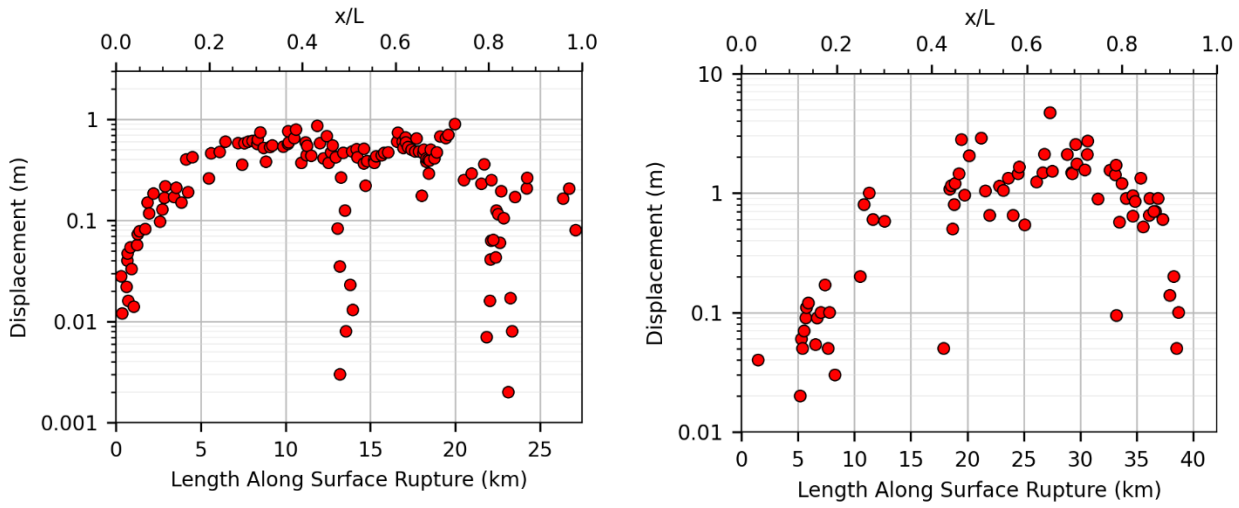

(a) 1987 **M** 6.54 Superstition Hills, California

(b) 1987 **M** 6.88 Borah Peak, Idaho

Figure 2.4. Example empirical displacement profiles showing principal displacements. Normalized distance ratio $\boldsymbol{x/L}$ is shown on top axis, where $\boldsymbol{x}$ is the length along the surface rupture and $\boldsymbol{L}$ is the total surface rupture length. Note rupture extends beyond measurements in the Borah Peak data set.

2.3 MODEL FORMULATIONS EVALUATED IN THIS REPORT

The comparisons in this study are for principal (or aggregated) displacements only. Several model developers provide alternative formulations for principal (or aggregated) displacements. For brevity, only one formulation from each model is evaluated in Chapter 4 (Median Value Comparisons) and Chapter 5 (Aleatory Variability Comparisons). The chosen formulation was the preferred approach identified in the model documentation or through personal communication with the model developers. Table 2.3 summarizes the models, displacement metrics, and specific formulations (i.e., statistical distributions) that are the focus of this report.

Table 2.3. Fault displacement model formulations compared in this report.

Model	Formulation[1]	Displacement Metric D [2]
MEA22	$D/MD \sim Gamma$	Principal, vertical slip
KEA22	$lnD \sim Normal$	Aggregated, net slip
CEA22	$lnD \sim nEMG$	Aggregated, net slip
LA22	$D^{0.3} \sim Normal$	Aggregated, net slip
YEA03	$D/AD \sim Gamma$	Principal, vertical slip
PEA11	$lnD \sim Normal$	Principal, lateral slip
MR11	$D/MD \sim Beta$	Principal, vertical slip

[1] Describes response variable and statistical distribution. Variables D, AD, and MD are displacement, average displacement, and maximum displacement, respectively. $nEMG$ is negative exponentially-modified Gaussian distribution.

[2] Definition of response variable D used in model formulation.

3 Data Set Selection and Model Applicability

This chapter summarizes the data sets used in the development of each model. Specifically, we summarize the number of events, number of measurements, and magnitude ranges for the model formulations evaluated in this report (Tables 1.1 and 2.1). Guidance on model applicability is provided at the end of this chapter.

3.1 DATA SET SELECTION

All four new FDMs used the FDHI Database (Sarmiento et al., 2021). The empirical database was developed in collaboration with earthquake geologists, model developers, engineering community end-users, and project sponsors through the FDHI Project. The primary goal of the database was to support the development of new FDMs by systematically collecting, reviewing, and organizing relevant data in a database. The database contains rupture traces and fault displacement measurements from 75 global historical surface-rupturing earthquakes. The earthquakes are from shallow crustal tectonic environments and include all styles of faulting.

The FDHI model development teams selected subsets of the FDHI database based on data selection criteria for their model. The specific criteria and justification for the excluded data are described in the respective model reports. Generally, model teams excluded events based on style of faulting (e.g., MEA22 and CEA22) or insufficient spatial distribution or number of displacement measurements. Individual measurements with low-quality flags were typically excluded, and some model developers selected one measurement data set when alternative data sets were available for the same event (e.g., the Hector Mine earthquake). Finally, the MEA22 model used the initial FDHI Database release dated August 2021, whereas the other new models used an expanded version that was released in July 2022 with nine additional earthquakes.

The location scaling component of the model development uses empirical displacement profiles (i.e., displacement amplitude as a function of position-along-rupture; Figure 2.4). The reference lines used to measure position-along-rupture can be based on manual or algorithmic interpretation of the rupture and/or displacement data. Manual efforts usually consist of a geologist determining the nominal rupture trace and projecting displacement measurements onto the trace. This approach can be subjective, especially when multiple (sub)parallel ruptures occur. Lavrentiadis et al. (2022a) and Thomas et al. (2022) recently developed automated methods to

remove or minimize subjectivity. The Event Coordinate System (ECS) algorithm by Lavrentiadis et al. (2022a) generates a reference line based on the spatial distribution of principal surface rupture traces and principal displacement measurement amplitudes. The Thomas et al. (2022) algorithm uses a least-cost path (LCP) analysis of the spatial distribution of surface rupture traces to create the reference line. Both methods use the second generalized coordinate system (GC2) by Spudich and Chiou (2015) to transform the event data into an along-strike dimension based on the reference line. The ECS coordinates are included in the FDHI Database.

Table 3.1 summarizes the data sets used for location scaling in the new and existing model formulations evaluated in this report. The new FDMs exclusively used the displacement measurements in the FDHI Database for location scaling. The existing models used various data sets. The CEA22 model (which only applies to strike-slip style of faulting) used the LCP-based reference line for the along-strike projection of displacements, whereas the other new models used the ECS. Preliminary sensitivity evaluations by G. Lavrentiadis (pers. comm.) and Chiou et al. (2022) found the surface rupture lengths derived from the ECS and LCP reference lines were similar for all strike-slip events, suggesting the impact of using different reference lines is small.

The data sets used for magnitude scaling are shown in Table 3.2. Three of the new FDMs (KEA22, CEA22, and LA22) exclusively used the data from the FDHI Database for magnitude scaling. The MEA22 model uses normalized displacement ratios to handle magnitude scaling, and the model developers elected to compile a separate data set of average and maximum displacement measurements for reverse events using the FDHI Database and other sources. Similarly, the MR11 and YEA03 FDMs also used different data sets for magnitude and location scaling. As a result, the data sets for the magnitude scaling are larger than those for location scaling in these models.

Table 3.1. Summary of data sets used in models for location scaling.

Model	Reference Line Basis	Style of Faulting[1]	N Events	Event **M** Range	N Measurements	Data Set
MEA22	ECS	RV/RVO	21	5.03 – 8.02	1038	FDHI
KEA22	ECS	SS	34	5.2 – 7.9	5446	FDHI
		RV/RVO	25	4.9 – 8.02	2113	
		NM/NMO	14	6.2 – 7.76	331	
CEA22	LCP	SS	29	6.0 – 7.9	3309	FDHI
LA22	ECS	SS	34	5.0 – 7.9	9107	FDHI
		RV/RVO	25	4.9 – 8.02	2681	
		NM/NMO	15	6.2 – 7.76	7904	
YEA03	Manual	NM/NMO	11	6.22 – 7.29	Not Reported	McCalpin and Slemmons (1998)
PEA11	Manual	SS	21	6.3 – 7.9	1666	Wesnousky (2008) subset, plus 9 PEA11 events
MR11	Manual	RV/RVO	9	5.4 – 7.9	Not Reported	Wesnousky (2008) subset, plus 1 MR11 event

(6) SS = Strike-slip; RV = Reverse; RVO = Reverse-oblique; NM = Normal; NMO = Normal-oblique.

Table 3.2. Summary of data sets used in models for magnitude scaling.

Model	Style of Faulting[1]	N Events	Event **M** Range	Data Set[2]
MEA22	RV/RVO	42	4.7 – 8.02	MEA22 MD
KEA22	SS	34	5.2 – 7.9	FDHI
	RV/RVO	25	4.9 – 8.02	
	NM/NMO	14	6.2 – 7.76	
CEA22	SS	29	6.0 – 7.9	FDHI
LA22	SS	34	5.0 – 7.9	FDHI
	RV/RVO	25	4.9 – 8.02	
	NM/NMO	15	6.2 – 7.76	
YEA03	NM/NMO	56	5.6 – 8.1	Wells and Coppersmith (1994), AD for all styles
PEA11	SS	21	6.3 – 7.9	Wesnousky (2008) subset, plus 9 PEA11 events
MR11	RV/RVO	25	5.4 – 7.9	MR11 MD

[1] SS = Strike-slip; RV = Reverse; RVO = Reverse-oblique; NM = Normal; NMO = Normal-oblique.
[2] MD = maximum displacement; AD = average displacement.

3.2 MODEL APPLICABILITY

The applicability conditions for each model, as specified by the model developers, are listed in Table 3.3. The recommendations are generally based on the empirical data used to develop the model and the modeler's confidence in extrapolating beyond the data or limiting applicability where data are sparse. For example, the LA22 model developers note that their FDM can be used for up to **M** 8.5 earthquakes because the underlying model is based on wavenumber spectrum analysis that provides a physical basis for magnitude scaling and enables extrapolation to larger magnitudes (Lavrentiadis and Abrahamson, 2019, 2022). The CEA22 model developers compared the magnitude scaling used in their model to average displacement data sets compiled by others and found the scaling was consistent for up to **M** 8.3 strike-slip earthquakes. The magnitude range for the PEA11 model is based on personal communication with the model developers, whereas the recommended magnitude ranges for all other models are reported in the respective reference. All FDMs except KEA22 use a folded profile functional form, requiring the normalized position to be ≤ 0.5.

Table 3.3. Recommended model applicability.

Model	Style of Faulting[(1)]	Magnitude	Normalized Position
MEA22	RV/RVO	4.7 – 8.0	$[0, 0.5]$
KEA22	SS	6.0 – 8.0	$[0, 1]$[(2)]
	RV/RVO	5.0 – 8.0	
	NM/NMO	6.0 – 8.0	
CEA22	SS	6.0 – 8.3	$[0, 0.5]$[(3)]
LA22	All	5.0 – 8.5	$[0, 0.5]$
YEA03	NM/NMO	5.6 – 8.1[(4)]	$[0, 0.5]$
PEA11	SS	6.0 – 8.0	$[0, 0.5]$
MR11	RV/RVO	5.5 – 8.0	$[0, 0.5]$

(1) SS = Strike-slip; RV = Reverse; RVO = Reverse-oblique; NM = Normal; NMO = Normal-oblique.
(2) Calculation for complimentary position $(1 - x/L)$ should be equally-weighted in most cases because profile asymmetry is not known a priori.
(3) An alternative unfolded $[0,1]$ formulation is also provided for the $nEMG$ distribution.
(4) Based on Wells and Coppersmith (1994) displacement – magnitude regression.

4 Median Value Comparisons

This chapter presents comparisons of median displacement predictions. The comparisons are shown for scaling with moment magnitude (**M**) and normalized rupture position (x/L). All FDMs use moment magnitude and normalized position along rupture as predictor variables (Table 2.2). The LA22 model also uses surface rupture length (SRL). To obtain the surface rupture length, we use the median prediction from the new model by Lavrentiadis et al. (2022b), which is based on moment magnitude and seismogenic width. A width of 15 km is used in the calculations.

The normalized models (MEA22, YEA03, and MR11) allow for any appropriate displacement – moment magnitude relation. The following empirical relations are used in this report, which are also listed in Table 3.2:

- MEA22: Moss et al. (2022) $log(MD) - \boldsymbol{M}$, complete only
- YEA03: Wells and Coppersmith (1994) $log(AD) - \boldsymbol{M}$, all styles of faulting
- MR11: Moss and Ross (2011), $log(MD) - \boldsymbol{M}$

For models that have alternative formulations, the calculations were performed for the formulation and displacement metrics listed in Table 2.3. The preferred (Model 4) $nEMG$ parameters were used for the CEA22 model. For the KEA22 model, the calculations were performed using the mean coefficients and the results reflect the folded profile implementation (i.e., equal weighting with the complimentary position $1 - x/L$).

4.1 LOCATION SCALING

The shape of the displacement profile is defined by the location scaling component of each model. The shape or functional form of the displacement profile used in each model is a modeling decision. In the LA22 model, the shape of the displacement profile is determined from simulations in the wavenumber domain; however, a space domain functional form with consistent taper scaling is provided for convenience. For all other models, an along-strike functional form is prescribed by the model developer for the full rupture. Qualitative summaries of the displacement profile shapes (i.e., functional forms) used in each model are listed in Table 4.1. The shape descriptions are in semi-log space (i.e., linear normalized position and log of displacement).

Table 4.1. Summary of model scaling components.

Model	Location Scaling		Magnitude Scaling	
	Prescribed Profile Shape[1]	Symmetrical About Rupture Midpoint	Formulation	Relationship[1]
MEA22	Approximately Linear	✓	$MD(\boldsymbol{M})$	Linear
KEA22	Beta Distribution PDF	–	$f(\boldsymbol{M})$	Bi-linear
CEA22	Elliptical	✓	$f(\boldsymbol{M})$	Bi-linear
LA22	Approx. Quadratic[2]	✓	$f(\boldsymbol{M}, SRL)$	Tri-linear
YEA03	Approximately Linear	✓	$AD(\boldsymbol{M})$	Linear
PEA11	Elliptical	✓	$f(\boldsymbol{M})$	Linear
MR11	Approximately Linear	✓	$MD(\boldsymbol{M})$	Linear

[1] In semi-log space.
[2] Profile shape is determined in wavenumber domain.

Location scaling is parameterized only using the normalized position along the rupture length in most models (Table 2.2). As a result, the profile shape is independent of earthquake size and is only based on the style of faulting in most models. An exception is the LA22 model, which also uses surface rupture length as a parameter in the location scaling and therefore considers earthquake size in the profile shape.

The median profile shapes are compared on Figure 4.1 for each style of faulting. The profiles are normalized by the area under the curve. Area-normalized profiles are used to remove the effects of magnitude scaling and thereby provide a direct visual comparison between profile shapes and end-of-rupture tapering effects. The area-normalized profiles $g(\tilde{x})$ are computed using the following equation:

$$g(\tilde{x}) = \frac{f(\tilde{x})}{\int_0^1 f(\tilde{x})d\tilde{x}} \tag{4.1}$$

Where $f(\tilde{x})$ is the median profile for a given model and $\tilde{x} = \frac{x}{L}$. The integral was approximated using numerical integration with the trapezoidal rule and a step size of 0.01 units on Figure 4.1.

Two profiles are shown for the LA22 model to capture the effect of earthquake size. It should be noted that the plots on Figure 4.1 should not be interpreted as normalized average displacement plots for the LA22 model because of the magnitude dependence (via the surface rupture length parameter). In other words, the area under the LA22 **M** 5.0 and **M** 8.0 profiles are both equal to unity. However, these plots effectively serve as normalized average displacement profiles for the other models because their location scaling components are independent of earthquake size.

Overall, the median location scaling between all models is similar along most of the rupture for each style of faulting. The strike-slip profiles are generally more elliptical, and the dip-slip

style profiles are generally flatter. The LA22 model shows a strong magnitude dependence on tapering at the rupture ends for all styles of faulting, but the tapering is strongest for small magnitude strike-slip events (Figure 4.1a). The LA22 model also produces flatter profiles for larger magnitudes in the normalizing space, implying a non-self-similar scaling (i.e., the tapering length scales slower than the rupture length). In all cases, the differences between models are most significant within ±15% of the rupture endpoints.

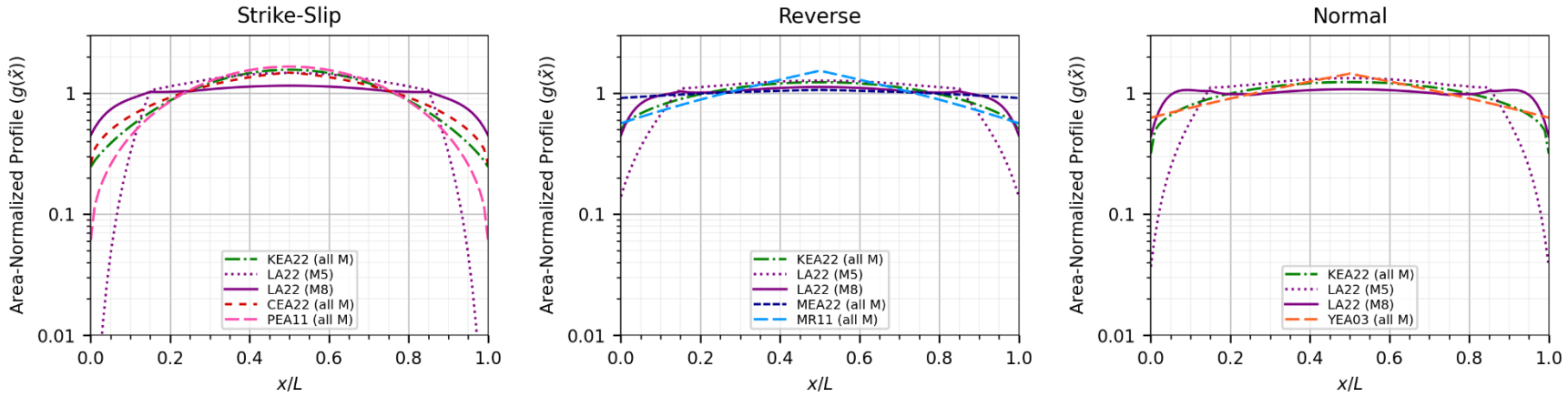

(a) Strike-slip events. **(b)** Reverse events. **(c)** Normal events.

Figure 4.1. Comparison of location scaling using equal-area median profiles.

4.2 MAGNITUDE SCALING

The amplitude of the median profile is scaled based on earthquake size in all models. The LA22 model uses both moment magnitude and surface rupture length to capture earthquake size, whereas the other models only use moment magnitude. The magnitude scaling approach in each model is summarized in Table 4.1. The existing models all use a log-linear magnitude scaling relation based on style of faulting. The new CEA22 and KEA22 models both use bi-linear magnitude scaling with magnitude breakpoints at **M** 7.1 and 7.0, respectively, to produce steeper scaling for smaller magnitudes. The LA22 model uses tri-linear scaling with breakpoints at **M** 6.0 and 6.7 and linear scaling with $ln(SRL)$. We present magnitude scaling as a function of average and maximum displacements below.

4.2.1 Average Displacement

Several methods exist for calculating average displacement based on empirical observations. A common approach is to compute the arithmetic mean of all measurements or a subset of higher quality measurements; however, the mean may not be representative of the average displacement across the entire rupture if the number of measurements is insufficient or the measurements are not spatially distributed along the rupture length (Wells and Coppersmith, 1994). Instead, displacement profiles are often constructed by linearly interpolating between measurement sites (or along a prescribed profile shape), and the average displacement is computed as the area under the profile (e.g., Litchfield et al., 2013). The integration approach generally provides a more accurate estimate of the true average displacement because it evenly samples measurements along the rupture length and better captures displacement tapering at rupture end-points (which is commonly under-sampled in empirical data sets). Displacement profiles are provided by all models, so we use the integration method in most cases to compare the predicted average displacement between the models.

Figure 4.2 shows how the median average displacement scales with magnitude for each model. The YEA03 FDM uses average displacement as the normalization variable, which is computed as a function of magnitude using the Wells and Coppersmith (1994) $log(AD) - \boldsymbol{M}$ relation for all styles of faulting. The average displacement AD for all other models is computed using the following equation, where f(x̃) is the median profile for a given earthquake magnitude and model and $\tilde{x} = \frac{x}{L}$:

$$\mathrm{AD} = \int_0^1 \mathrm{f}(\tilde{\mathrm{x}})\mathrm{d}\tilde{\mathrm{x}} \tag{4.2}$$

The integral was approximated using numerical integration with the trapezoidal rule and a step size of 0.01 units on Figure 4.2. We note the D/MD formulations are used herein for the MR11 and MEA22 models, and the average displacement implied by integration is different than

the average displacement computed using their respective $log(AD) - \boldsymbol{M}$ relations. The discrepancy is due to differences in the magnitude scaling (i.e., steeper or flatter slopes). The magnitude scaling differences arise because the relationship between MD and AD is not constant for all magnitudes, which is at least partly due to different methods used to determine AD (cf. Chapter 4.2.1).

The following observations summarize the comparisons of the average displacements on Figure 4.2 between the new models:

- Displacements are within a factor of about 2.5 at **M** 6.0 and within a factor of 1.5 for **M** ≥ 6.8 for strike-slip faulting. The predictions are most similar at **M** 6.9 - 7.9 (within a factor of 1.2).
- Displacements are within a factor of 1.2 at **M** 5.0 and increase to a factor of 1.8 at **M** 8.0 for reverse faulting.
- Displacements are within a factor of 2.5 for **M** ≥ 6.3 and are most similar at **M** 7.1 (within a factor of 1.2) for normal faulting.
- For strike-slip faulting, the new models generally produce higher average displacements for roughly **M** 6.7 to 7.8 than the existing PEA11 model due to the piecewise (bi-linear or tri-linear) magnitude scaling in the new models. For example, at **M** 7.0, average displacements in the new models are about 70% higher than in PEA11.
- The MR11 scaling is similar to the new reverse models for all magnitudes.
- For normal faulting, the scaling in the LA22 model is similar to the existing YEA03 model for **M** ≤ 7.5 and flatter at larger magnitudes. The bi-linear scaling in the KEA22 model produces average displacements that are similar to YEA03 and LA22 at **M** 7.0, but the differences at other magnitudes can be significant. For example, the KEA22 average displacements at **M** 6.0 and 8.0 are, respectively, four and 2.5 times lower than the YEA03 values.

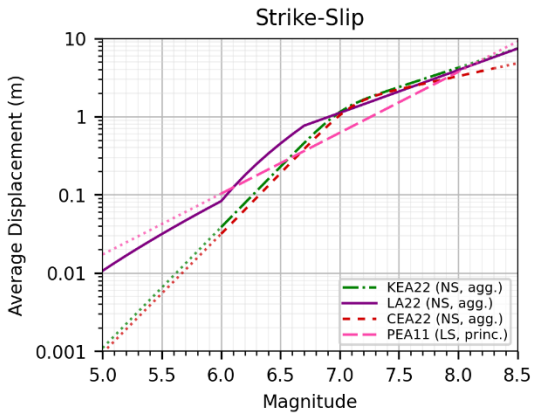

(a) Strike-slip events.

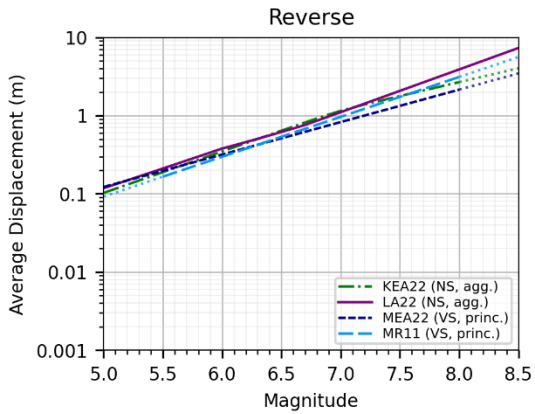

(b) Reverse events.

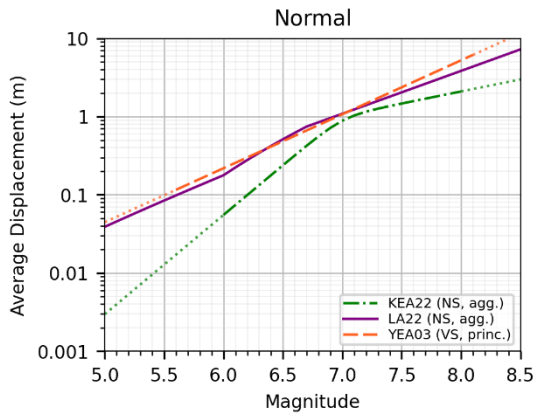

(c) Normal events.

Figure 4.2. Comparison of magnitude scaling for median average displacement. Dotted lines at low and high magnitudes indicate extrapolation beyond recommend magnitude applicability range for the model (Table 3.3). NS = net slip component; LS = lateral slip component; VS = vertical slip component (see Chapter 2.1.1 for slip component discussion).

4.2.2 Maximum Displacement

Four models (MEA22, CEA22, LA22, and MR11) provide predictions for maximum displacement. While average displacement can be determined from displacement profiles, maximum displacement must be directly modeled. Maximum displacement is typically modeled using linear regression with moment magnitude as the predictor variable. However, it can also be modeled using numerical simulation.

Three models (MEA22, CEA22, and MR11) use linear regression to model maximum displacement. The MEA22 and MR11 models use ordinary least squares regression based on data sets of moment magnitude **M** and maximum displacement MD from reverse and reverse-oblique earthquakes (Table 3.2) to produce linear $log(MD) - \boldsymbol{M}$ scaling relations. The CEA22 model uses linear regression with maximum likelihood estimation on maximum displacement data from strike-slip events in the FDHI Database against a backbone bilinear magnitude scaling formulation to produce a bilinear $ln(MD) - \boldsymbol{M}$ scaling relation. The MR11 and MEA22 FDMs predict normalized displacements (i.e., D/MD); therefore, the maximum displacement regressions are consistent with their FDMs. However, the CEA22 maximum displacement regression was developed separately from the $nEMG$ distribution, and the predicted maximum displacements generally correspond with the 90th percentile of the $nEMG$ distribution. Because there is a 10% probability that the predicted maximum displacements will be exceeded, the authors generally advise against using the maximum displacement regression to predict maximum displacement (Chiou et al., 2022).

The LA22 model uses numerical simulation to predict a maximum-to-average displacement log ratio $ln(MD/AD)$ consistent with the statistical distribution used in their FDM. Specifically, they use a magnitude-dependent correlation length model and calculate spatially-correlated residuals for a fixed number of equally-spaced locations along the rupture length. The residuals are paired with the median prediction at the location to determine the maximum displacement. The correlation length model has a first-order impact on the predicted maximum displacement because it governs the number of uncorrelated (independent) samples in a fixed sample size, and the probability of sampling a higher percentile increases with the number of independent draws. Although the correlation length increases with magnitude, the correlation lengths are still short (ranging from 1.5 to 3.5 km for **M** 6.0 to 8.0, respectively). As a result, the corresponding percentile for maximum displacement increases with magnitude because larger magnitudes have fewer correlated samples.

We use results from the LA22 model to estimate the median maximum displacement implied by the statistical distributions for the models that do not provide maximum displacement predictions (i.e., KEA22, YEA03, and PEA11), as well as the CEA22 model based on recommendations from the model developers (Chiou, B., pers. comm.). Specifically, implied maximum displacements in these FDMs are calculated based on the mean epsilon values of the

maximum displacements produced in the LA22 model. The epsilon values and the associated percentiles are computed as a function of magnitude and style of faulting using the LA22 model (Figure 4.3), and the displacement at that percentile is calculated from the cumulative probability distribution in other models. The probability distributions are calculated using within-event aleatory variability only because within-event variability controls the median maximum displacement (whereas between-event variability defines the aleatory variability on the maximum displacement prediction). An exception is the PEA11 model, for which the reported variance represents total aleatory variability because the error term was not partitioned into between-event and within-event components; for this case, the LA22 epsilon values are based on the total aleatory variability (Figure 4.3b). The displacement probability distributions are based on a normalized rupture position of $x/L = 0.25$, which is recommended by LA22 as a proxy for the average displacement. This approach assumes that the correlation lengths in other models are similar to the LA22 model correlation, which is a valid assumption for the purpose of comparing implied maximum displacement values.

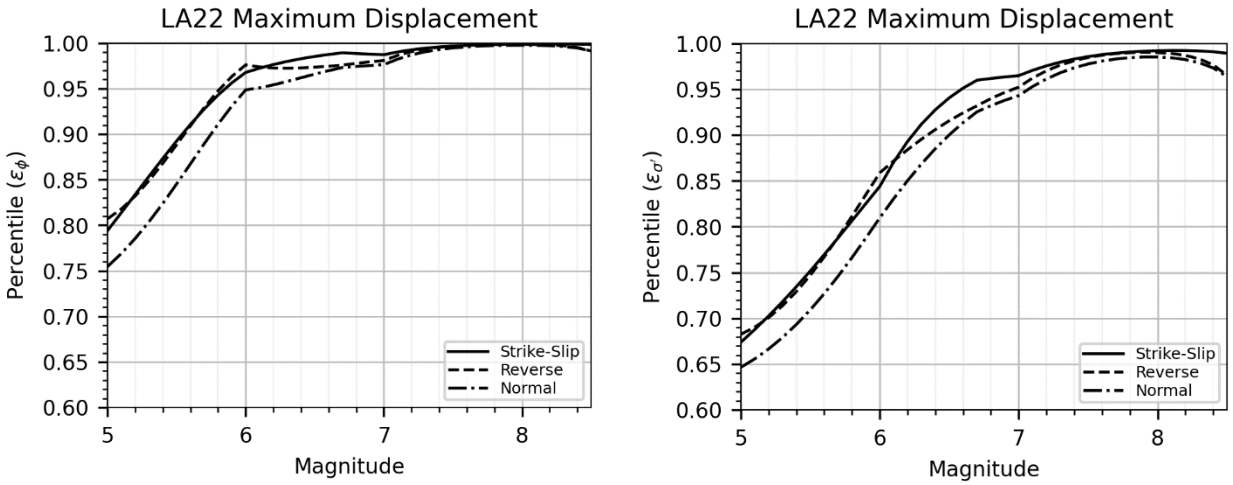

(a) Based on within-event standard deviation.

(b) Based on total standard deviation.

Figure 4.3. Mean epsilon values for predicted maximum displacement as a function of magnitude from LA22 model.

Figure 4.4 shows how the median maximum displacement scales with magnitude for each model. The results for the MEA22, LA22, and MR11 models are based on the maximum displacement formulations provided by the model developers. The results for the other models (KEA22, CEA22, YEA03, and PEA11) are implied values based on the percentiles associated with the mean epsilon values of the maximum displacements in the LA22 model. Maximum

displacements from events in the FDHI Database are plotted for reference and reported maximum displacements from the **M** 7.92 1931 Kehetuohai, China and **M** 8.2 1855 Wairarapa, New Zealand strike-slip earthquakes are also shown (Wells and Coppersmith, 1994; Manighetti et al., 2020). The maximum displacement scaling in the new models is in reasonable agreement with the empirical data. Compared to existing models, the scaling in the new models is in better agreement with the data for large magnitude strike-slip (**M** ≥ 7.0) and normal (**M** ≥ 7.5) events. For reverse events, the scaling in the new models is in good agreement with the data and similar to the scaling in MR11.

The following observations summarize the comparisons of the maximum displacements on Figure 4.4 between the new models:

- Displacements are within a factor of three for **M** ≥ 6.0 and are most similar at **M** 7.1 (within a factor of 1.5) for strike-slip faulting.
- Displacements are within a factor of about two for **M** ≤ 7.1 and within a factor of three for larger magnitudes for reverse faulting.
- Displacements are within a factor of 1.5 for **M** ≥ 6.0 for normal faulting.
- For a strike-slip **M** 8.0 event, the new models predict maximum displacements that are less than half of the value implied by the statistical distribution used in the PEA11 model. The PEA11 model scaling is similar to the LA22 model for **M** ≤ 7.0.
- The MR11 scaling is similar to the new reverse models for all magnitudes.
- For a normal **M** 8.0 event, the new models predict maximum displacements that are at least 20% less than the value implied by the statistical distribution used in the YEA03 model. However, the YEA03 model scaling is similar to the LA22 model for **M** ≤ 8.0.

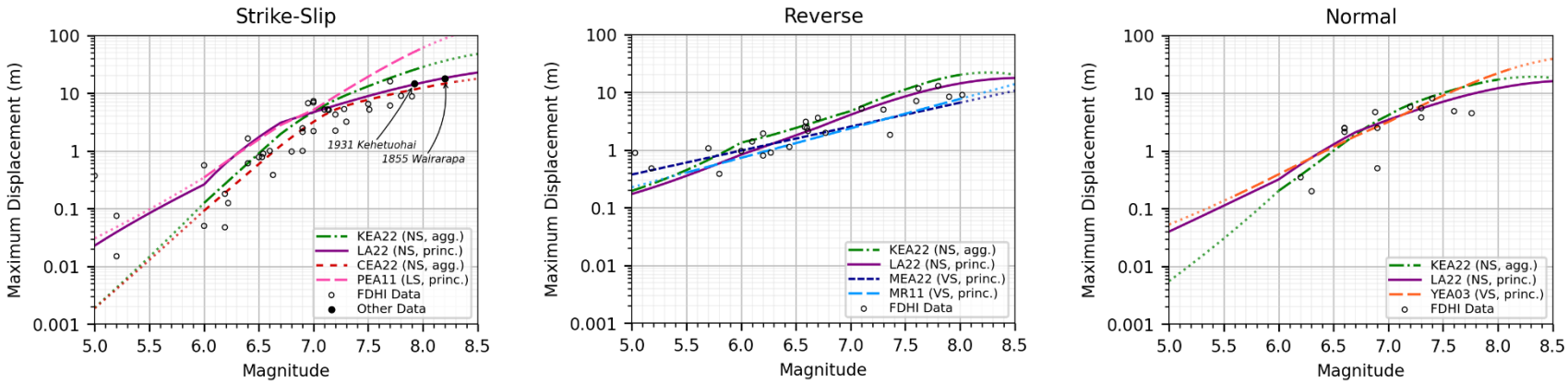

(a) Strike-slip events. **(b)** Reverse events. **(c)** Normal events.

Figure 4.4. Comparison of magnitude scaling for median maximum displacement against empirical data (i.e., maximum principal displacement). Results for MEA22, LA22, and MR11 based on formulations provided by model developers. See text for discussion on the basis for KEA22, CEA22, YEA03, and PEA11 results. Dotted lines at low and high magnitudes indicate extrapolation beyond recommend magnitude applicability range for the model (Table 3.3). NS = net slip component; LS = lateral slip component; VS = vertical slip component (see Chapter 2.1.1 for slip component discussion).

5 Aleatory Variability Comparisons

This chapter summarizes the aleatory variability in each model and makes comparisons between the models. Table 5.1 lists the probability distributions used in each model as the aleatory variability model components. Most of the new models use magnitude- and location-dependent scale parameters in the statistical distributions. While between-event variability in magnitude scaling is common, we note that the KEA22 model also considers between-event variability in location scaling for dip-slip events. The KEA22 model developers observed significant differences in profile shapes (i.e., flat vs. elliptical) for reverse and normal earthquakes (but not strike-slip earthquakes) and included event-specific terms for location scaling to capture this variability. The event-specific terms were modeled as random effects.

The LA22 model is different from other FDMs in two key ways that are important to the model implementation. First, their model was developed using data from individual rupture segments. As a result, an additional component of aleatory variability (σ_{add}) is required to capture the effect of segmentation (Table 5.1), and the conditional probability that a site location is within a gap between segments, $P(D_{agg} = 0)$, must be included in hazard calculations for aggregated displacement. Second, the LA22 developers explicitly modeled the conditional probability of zero principal displacement, $P(D_{princ} = 0)$, which must be included in hazard calculations for principal displacement. Excluding the conditional probability terms will result in overestimating hazard because these terms scale down the probability of exceedance, rather than affecting the displacement amplitude probability distributions (which are based on non-zero displacements).

In ground motion modeling, comparisons of aleatory variability are usually presented by showing model standard deviations. This is possible because ground motions are mostly modeled using lognormal distributions, and the aleatory variability of a model can be fully described with the standard deviation. Unlike ground motion models, several different probability distributions are used in the FDMs (Table 5.1), and direct comparisons of scale parameters between different statistical distributions are challenging.

Aleatory variability comparisons are presented in this chapter in two ways. First, cumulative displacement distribution curves are shown for a range of scenarios (i.e., magnitude and normalized rupture position) and are paired with fractile plots for convenience. Second, probability of exceedance hazard curves are presented. Additional comparisons in Appendix B

provide plots of the logarithmic ratios of 84th-to-median and median-to-16th percentiles. While the ratio plots in Appendix B and the model component summary in Table 5.1 provide insight into how each model developer handled aleatory variability and how the approaches compare between models, the most direct way to compare the aleatory variability between different models is to evaluate probability densities or cumulative distributions for specific scenarios, as in Chapter 5.1. The hazard curves in Chapter 5.2 provide an idea of how the models will compare in a probabilistic analysis.

The calculations in this chapter are performed as described at the beginning of Chapter 4. All aleatory model components listed in Table 5.1 are also included in the calculations in this chapter. Additionally, aleatory variability on the maximum or average displacement was also included for the normalized displacement models (MEA22, YEA03, and MR11; Table 5.1) to make the comparisons to other models more consistent. Specifically, the MD or AD values were sampled from ±6 standard deviations in 0.2-increments. The same MD and AD models described in Chapter 4 and in Table 3.2 were used here. The probability of exceedance plots in Chapter 5.2 include the gap probability $P(D_{agg} = 0)$ for the LA22 model; however, the cumulative distributions in Chapter 5.1 are provided without gap probabilities to directly compare the distributions for non-zero displacements.

Table 5.1. Summary of aleatory variability model components.

Model	Statistical Distribution	Between-Event	Within-Event	Other
MEA22	$D/MD \sim Gamma$	*	Location-dependent	–
KEA22	$lnD \sim Normal$	Magnitude-dependent[(1)] and location-dependent[(2)]	Location-dependent	–
CEA22	$lnD \sim nEMG$	Magnitude-dependent	Location-dependent	–
LA22	$D^{0.3} \sim Normal$	Magnitude-dependent	Constant	Magnitude-dependent[(4)]
YEA03	$D/AD \sim Gamma$	*	Location-dependent	–
PEA11	$lnD \sim Normal$	Constant[(3)]		–
MR11	$D/MD \sim Beta$	*	Location-dependent	–

* Provided by the maximum displacement (MD) or average displacement (AD) models; typically constant.
(1) Constant for reverse style of faulting.
(2) For reverse and normal styles of faulting.
(3) Error term was not partitioned into between-event and within-event components, so reported variance represents total aleatory variability.
(4) Additional aleatory variability component is used to capture fault segmentation.

5.1 CUMULATIVE DISTRIBUTIONS AND FRACTILES

We provide a series of plots on Figures 5.1 through 5.15 that show cumulative probability curves (top panels) and compare specific percentiles (bottom panels) for a broad range of scenarios for each style of faulting. Specifically, three normalized positions along the folded rupture length are shown (x/L 0, 0.25, and 0.5) for five magnitudes (**M** 6.0, 6.8, 7.2, 7.7, and 8.0). These combinations capture a representative range of scenarios and are within the recommended limits of each model (Table 3.3). Collectively, these plots characterize the aleatory variability in each model. The distribution curves and fractile plots for the LA22 FDM are provided without the gap probability scaling to directly compare the distributions for non-zero displacements. Including the $P(D_{agg} = 0)$ gap probability term would affect the lower tail of the distributions because there is a larger probability of zero displacement; any effect on the median and the upper tails is minimal.

The cumulative probability curves and percentile plots for strike-slip faulting are shown on Figures 5.1 through 5.5 for each of the magnitudes evaluated, respectively. The LA22 FDM has a steep taper at rupture endpoints for small magnitude strike-slip events (Figure 4.1a), which is reflected in the cumulative distribution for **M** 6.0 (Figure 5.1). The median and 95th percentile displacements in the new models are within a factor of three for **M** ≥ 6.0 at all rupture positions and within a factor of ~1.5 for **M** ≥ 6.8 at x/L of 0.25 and 0.5. The 5th percentile displacements in the new models are within a factor of four for **M** ≥ 6.0 at x/L of 0.25 and 0.5 but are larger at the rupture endpoint. The upper tail displacements at the rupture endpoint in the new models are larger than the PEA11 model for all magnitudes; however at larger magnitudes (**M** ≥ 7.2), the upper tail displacements in the new models are significantly lower at x/L of 0.25 and 0.5. For example, the 95th percentile displacements in the new models at the rupture midpoint of a **M** 8.0 strike-slip earthquake range from 12 to 19 meters, whereas the PEA11 prediction is 40 meters.

Similar plots are shown for reverse faulting on Figures 5.6 through 5.10. Overall, the differences between all models are smaller for reverse events than strike-slip or normal for all magnitudes and rupture positions. The median and 95th percentile displacements in the new models are within a factor of two for almost all magnitudes and rupture positions. The 5th percentile displacements in the new models are within a factor of three for **M** ≥ 6.0 at x/L of 0.25 and 0.5 but are larger at the rupture endpoint. The upper tail displacements in the new models are similar to the MR11 results for all magnitudes and rupture positions, but generally are lower at large magnitudes (**M** ≥ 7.2) at x/L of 0.25 and 0.5. For example, the 95th percentile displacements in the new models at the rupture midpoint of a **M** 8.0 reverse earthquake range from 7 to 12 meters, whereas the MR11 prediction is 17 meters.

Finally, Figures 5.11 through 5.15 present similar plots for normal faulting. The LA22 FDM has a steep taper at rupture endpoints for small magnitude normal events (Figure 4.1c), which is reflected in the cumulative distribution for **M** 6.0 (Figure 5.11). The median and 95th percentile displacements in the new models are within a factor of about three for **M** ≥ 6.0 at all rupture positions and within a factor of ~1.5 for **M** ≥ 6.8 at x/L of 0.25 and 0.5. The 5th percentile

displacements in the new models are within a factor of two for **M** ≥ 6.0 at x/L of 0.25 and 0.5 but are larger at the rupture endpoint. In almost all cases, the upper tail displacements in the new models are significantly lower than the YEA03 model. For example, the 95th percentile displacements in the new models at the rupture midpoint of a **M** 8.0 normal earthquake range from 9 to 12 meters, whereas the YEA03 prediction is 38 meters.

In summary, the largest variability across all models occurs at rupture endpoints. This is consistent with the location scaling plots in Figure 4.1 and is due to a combination of limited data at rupture endpoints and the profile shapes used in each model (Table 4.1) (particularly the end-of-rupture tapering). Furthermore, the variability across all models is larger at the lower tails and smaller at the upper tails, because the skewed probability distributions used in Table 5.1 have broader lower tails and narrower upper tails. The following observations summarize the comparisons between the new models:

- 50th percentile displacements at rupture endpoints ($x/L = 0$) are within a factor of about 2.5 for all magnitudes considered.
- 95th percentile displacements at rupture endpoints are lowest for normal events (within a factor of 1.5) and highest for strike-slip (within a factor of 2.5 in most cases).
- 5th percentile displacements at rupture endpoints differ by a factor of ten in the new models for all styles of faulting.
- 50th percentile displacements at the rupture midpoint ($x/L = 0.5$) are within a factor of 1.5 to 2 for most magnitudes and styles.
- 95th percentile displacements at the rupture midpoint are lowest for normal events (within a factor of 1.2) and within a factor of two for strike-slip and reverse faulting.
- 5th percentile displacements at the rupture midpoint are within a factor of four or better for all styles of faulting.
- At the rupture midpoint, the new models produce upper tail displacements smaller than the existing models for large magnitudes (**M** ≥ 7.2) and all styles of faulting.

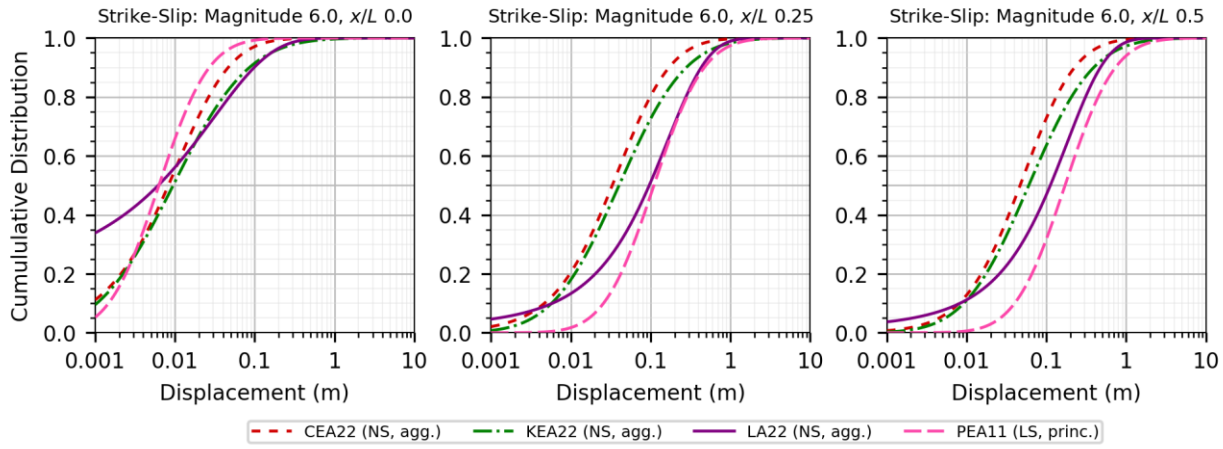

(a) Cumulative displacement probability curves.

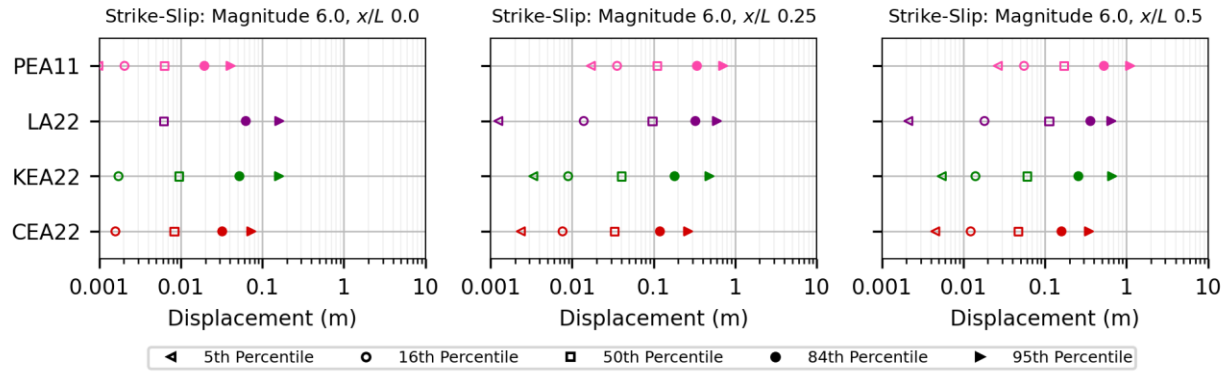

(b) Percentile displacement plots.

Figure 5.1. Comparison of aleatory variability for strike-slip **M** 6.0. NS = net slip component; LS = lateral slip component; VS = vertical slip component (abbreviations apply to all plots; see Chapter 2.1.1 for slip component discussion).

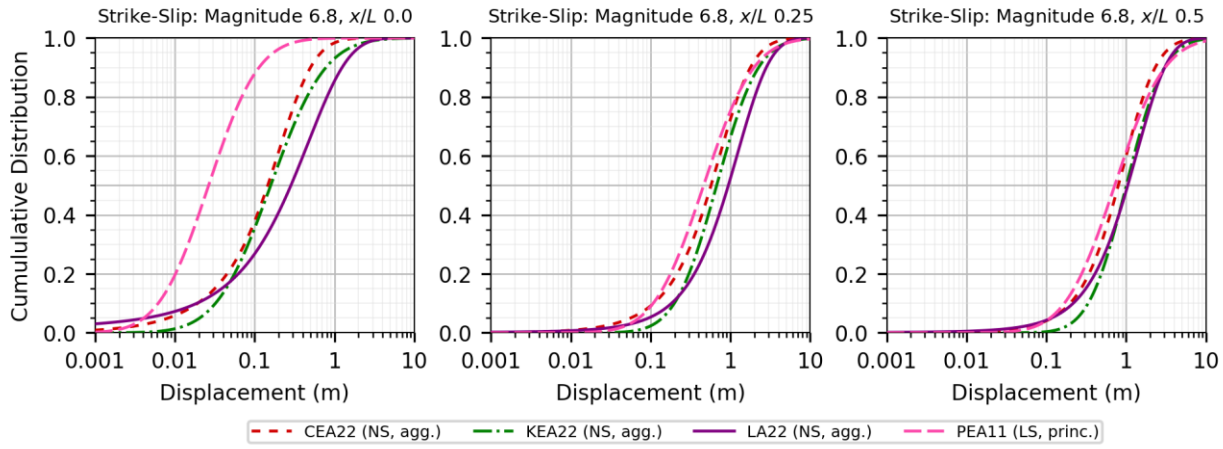

(a) Cumulative displacement probability curves.

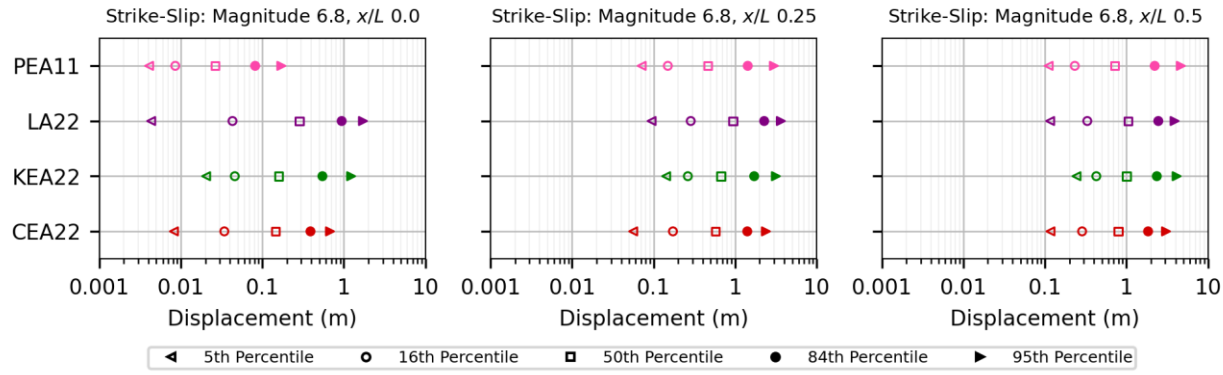

(b) Percentile displacement plots.

Figure 5.2. Comparison of aleatory variability for strike-slip **M** 6.8.

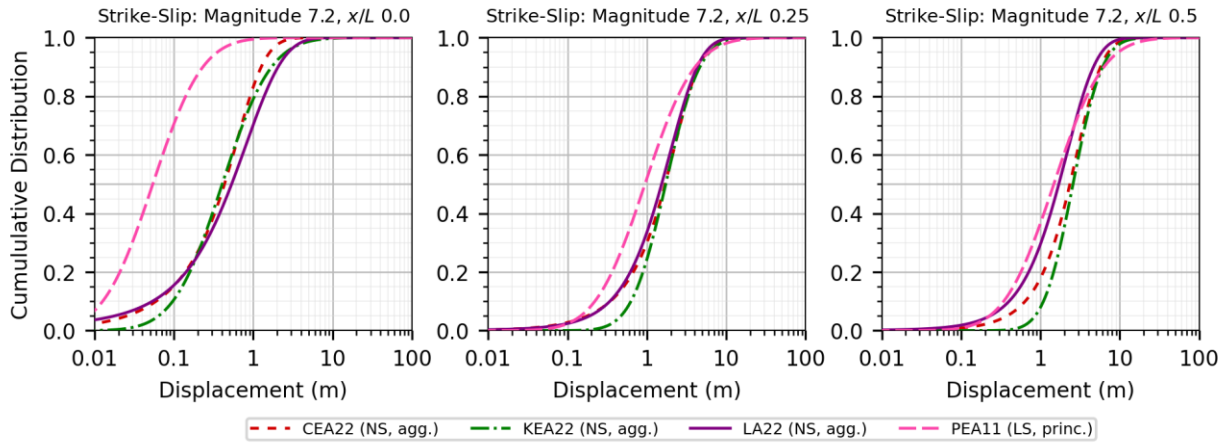

(a) Cumulative displacement probability curves.

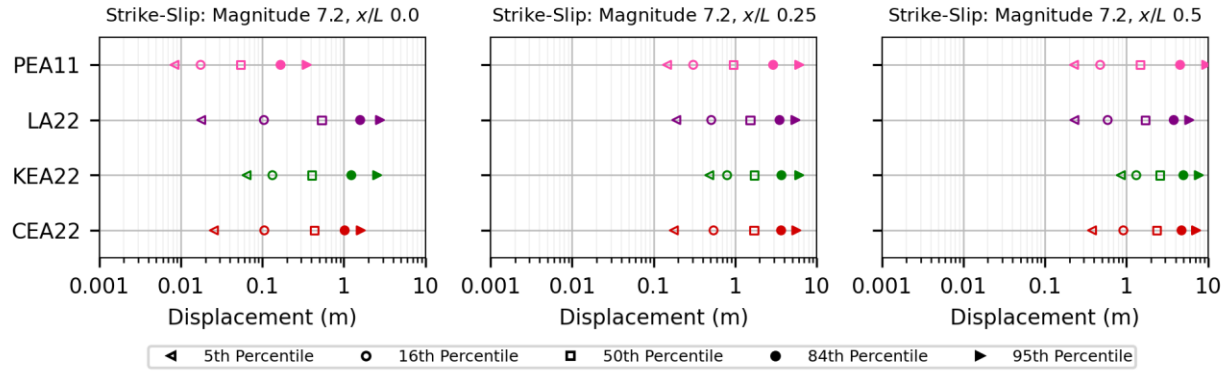

(b) Percentile displacement plots.

Figure 5.3. Comparison of aleatory variability for strike-slip **M** 7.2.

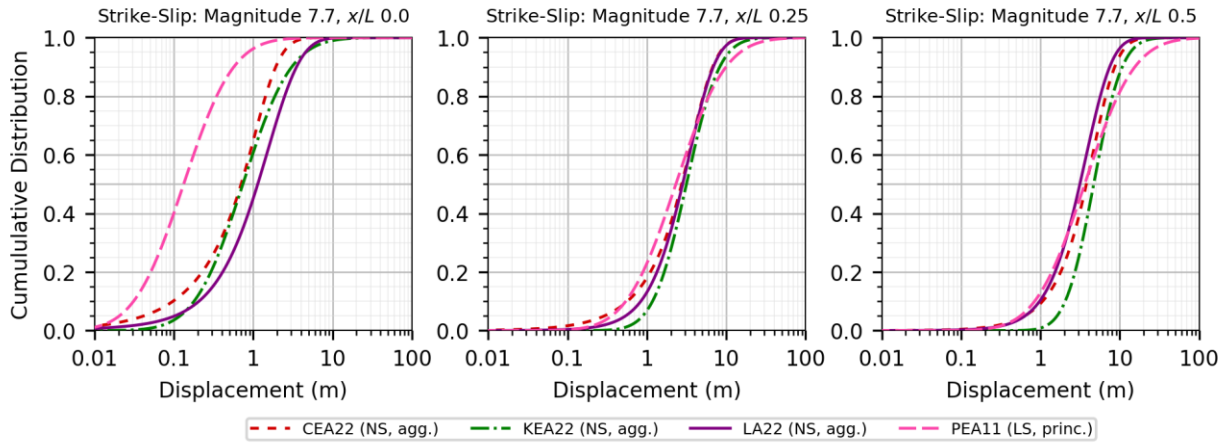

(a) Cumulative displacement probability curves.

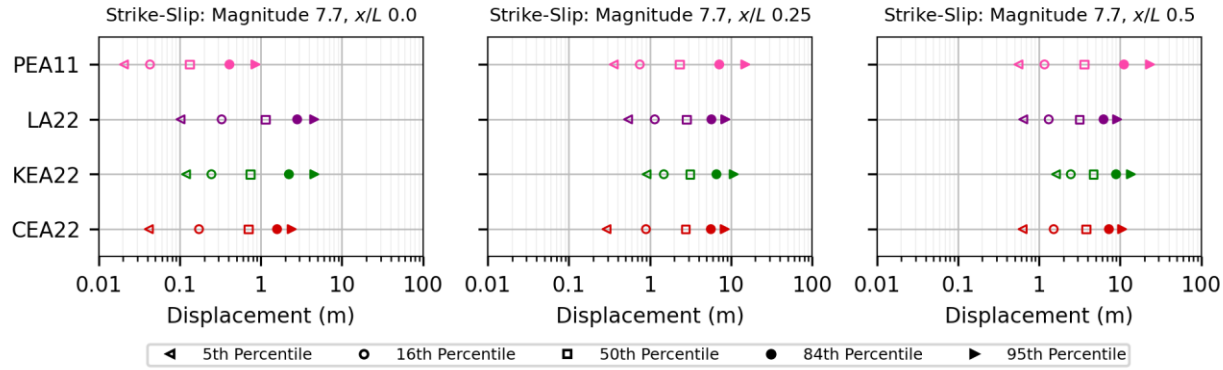

(b) Percentile displacement plots.

Figure 5.4. Comparison of aleatory variability for strike-slip **M** 7.7.

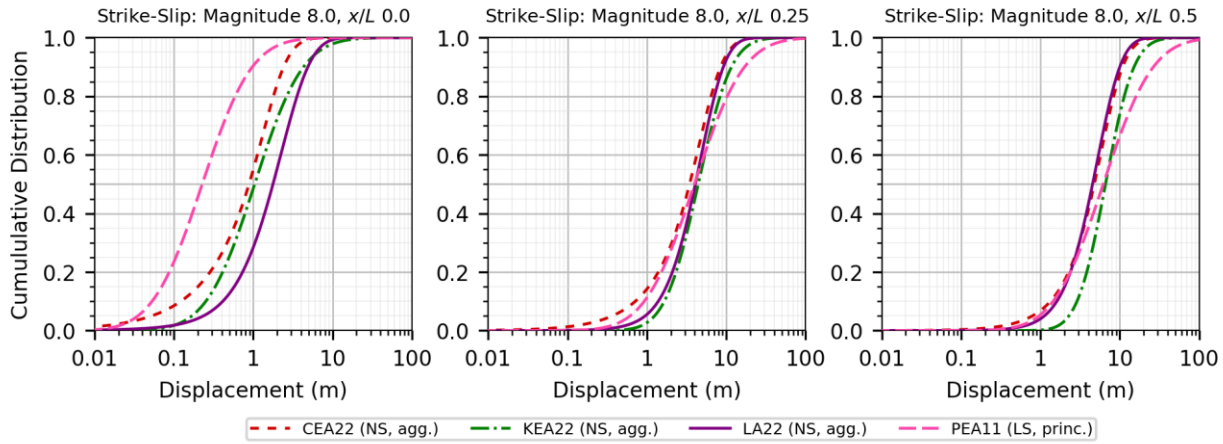

(a) Cumulative displacement probability curves.

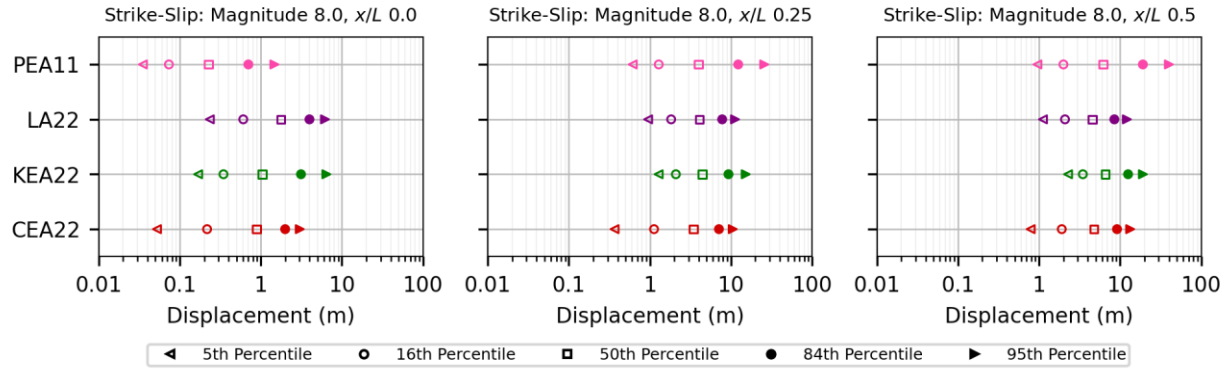

(b) Percentile displacement plots.

Figure 5.5. Comparison of aleatory variability for strike-slip **M** 8.0.

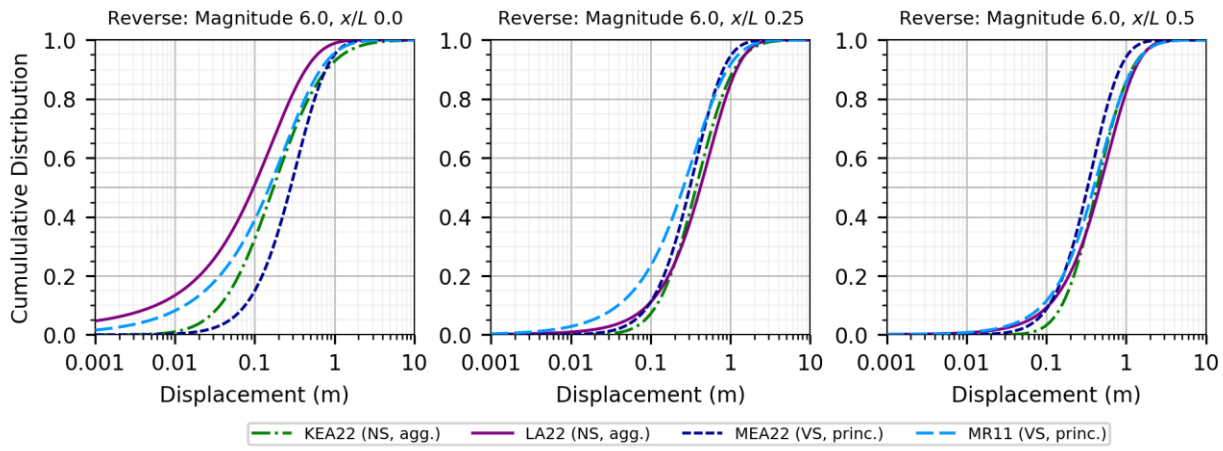

(a) Cumulative displacement probability curves.

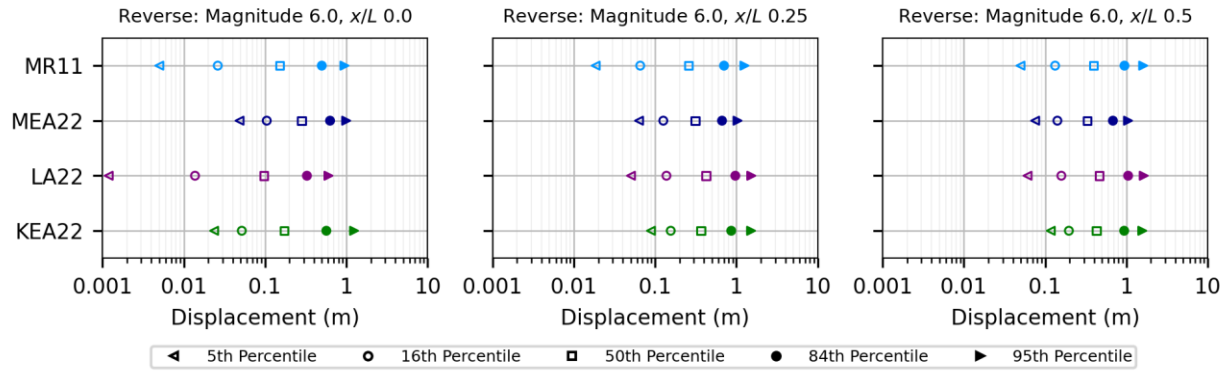

(b) Percentile displacement plots.

Figure 5.6. Comparison of aleatory variability for reverse **M** 6.0.

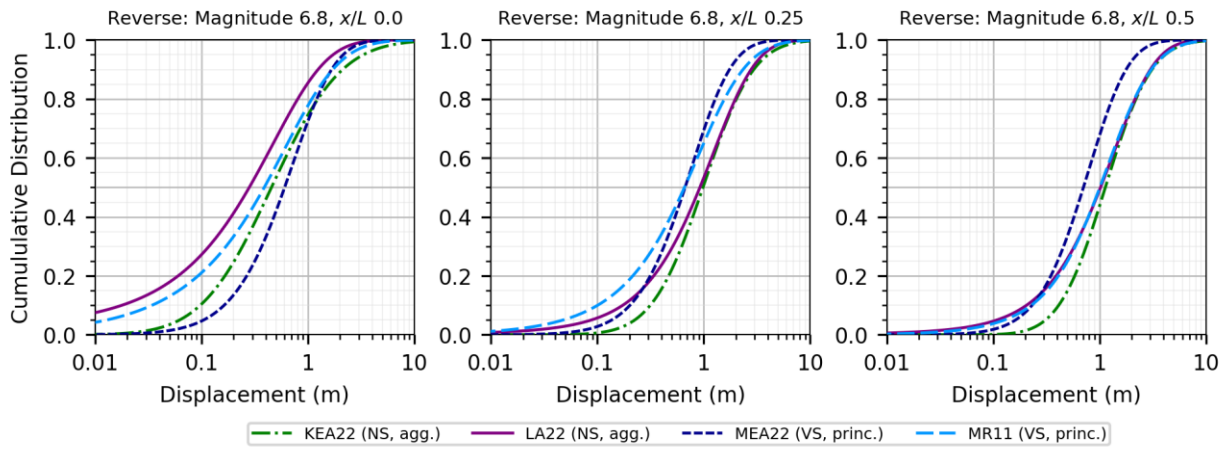

(a) Cumulative displacement probability curves.

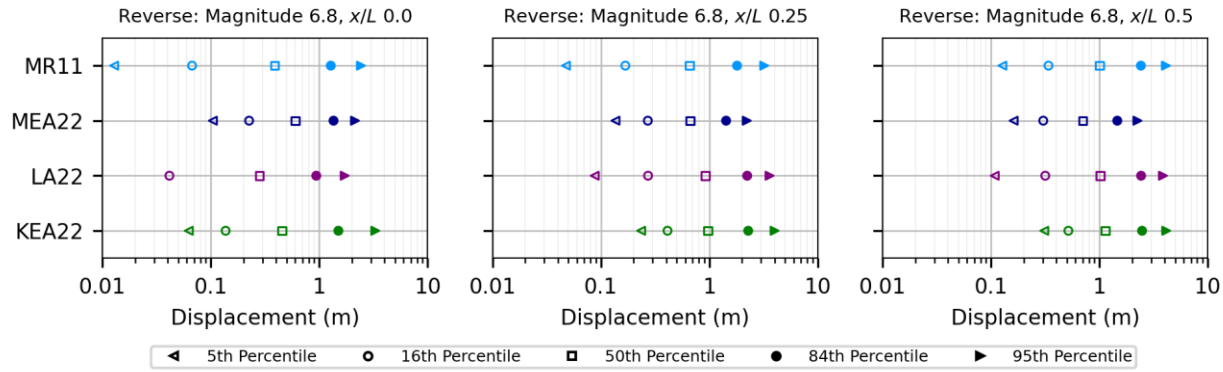

(b) Percentile displacement plots.

Figure 5.7. Comparison of aleatory variability for reverse **M** 6.8.

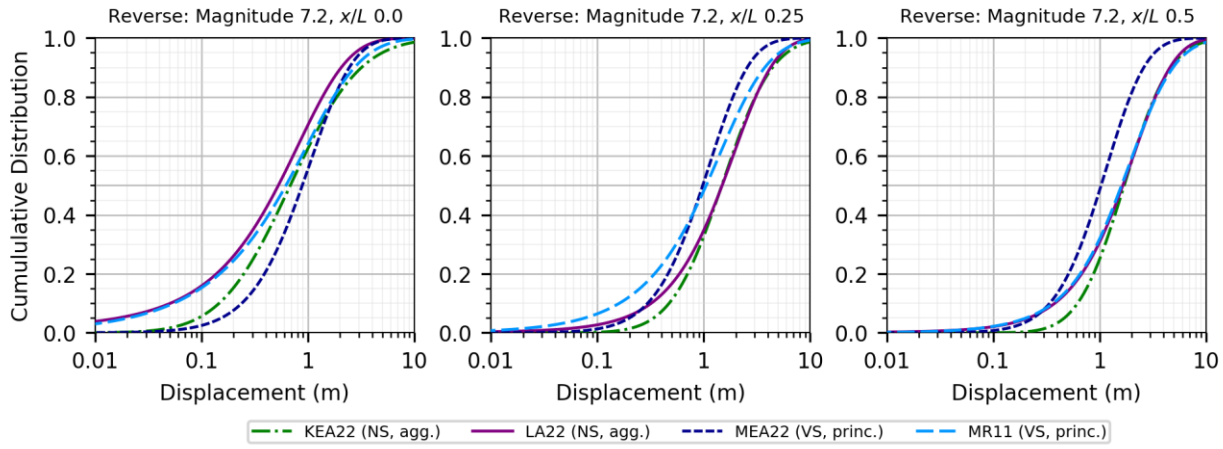

(a) Cumulative displacement probability curves.

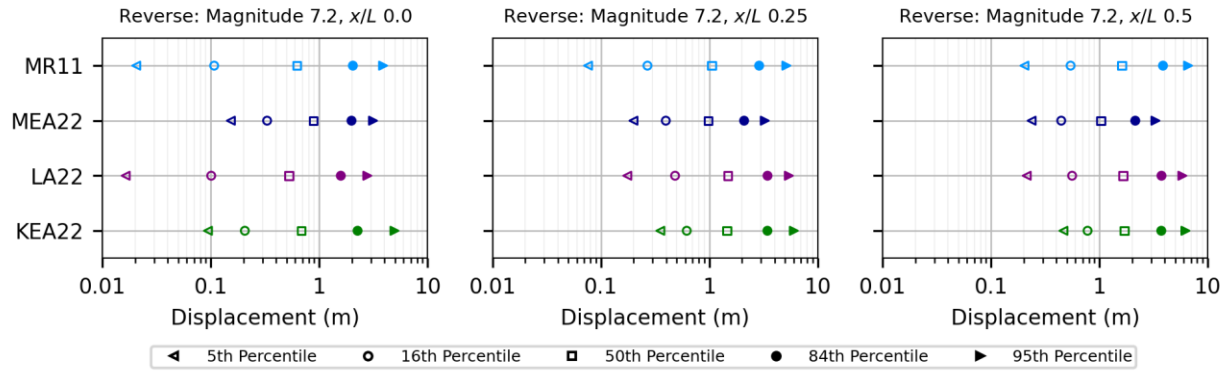

(b) Percentile displacement plots.

Figure 5.8. Comparison of aleatory variability for reverse **M** 7.2.

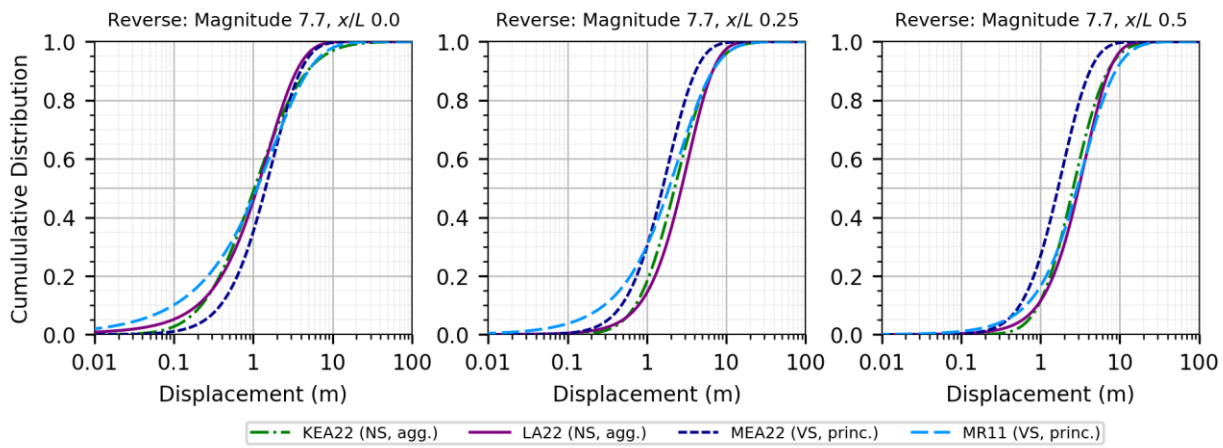

(a) Cumulative displacement probability curves.

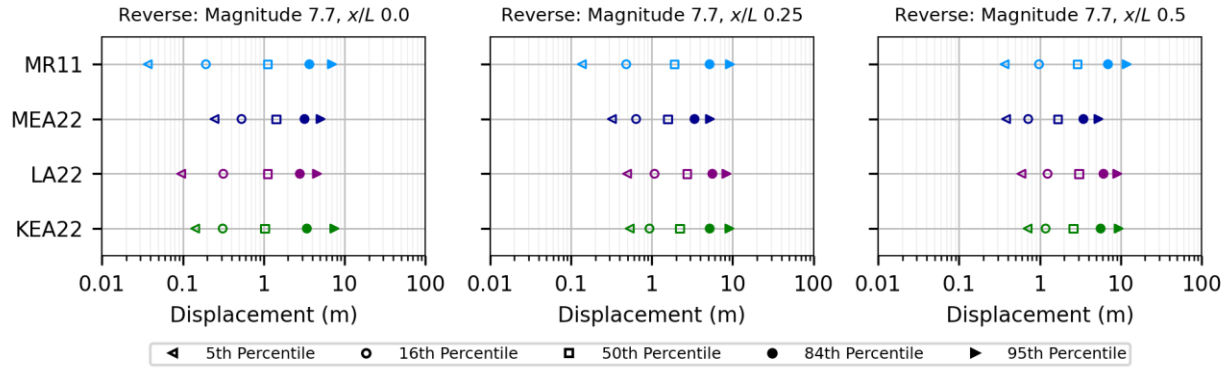

(b) Percentile displacement plots.

Figure 5.9. Comparison of aleatory variability for reverse **M** 7.7.

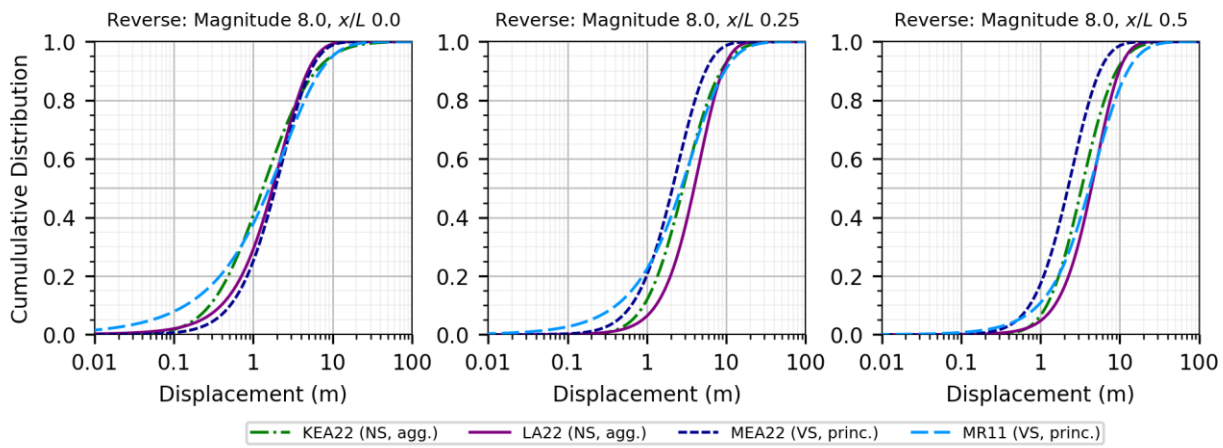

(a) Cumulative displacement probability curves.

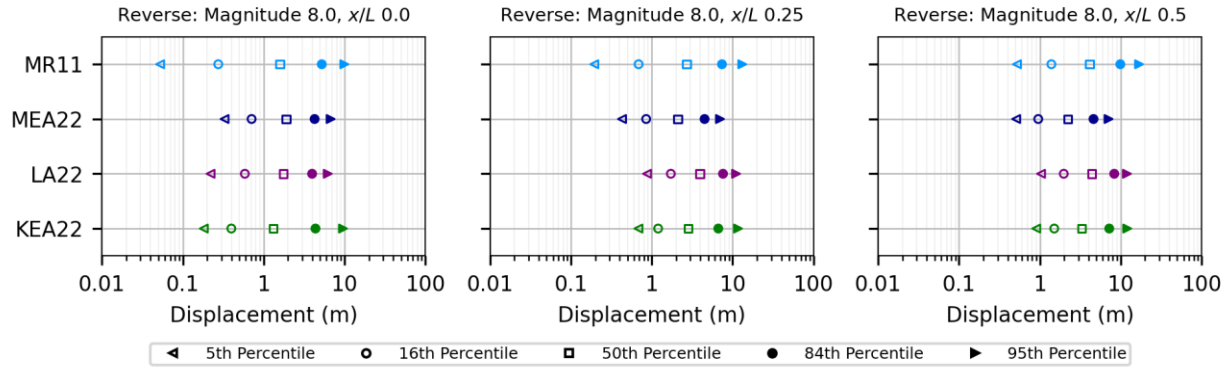

(b) Percentile displacement plots.

Figure 5.10. Comparison of aleatory variability for reverse **M** 8.0.

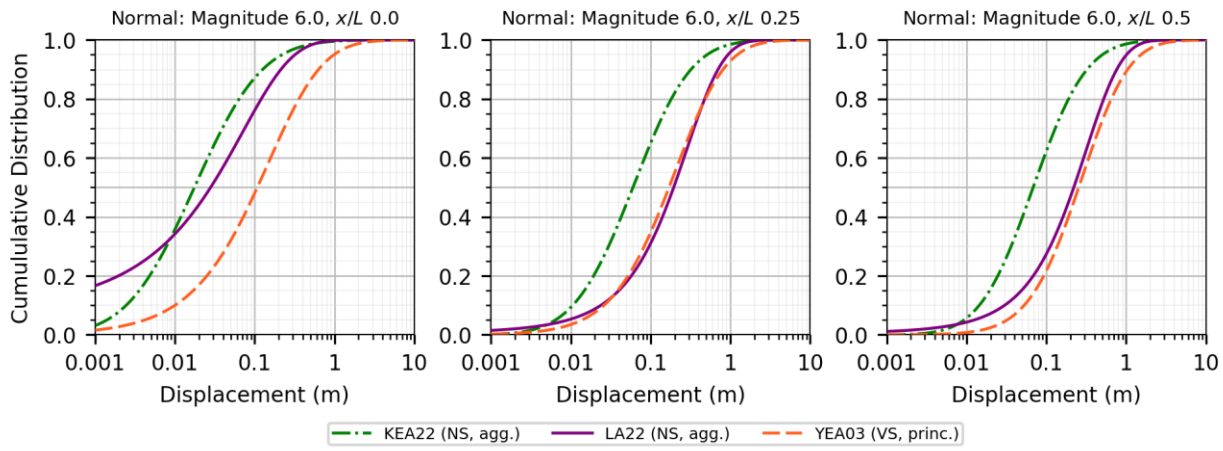

(a) Cumulative displacement probability curves.

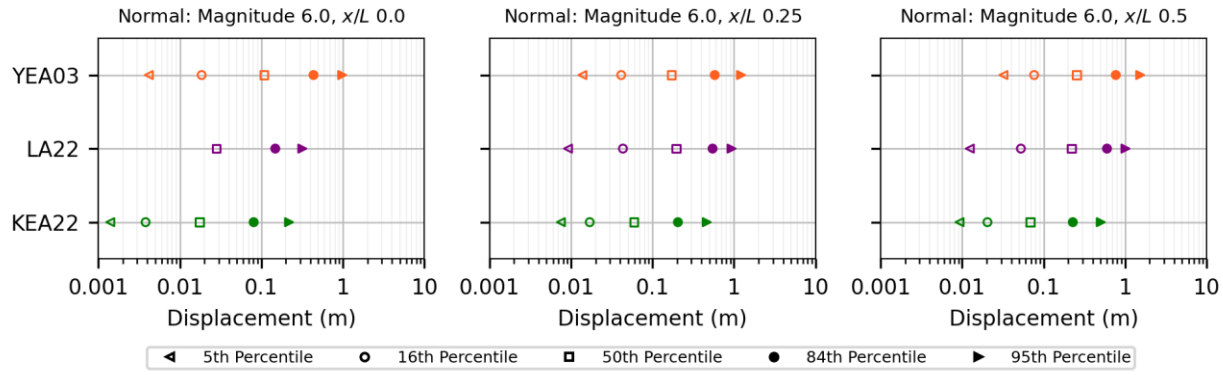

(b) Percentile displacement plots.

Figure 5.11. Comparison of aleatory variability for normal **M** 6.0.

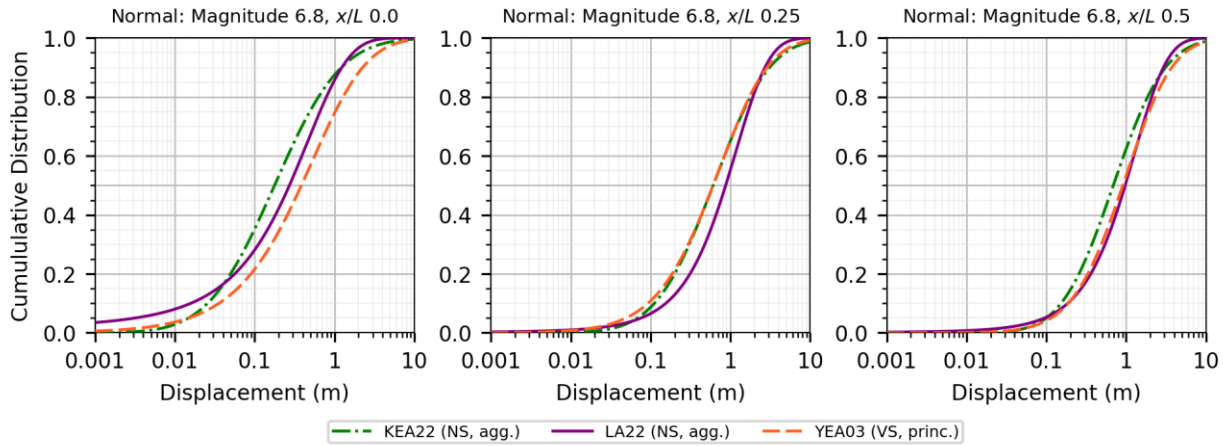

(a) Cumulative displacement probability curves.

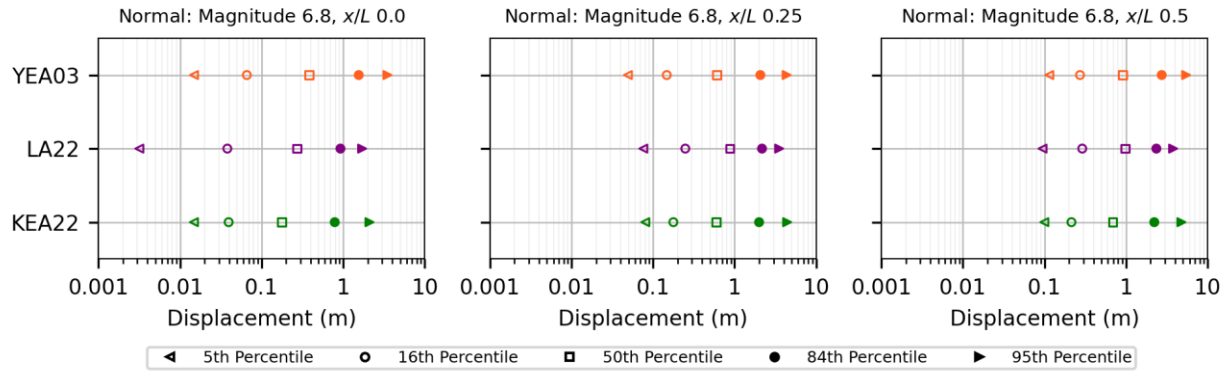

(b) Percentile displacement plots.

Figure 5.12. Comparison of aleatory variability for normal **M** 6.8.

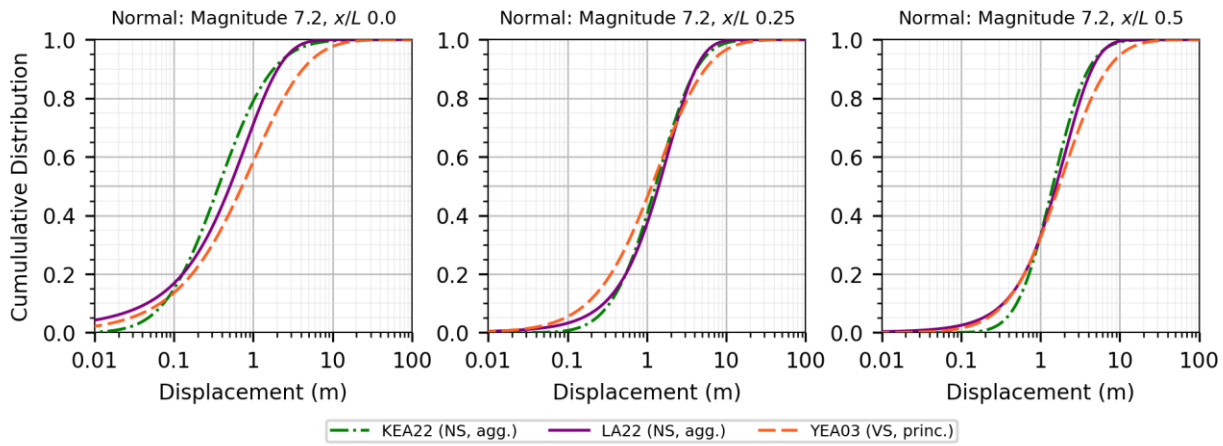

(a) Cumulative displacement probability curves.

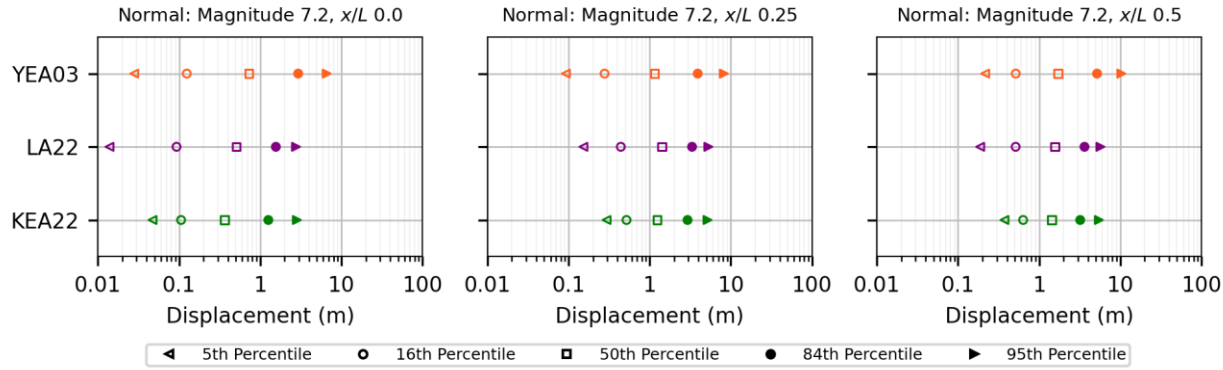

(b) Percentile displacement plots.

Figure 5.13. Comparison of aleatory variability for normal **M** 7.2.

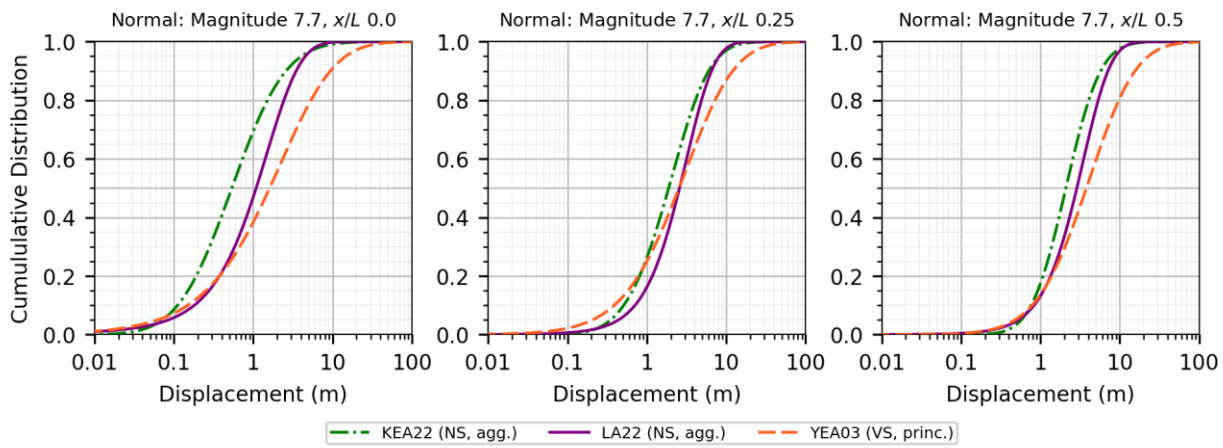

(a) Cumulative displacement probability curves.

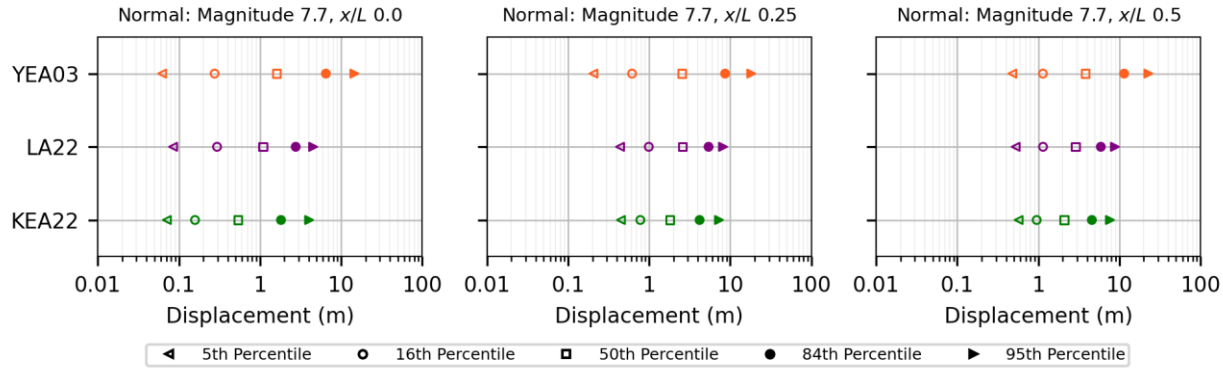

(b) Percentile displacement plots.

Figure 5.14. Comparison of aleatory variability for normal **M** 7.7.

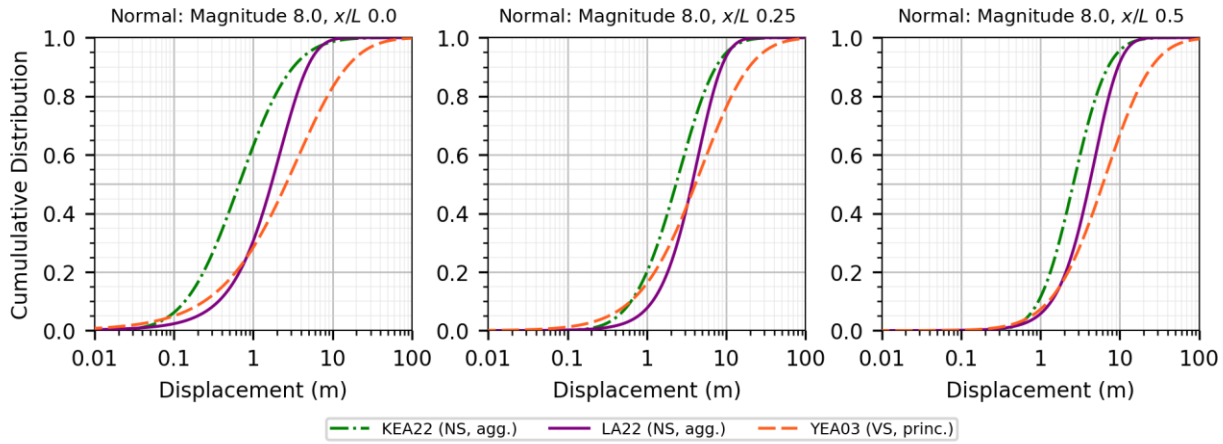

(a) Cumulative displacement probability curves.

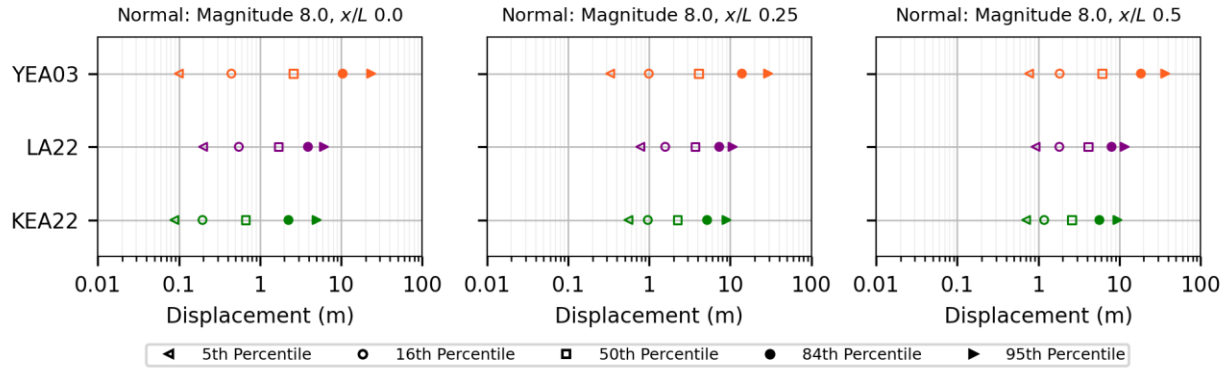

(b) Percentile displacement plots.

Figure 5.15. Comparison of aleatory variability for normal **M** 8.0.

5.2 HAZARD CURVES

Probability of exceedance curves are presented for a set of scenarios to provide model comparisons in hazard space. Other elements of a probabilistic fault displacement hazard analysis, such as fault activity rate and the conditional probability of surface rupture given magnitude and style of faulting (e.g., Wells and Coppersmith, 1993), are not included herein; however, the probability of rupture gaps in the LA22 model is included for the LA22 results in this section because their FDM formulation includes fault segmentation, and accounting for gaps between segments is required to capture the full distribution of displacements (i.e., zero and non-zero displacements).

Importantly, we note that while the displacement amplitude probability distributions in other models are also based on non-zero displacements, the conditional probability for rupture

gaps in the LA22 model, $P(D_{agg} = 0)$, should not be applied to the other FDMs used in this report because the other models were developed using data from the full rupture length and therefore capture segment behavior differently. Specifically, artifacts of segmentation such as the end-of-segment displacement amplitude tapering that occurs in the middle of ruptures (e.g., Figure 2.4a), is inherently captured in the within-event variability in the other models. However, because the LA22 model was developed using data from individual rupture segments, the within-event variability in their model is based on segment data and an additional aleatory variability model is used to capture the number, lengths, and locations of the segments. In other words, the LA22 gap probability model is integrated with their segmentation model, which forms the basis of their overall FDM, and is not applicable to other models.

Probability of exceedance curves are presented for all FDMs for **M** 6.0, 7.0, and 8.0 at the rupture endpoints and midpoint on Figures 5.16, 5.17, and 5.18 for strike-slip, reverse, and normal styles of faulting, respectively. The LA22 model results incorporate the gap probability model on Figure 5.19. The conditional gap probability is highest for normal faulting and lowest for strike-slip faulting. As well, the probability is negligible for small magnitudes at the rupture endpoints and increases with magnitude and normalized position along the rupture.

The probability of exceedance curves for strike-slip faulting are shown on Figure 5.16. The spread between all models is higher at rupture endpoints ($x/L = 0$). In general, the upper tails (which correspond to lower probabilities of exceedance) in the KEA22 model are wider than the CEA22 and LA22 models for the scenarios shown. The spread between new models is lowest for **M** 7.0, which is well-captured with 13 strike-slip events in the FDHI database (**M** 7.0 ± 0.3). At the **M** 7.0 midpoint ($x/L = 0.5$), the predicted displacements in the new FDMs are within a factor of 1.5 or better for exceedance probabilities ≤ 10^{-3}. In all cases, the new model predictions at the rupture midpoints are within a factor of three or better for exceedance probabilities ≤ 10^{-3} and within a factor of five or better at the rupture endpoints. Predicted displacements in the new models are higher at rupture endpoints than the PEA11 model in almost all cases; the exception is **M** 8.0, where the CEA22 prediction is lower for exceedance probabilities greater than about 2 x 10^{-3}. At the rupture midpoint, the new FDMs predict displacements that over 10 times lower than the PEA11 model for **M** 8.0 and generally more than three times lower for **M** 6.0; an exception is the KEA22 model, for which the **M** 6.0 midpoint prediction is similar to PEA11 due to the larger aleatory variability for small magnitude strike-slip events in their model.

Similar plots are shown on Figure 5.17 for reverse faulting. Again, the spread between all models is higher at rupture endpoints, and the KEA22 model upper tails are wider than the LA22 and MEA22 models. The predicted displacements in the new FDMs at the rupture midpoint are within a factor of 1.5 or better for exceedance probabilities ≤ 10^{-3} and within a factor of five or better at the rupture endpoints in all cases. At the **M** 6.0 and 7.0 rupture midpoint cases, the difference between the KEA22 and MR11 results is nil for exceedance probabilities greater than about 4 x 10^{-1}. At the rupture endpoints, the KEA22 model predictions are higher than the MR11 model across most of the hazard curve for the magnitudes considered. The other new models

produce displacements at least 1.5 times lower than the MR11 model at an exceedance probability of 10^{-3} for **M** 6.0 and 7.0 and more than two times lower for **M** 8.0 at both the rupture midpoint and end points.

Finally, Figure 5.18 provides similar plots for normal faulting. As with other styles of faulting, the spread between all models is higher at rupture endpoints, and the KEA22 model upper tails are wider than the LA22 model. The predicted displacements in the new FDMs are within a factor of three or better for exceedance probabilities $\leq 10^{-3}$ in all cases. As well, displacements in the new FDMs are lower than the YEA03 model in all cases. For example, at an exceedance probability of 10^{-3}, the predicted displacements in the new FDMs are more than 2.5 times lower for **M** 6.0 and over 10 times lower for **M** 8.0.

In summary, probability of exceedance curves are presented for six scenarios (**M** 6.0, 7.0, and 8.0 at x/L of 0 and 0.5) and all styles of faulting. The largest variability across all models occurs at rupture endpoints. This is expected due to relatively limited data at rupture endpoints and different profile shapes used in each model (Table 4.1; Figure 4.1a) and is consistent with results presented elsewhere in this report (e.g., Chapter 5.1). Furthermore, the upper tails (which correspond to lower probabilities of exceedance) in the KEA22 model are generally wider than the other new models because the KEA22 model uses a lognormal distribution and the other new models use asymmetric probability distributions that broader lower tails and narrower upper tails. The following observations summarize the probability of exceedance comparisons between the new models:

- Displacements at rupture endpoints ($x/L = 0$) are within a factor of two for all styles and all magnitudes considered at an exceedance probability of 10^{-1}.
- Displacements at the rupture midpoint ($x/L = 0.5$) are within a factor of about 1.5 for **M** 7.0 and 8.0 a factor of about two for **M** 6.0 at an exceedance probability of 10^{-1} for all styles.
- Displacements at rupture endpoints are within a factor of five for strike-slip and reverse faulting and a factor of three for normal faulting at an exceedance probability of 10^{-3} for all magnitudes considered.
- Displacements at the rupture midpoint are within a factor of three for all styles and all magnitudes considered at an exceedance probability of 10^{-3}, and within a factor of two in most cases.
- For strike-slip faulting, the new models produce displacements greater than the existing PEA11 model at the rupture endpoints across the full hazard curve in most cases. At the rupture midpoint, displacements from the new models are lower than the PEA11 model at exceedance probabilities less than about 4×10^{-1} to 10^{-1} (depending on the magnitude) (an exception is the KEA22 model for **M** 6.0, for which the midpoint prediction is similar to PEA11).

- For reverse faulting, two of the new models (MEA22 and LA22) produce displacements lower than the existing MR11 model at exceedance probabilities less than about 10^{-1} (varies by scenario). The KEA22 model produces displacements that are higher than the MR11 model across most of the hazard curve at the rupture endpoints. At the rupture midpoint, the KEA22 model displacements are lower than the MR11 model for **M** 8.0, whereas the KEA22 and MR11 hazard curves are similar for **M** 6.0 and 7.0.
- For normal faulting, the new models produce displacements lower than the existing YEA03 model across the full hazard curve for the scenarios presented.

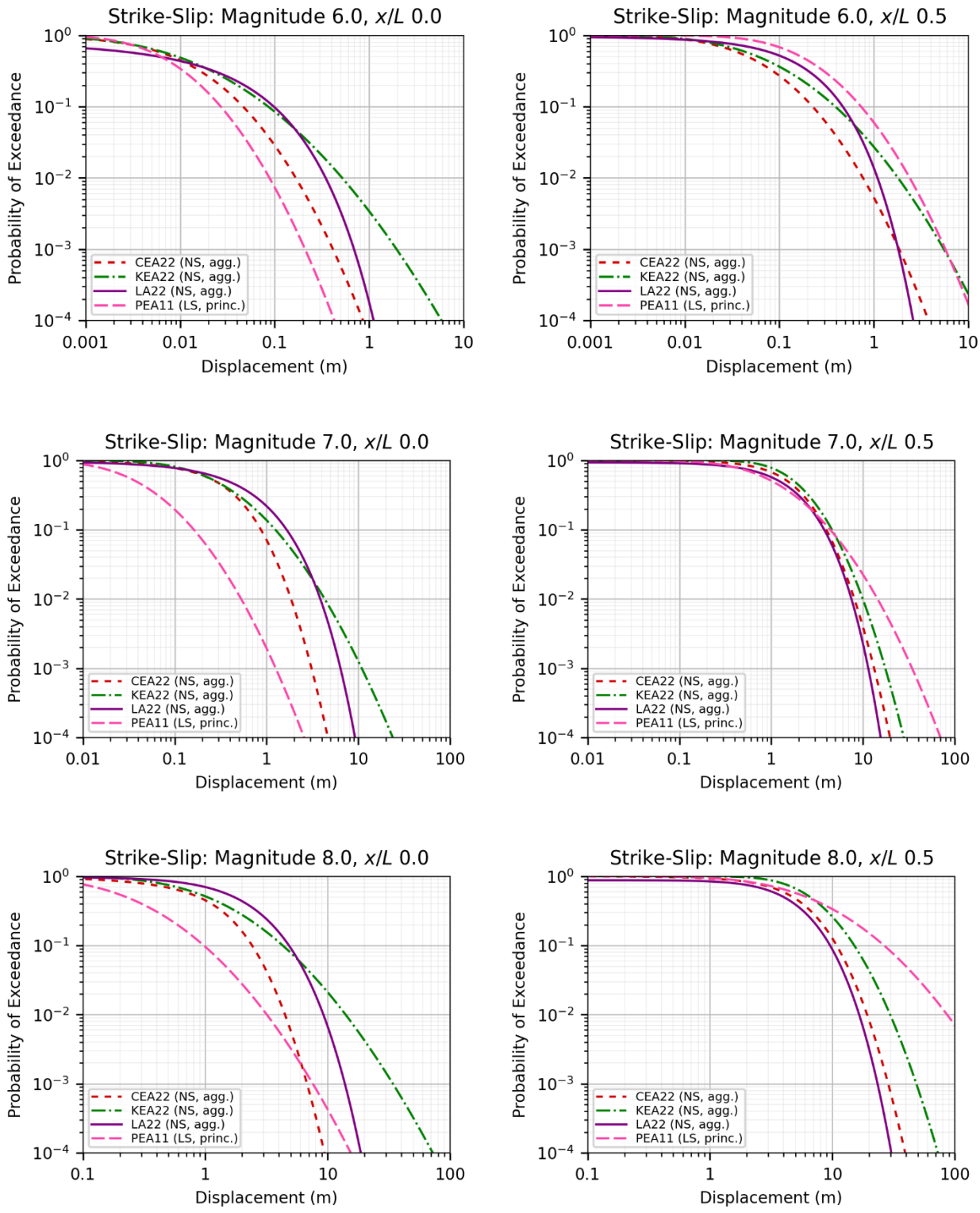

Figure 5.16. Probability of exceedance curves for strike-slip style of faulting. NS = net slip component; LS = lateral slip component (see Chapter 2 for slip component discussion).

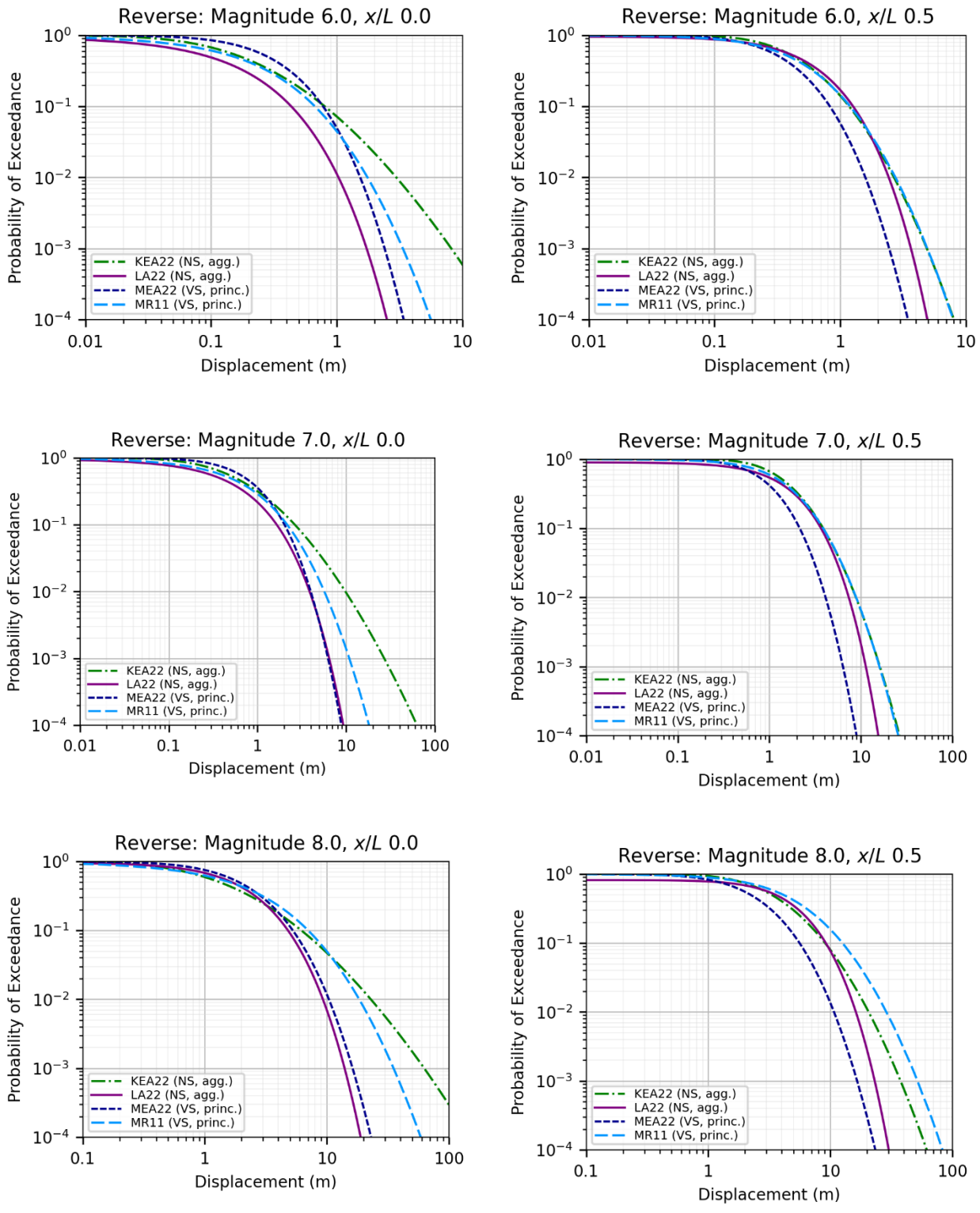

Figure 5.17. Probability of exceedance curves for reverse style of faulting. NS = net slip component; VS = vertical slip component (see Chapter 2 for slip component discussion).

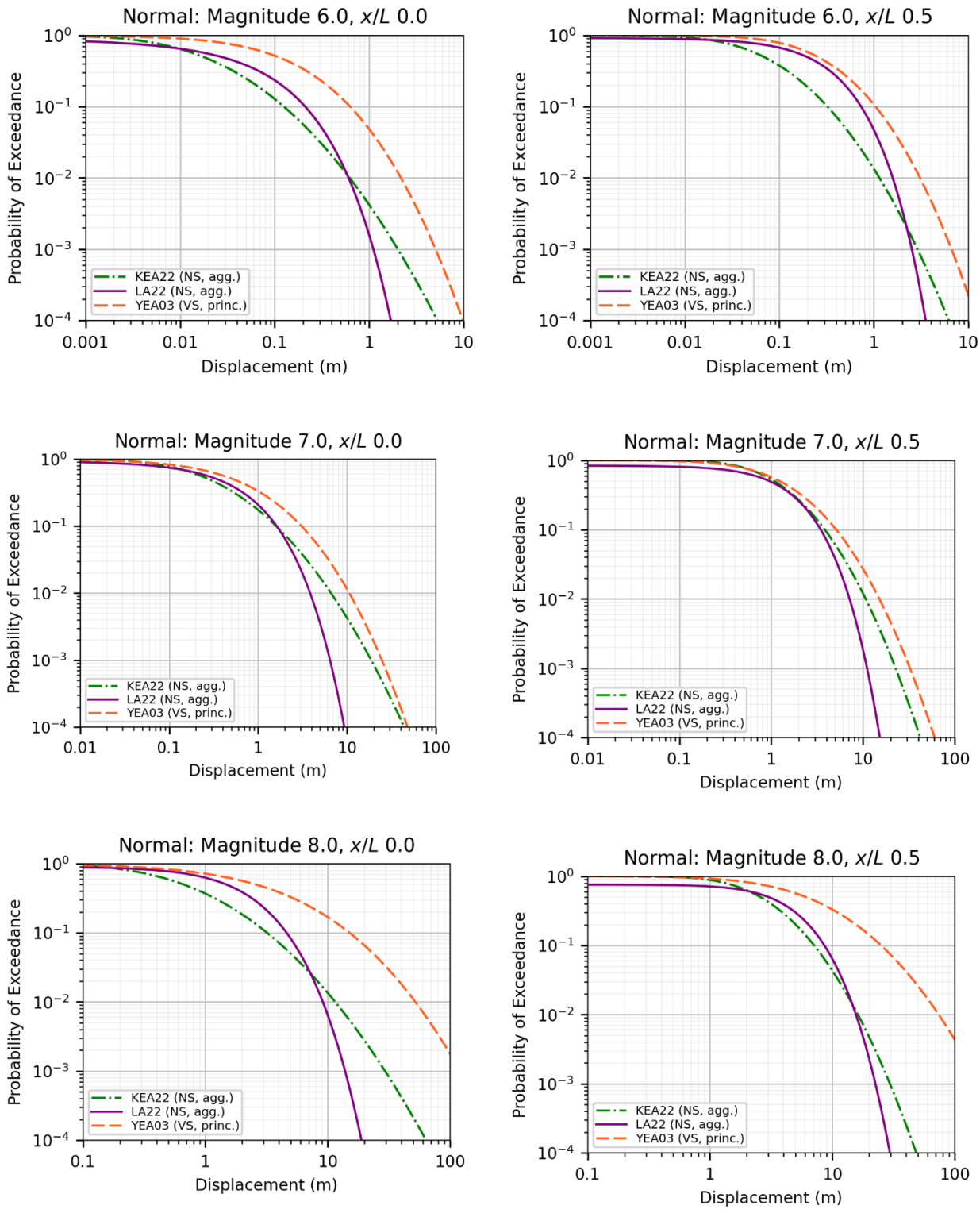

Figure 5.18. Probability of exceedance curves for normal style of faulting. NS = net slip component; VS = vertical slip component (see Chapter 2 for slip component discussion).

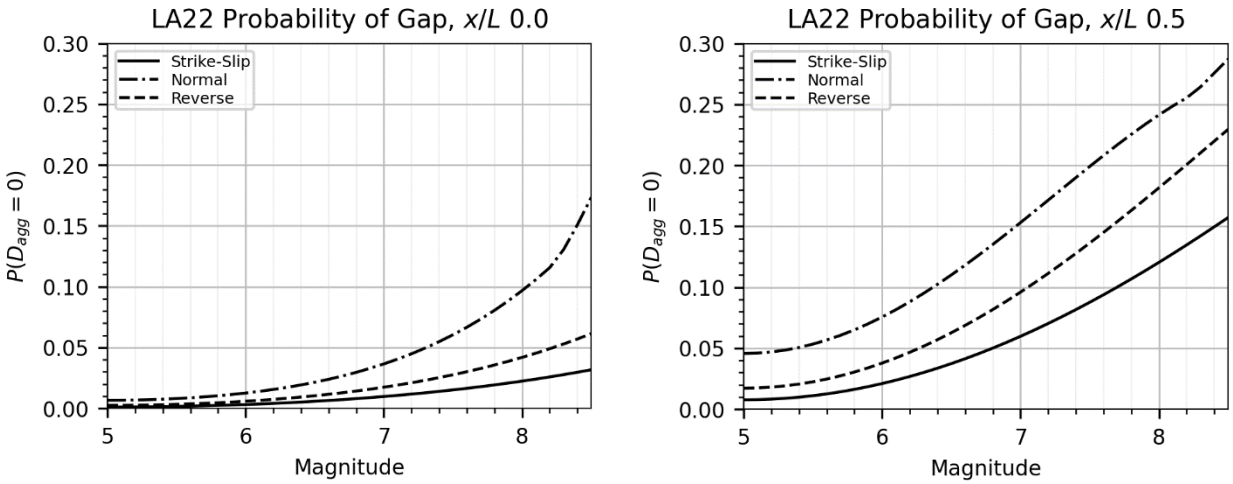

(a) For rupture endpoints.

(b) For rupture midpoint.

Figure 5.19. Rupture gap probability model used in LA22 probability of exceedance calculations. Note that the model is only applicable to the LA22 FDM; see text for discussion.

6 Within-Model Epistemic Uncertainty

This chapter summarizes the within-model epistemic uncertainty in the new FDMs. Each model handles epistemic uncertainty differently. For example, two alternative prediction formulations are provided in MEA22. Both LA22 and KEA22 provide estimates of the epistemic uncertainty in the median predicted displacement, and KEA22 also provides estimates of the uncertainty in the standard deviation. The CEA22 model provides alternative magnitude scaling models for the $nEMG$ distribution. (Other CEA22 formulations, such as the unfolded $nEMG$ distribution and alternative probability distributions, are not evaluated herein.)

The within-model epistemic uncertainty is discussed for each model separately below. Comparisons are made in hazard space for a range of scenarios (i.e., magnitude and normalized position along the rupture). Specifically, the results from the rupture endpoint and midpoint for three magnitudes (**M** 6.0, 7.0, and 8.0) are evaluated. These combinations capture a representative range of scenarios and are within the recommended limits of each model (Table 3.3). The results are shown as probability of exceedance curves for comparisons purposes; however, other factors such as the conditional probability of surface rupture given magnitude and style of faulting (e.g., Wells and Coppersmith, 1993) and activity rate vertically scale the curves in a hazard analysis and are not included herein.

6.1 MEA22 MODEL

The MEA22 model provides two alternative formulations. The D/MD relationship is the preferred alternative (Moss, R., pers. comm.), and the discussions and calculations in Chapters 3, 4, and 5 used this formulation. Here we compare D/MD relationship and the alternative D/AD formulation in MEA22. We note that because these formulations predict different response variables, this technically is not a within-model epistemic uncertainty, but the comparisons are provided here for completeness.

Comparisons are shown in hazard space for each model formulation on Figures 6.1 and 6.2. The calculations include aleatory variability in the MD and AD terms, as described at the beginning of Chapter 5. The hazard from the D/AD model is higher in all cases, although the difference at the rupture midpoint is small (only about 10% at probabilities of exceedance of 10^{-3}).

At the rupture endpoints, the D/AD model is roughly 30% higher at probabilities of exceedance of 10^{-3}.

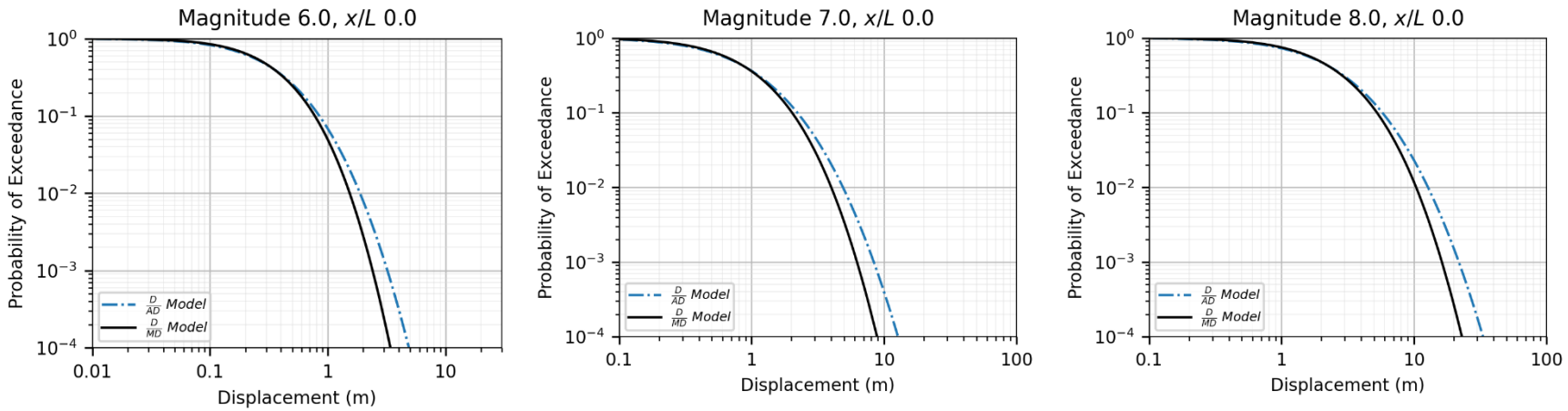

Figure 6.1. Comparison of MEA22 $\boldsymbol{D/MD}$ and $\boldsymbol{D/AD}$ model formulations at rupture endpoints.

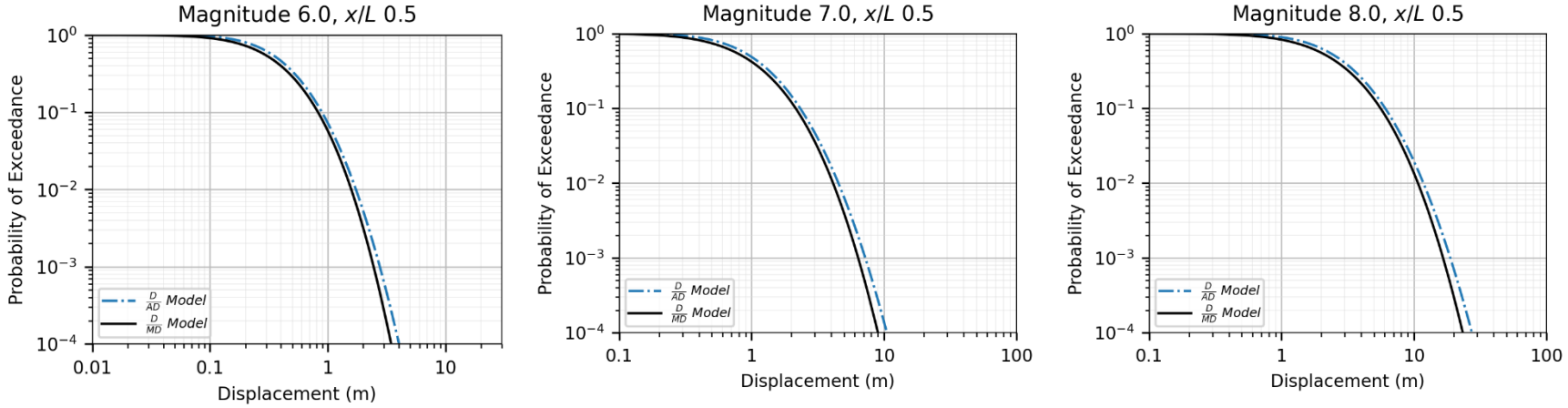

Figure 6.2. Comparison of MEA22 $\boldsymbol{D/MD}$ and $\boldsymbol{D/AD}$ model formulations at rupture midpoints.

6.2 KEA22 MODEL

The KEA22 model coefficients were developed using Bayesian inference. As a result, the coefficients are defined by statistical distributions rather than point estimates that are produced by the other models, which use linear regression with maximum likelihood estimation. The authors provide a set of 2000 correlated coefficients sampled from the posterior distributions to represent the full within-model epistemic uncertainty. However, the epistemic uncertainty can be more efficiently approximated by obtaining standard deviations of the 2000 median and standard deviation predictions from a lookup table and using a three-point approximation of a normal distribution (Kuehn, N., pers. comm.) (e.g., Keefer and Bodily, 1983). Figure 6.3 shows the logic tree implementation.

The standard deviations of the median prediction are shown on Figure 6.4 as a function of normalized position along rupture and magnitude for each style of faulting. Similarly, Figure 6.5 shows the standard deviations of the predicted total standard deviation. Figures 6.4 and 6.5 were created from the lookup tables provided by the KEA22 model developers.

Comparisons are shown in hazard space with and without epistemic uncertainty on Figures 6.6 through 6.11. The calculations are shown for folded position along rupture. The mean model on each figure corresponds to the base model used in the comparisons in Chapters 4 and 5 (i.e., calculations performed using the mean coefficients). Including epistemic uncertainty increases the hazard relative to the base mean model. The impact of including epistemic uncertainty varies, but it is highest for normal events and lowest for reverse events, higher at rupture midpoints than endpoints for all styles of faulting, and generally higher for smaller magnitudes. The impact is lowest for reverse events because the standard deviations are lowest for this style of faulting (Figures 6.4 and 6.5). Similarly, normal events have the highest standard deviations.

The following observations summarize the comparisons between the mean hazard curves with and without epistemic uncertainty for probabilities of exceedance of 10^{-3}:

- For strike-slip faulting, the results are about two times higher for **M** 6.0 and about 20% higher for **M** 7.0 and 8.0.
- For reverse faulting, the results are about 20% higher for all magnitudes considered.
- For normal faulting, the results are about 2.5 times higher for **M** 6.0 and about 50% higher for **M** 7.0 and 8.0.

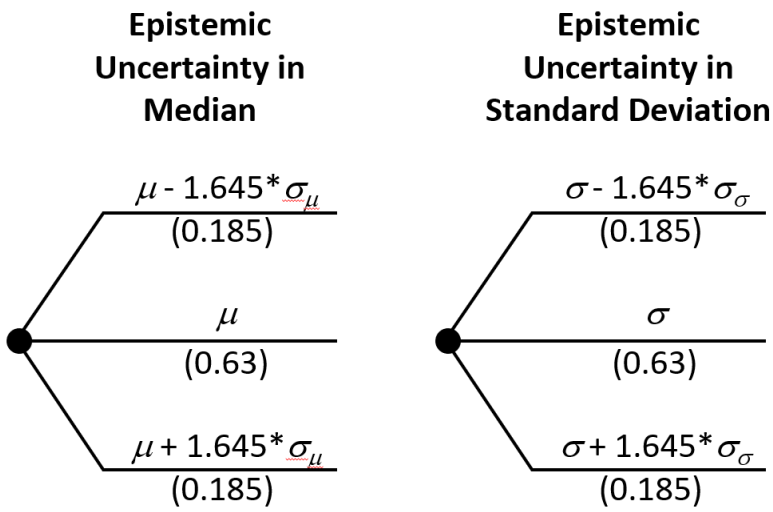

Figure 6.3. Logic tree for capturing epistemic uncertainty in median prediction $\boldsymbol{\mu}$ and standard deviation $\boldsymbol{\sigma}$ in KEA22 model.

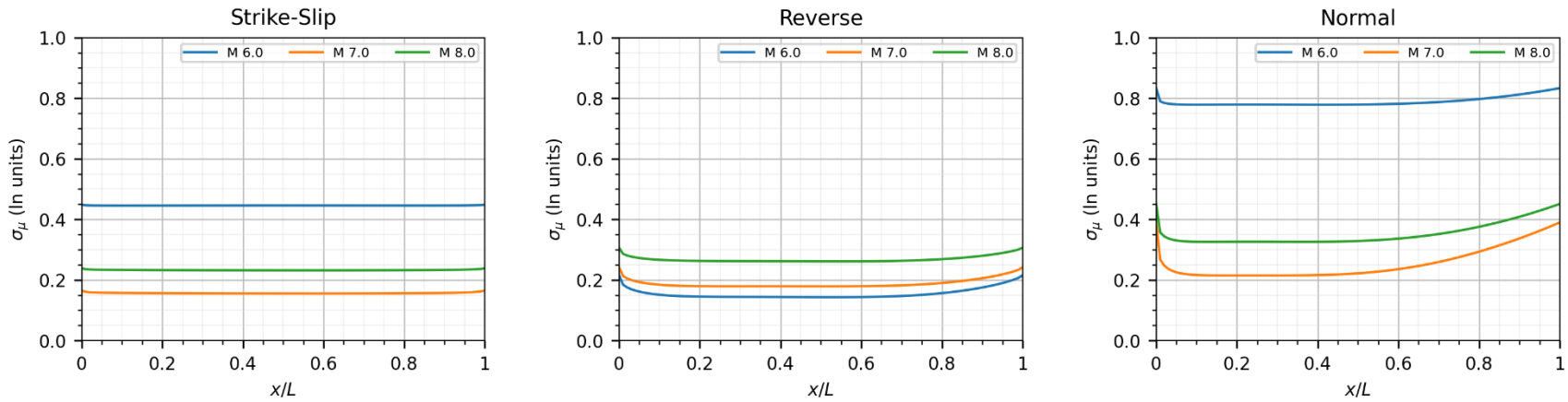

Figure 6.4. KEA22 epistemic uncertainty model for the predicted median (μ).

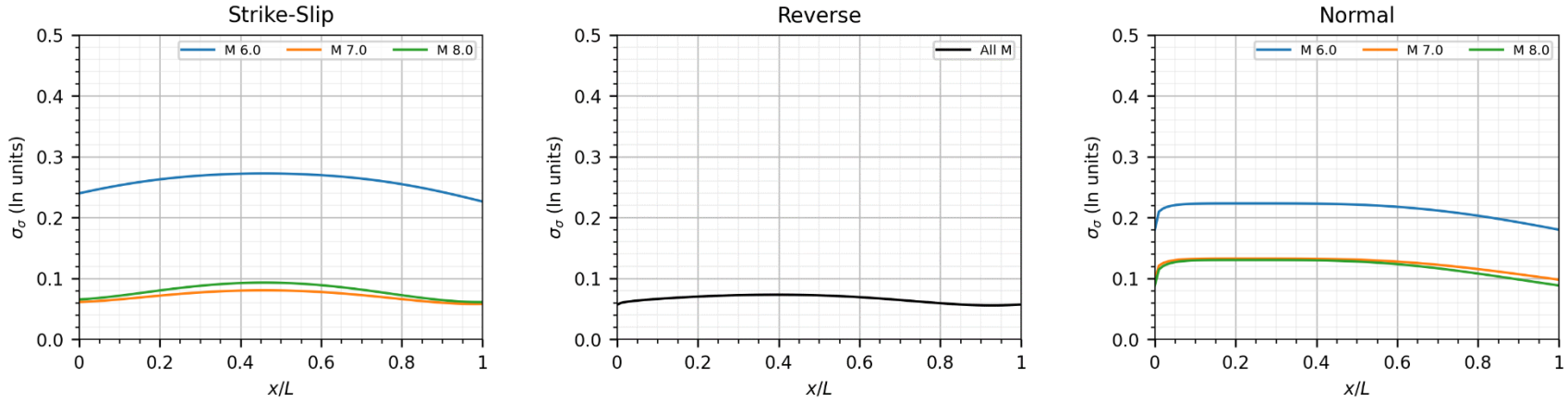

Figure 6.5. KEA22 epistemic uncertainty model for the predicted standard deviation (σ).

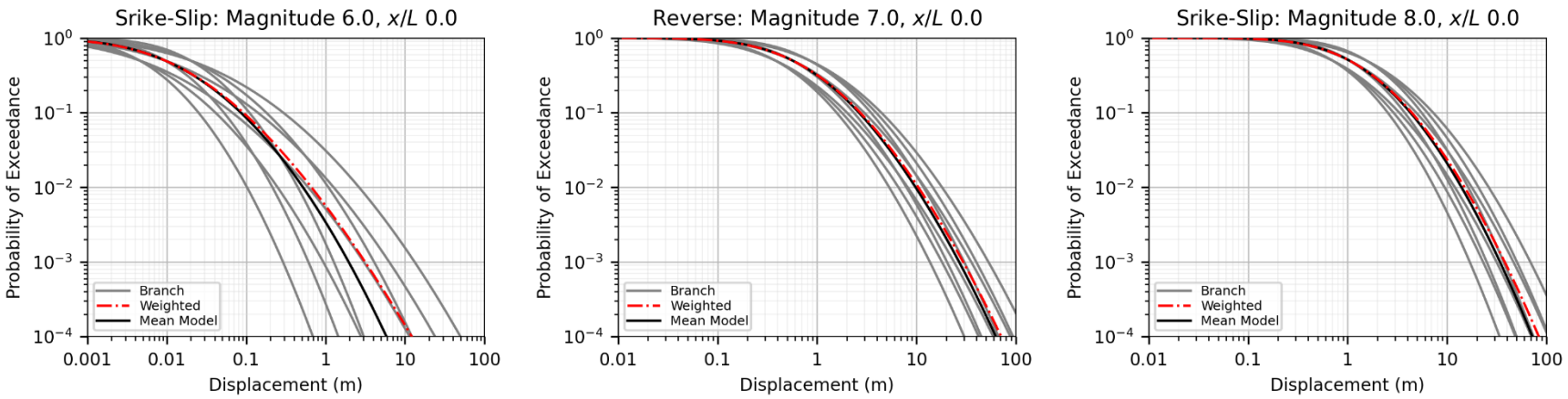

Figure 6.6. Comparison of KEA22 within-model epistemic uncertainty at rupture endpoints for strike-slip events.

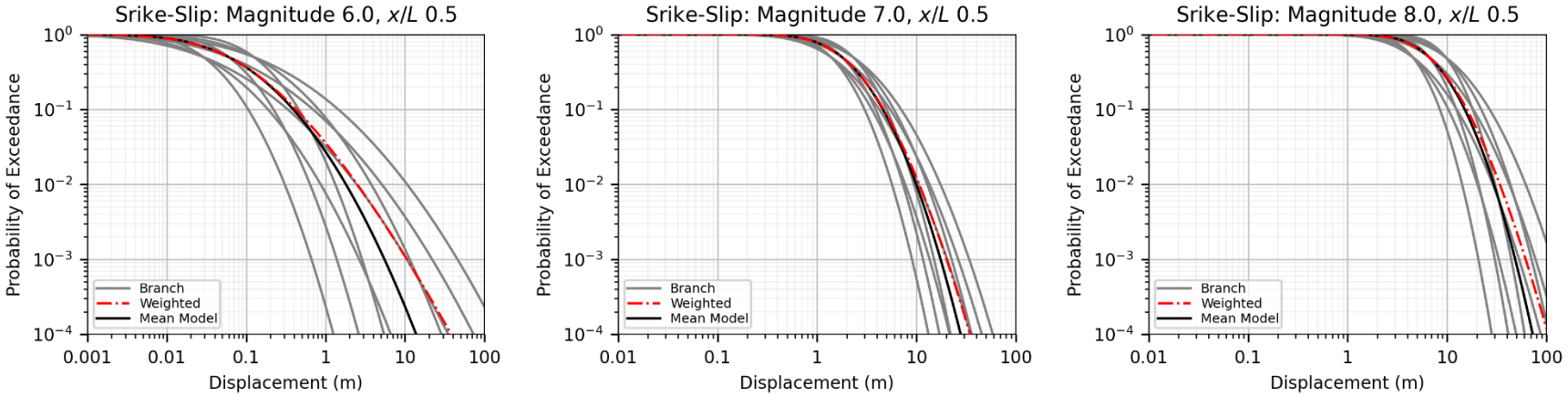

Figure 6.7. Comparison of KEA22 within-model epistemic uncertainty at rupture midpoints for strike-slip events.

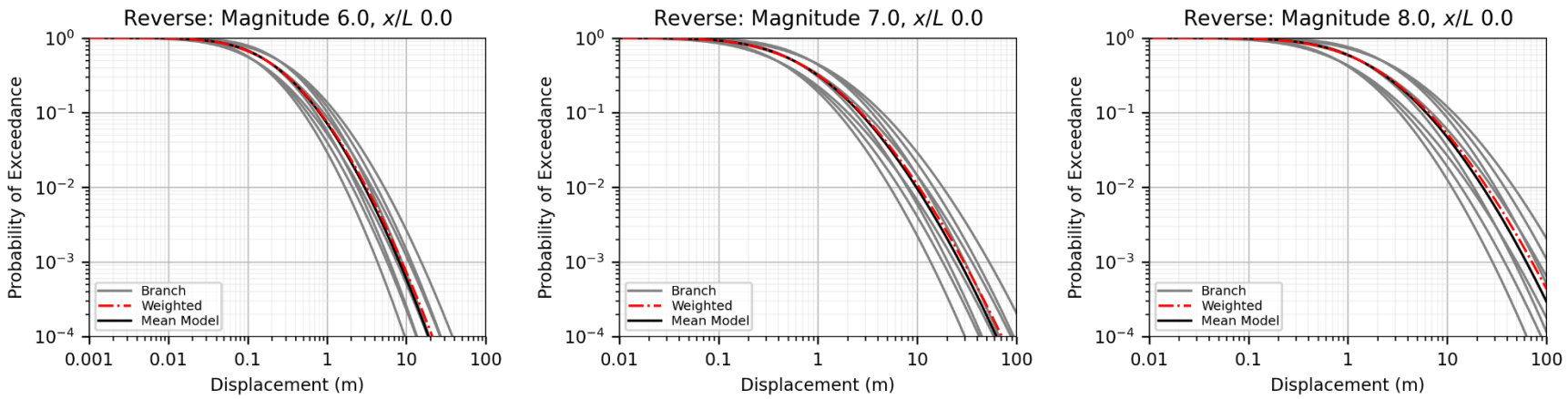

Figure 6.8. Comparison of KEA22 within-model epistemic uncertainty at rupture endpoints for reverse events.

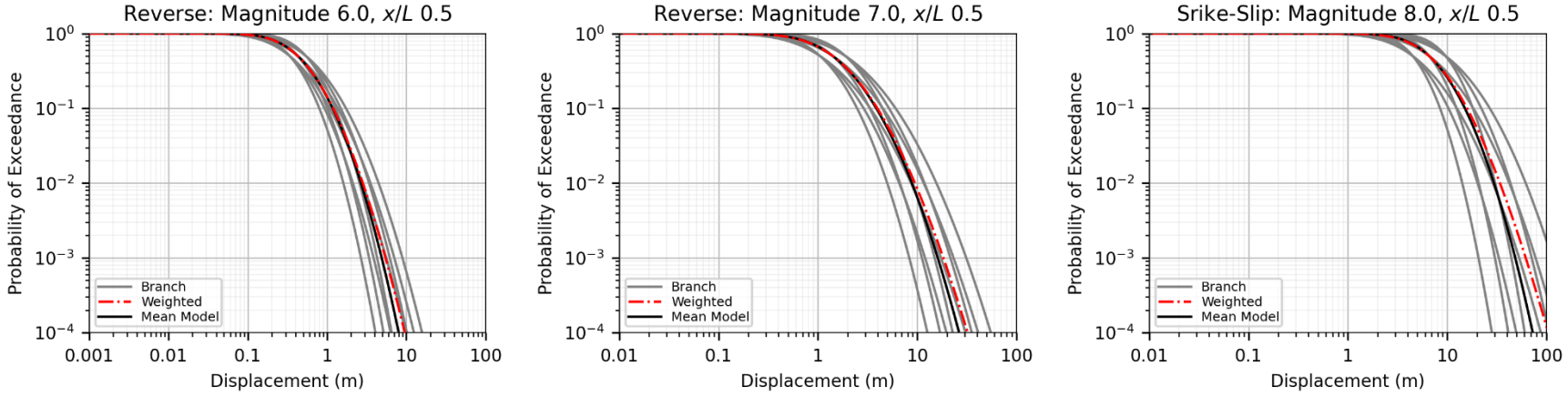

Figure 6.9. Comparison of KEA22 within-model epistemic uncertainty at rupture midpoints for reverse events.

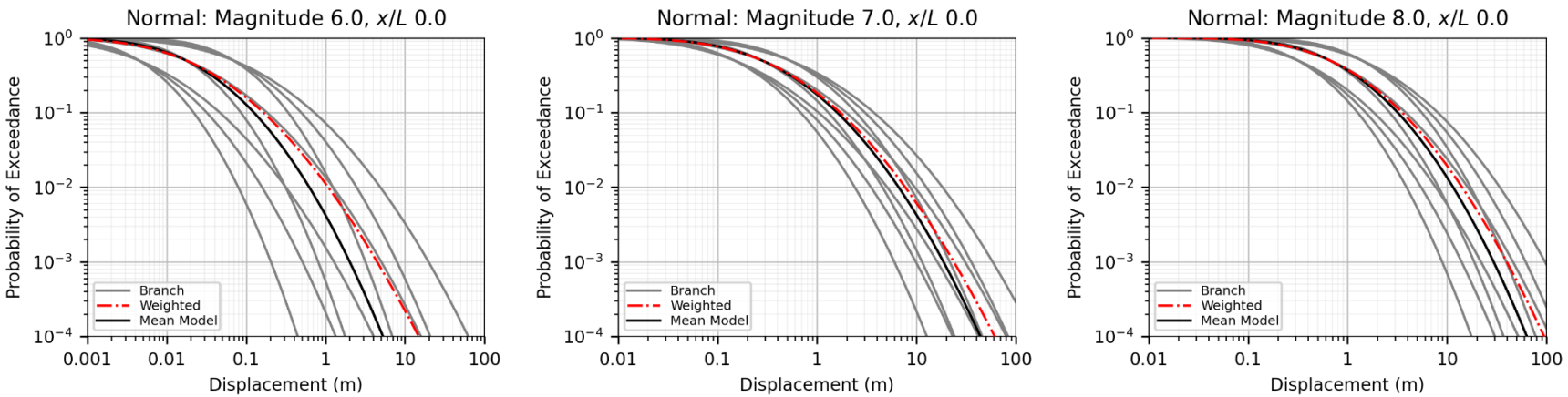

Figure 6.10. Comparison of KEA22 within-model epistemic uncertainty at rupture endpoints for normal events.

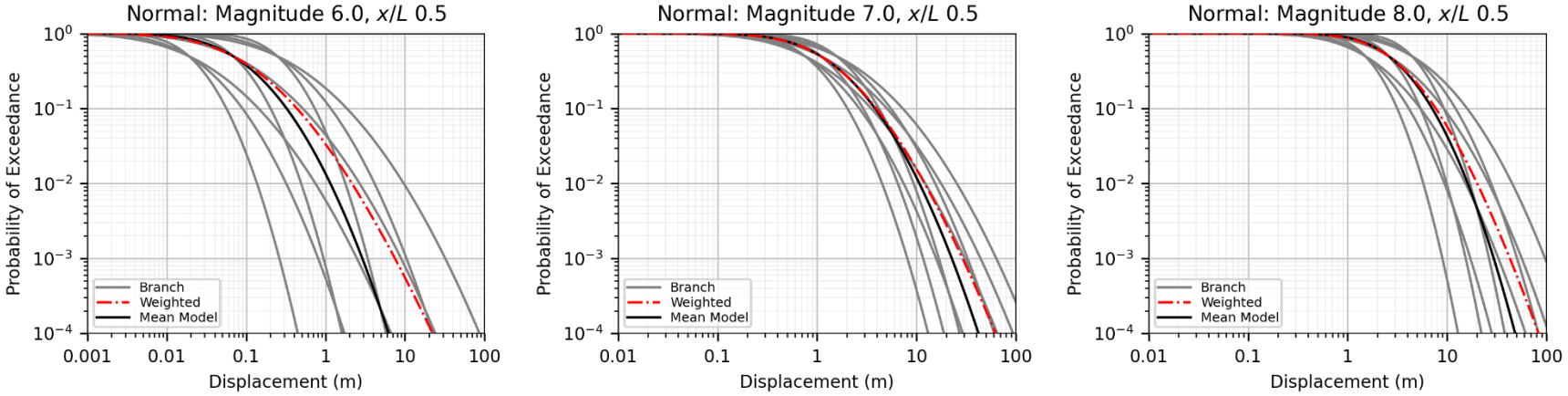

Figure 6.11. Comparison of KEA22 within-model epistemic uncertainty at rupture midpoints for normal events.

6.3 CEA22 MODEL

The CEA22 model provides alternative magnitude scaling models for the $nEMG$ probability distribution. All alternatives use bi-linear magnitude scaling, but the magnitude breakpoint (m_b) is varied in the alternatives. Their preferred model places the breakpoint at **M** 7.1, and the three alternatives use breakpoints at **M** 6.4, 6.75, and 7.32. Separate (correlated) model coefficients are provided in CEA22 for each alternative. In addition to alternatives for the $nEMG$ distribution, the CEA22 model also developed models for other probability distributions (e.g., skew-normal and skew-t). For brevity, only the $nEMG$ distribution alternatives are evaluated here. We note that the $nEMG$ formulation is preferred by the CEA22 model developers.

Comparisons are shown in hazard space on Figures 6.12 and 6.13 for each alternative magnitude scaling model for the $nEMG$ probability distribution. The impact of the different models varies by magnitude, as expected, such that the smaller magnitude breakpoints produce higher hazard for larger magnitude events, and vice-versa. At probabilities of exceedance of 10^{-3}, the displacements in the different models vary by a factor of about 1.3 for **M** 6.0 and less than two for **M** 8.0. The impact for **M** 7.0 is small at probabilities of exceedance greater than about 10^{-2} and nil otherwise.

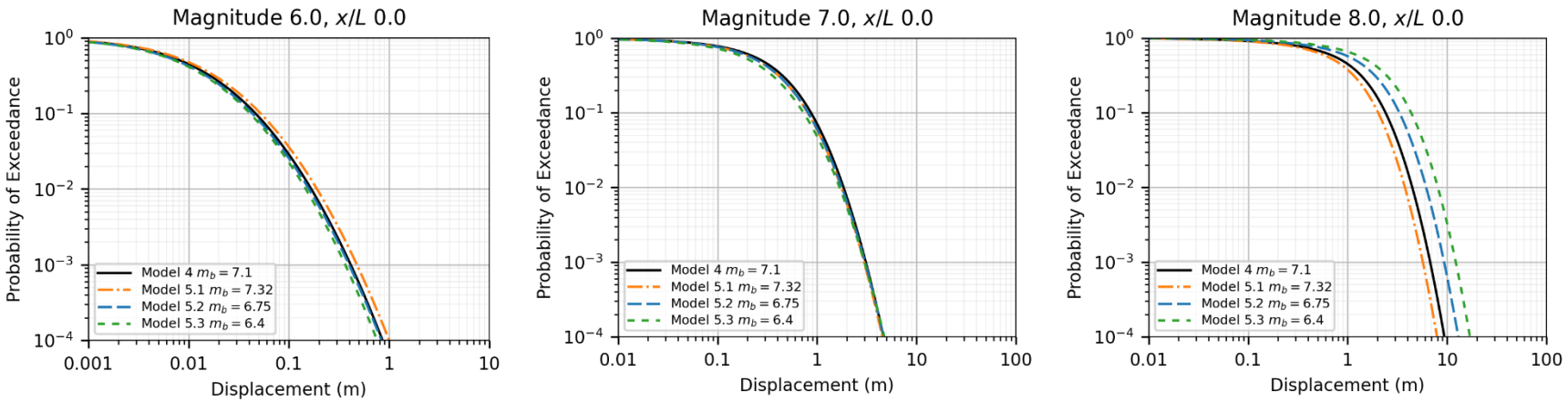

Figure 6.12. Comparison of CEA22 within-model epistemic uncertainty at rupture endpoints. $\boldsymbol{m_b}$ is magnitude breakpoint; see text for discussion.

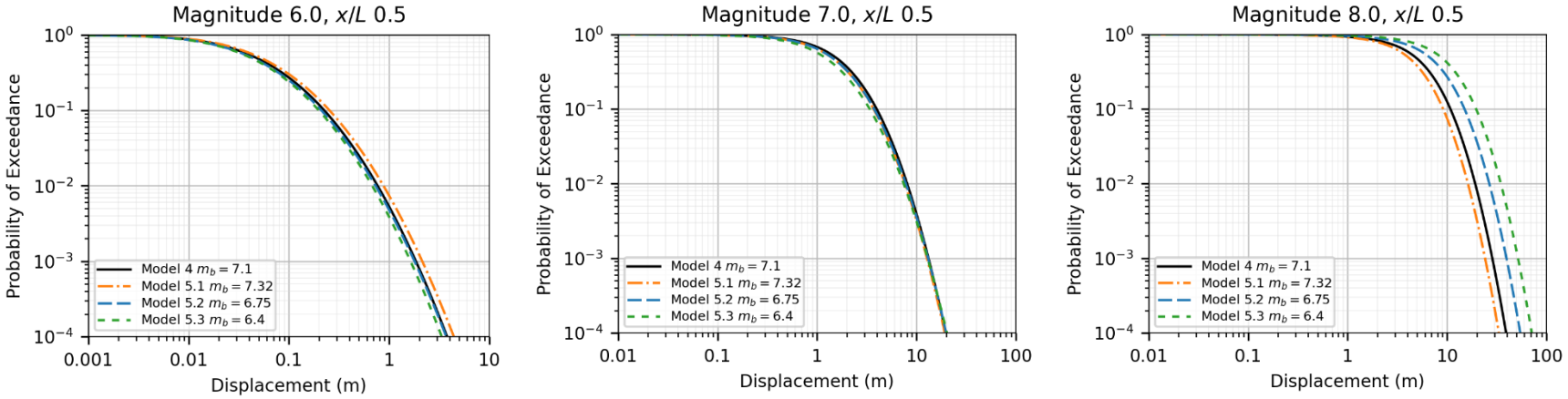

Figure 6.13. Comparison of CEA22 within-model epistemic uncertainty at rupture midpoints.

6.4 LA22 MODEL

The LA22 model provides estimates of the epistemic uncertainty in the median predicted displacement. Specifically, they provide a magnitude- and style-dependent standard deviation on the median, which can be captured with a three-point approximation of a normal distribution (Keefer and Bodily, 1983) using the logic tree on Figure 6.3. Note that only the epistemic uncertainty in the median on Figure 6.3 (i.e., left column) is used as the LA22 model does not provide uncertainty for the standard deviation. The epistemic uncertainty depends on magnitude and style of faulting (Figure 6.14).

The results in this section are for aggregated displacement and include the conditional probability that a site location is within a gap between segments. As discussed at the beginning of Chapter 5, the LA22 gap probability model, $P(D_{agg} = 0)$, on Figure 5.19 should be included in hazard calculations for aggregated displacement. Uncertainty in the gap probability is not provided in the LA22 model; therefore, all branches are scaled-down by the same amount. We also note that the LA22 gap probability model is not applicable to other FDMs, as explained in Chapter 5.2.

Comparisons are shown in hazard space with and without epistemic uncertainty on Figures 6.15 through 6.20. The central (μ) branch on each figure corresponds to the base model used in the comparisons in Chapters 4 and 5. The impact of including epistemic uncertainty is largest for small magnitudes (Figure 6.14). For the **M** 6.0 cases, including epistemic uncertainty increases the hazard by roughly 10% for strike-slip and reverse events at both the rupture endpoints and midpoint at probabilities of exceedance of 10^{-3}. For normal faulting, the increase is about 40% at the rupture endpoints and 20% at the midpoint.

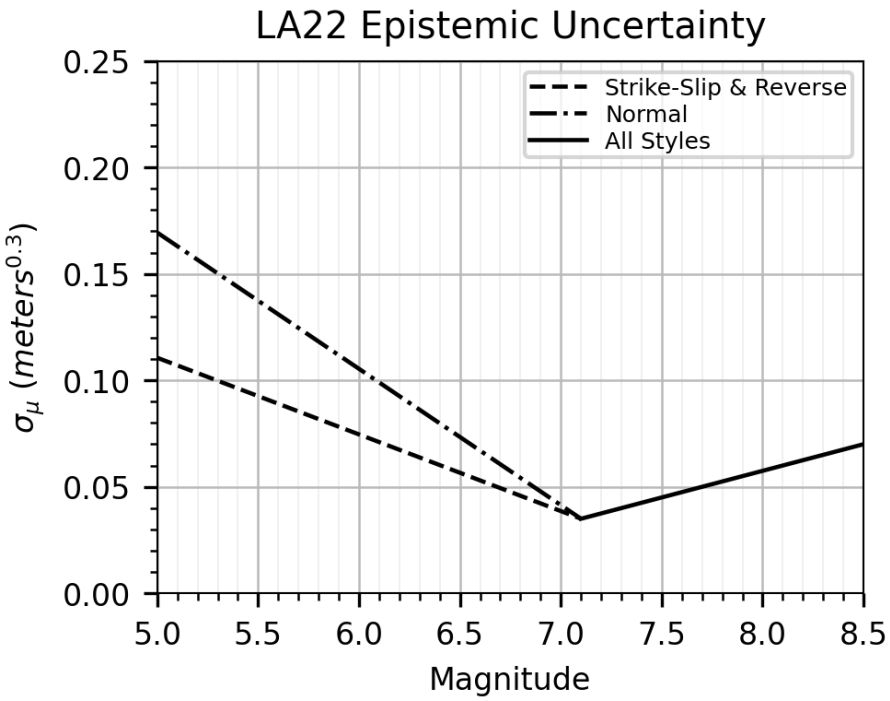

Figure 6.14. LA22 epistemic uncertainty model for the predicted median (μ).

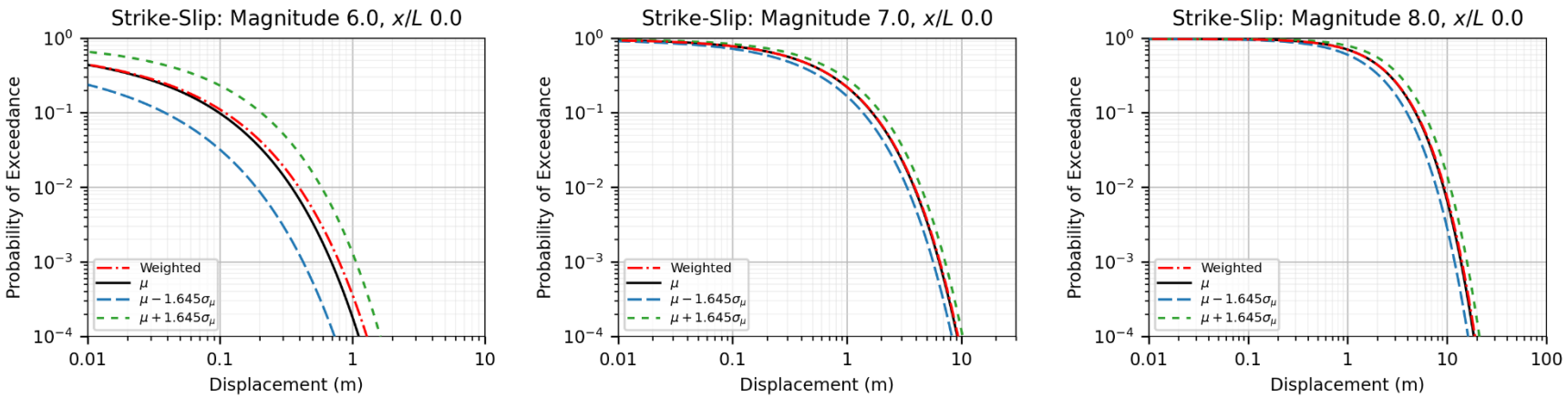

Figure 6.15. Comparison of LA22 within-model epistemic uncertainty at rupture endpoints for strike-slip events.

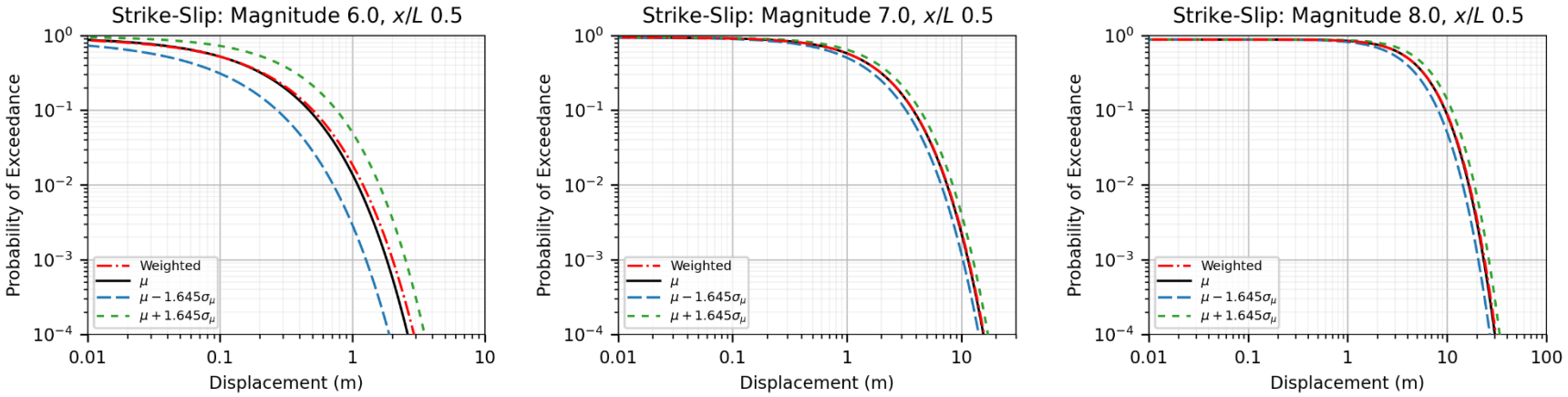

Figure 6.16. Comparison of LA22 within-model epistemic uncertainty at rupture midpoints for strike-slip events.

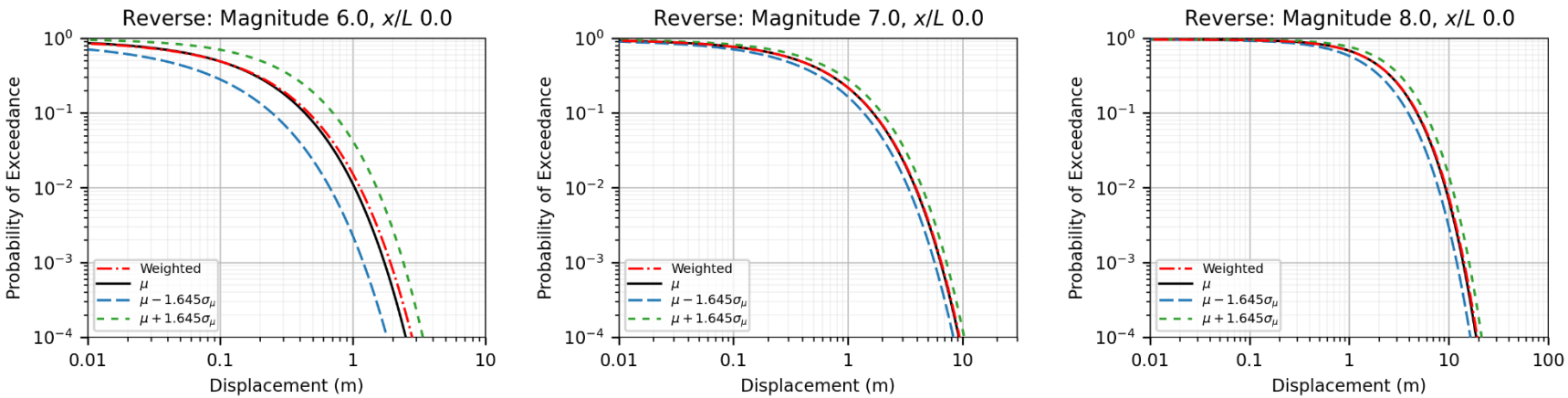

Figure 6.17. Comparison of LA22 within-model epistemic uncertainty at rupture endpoints for reverse events.

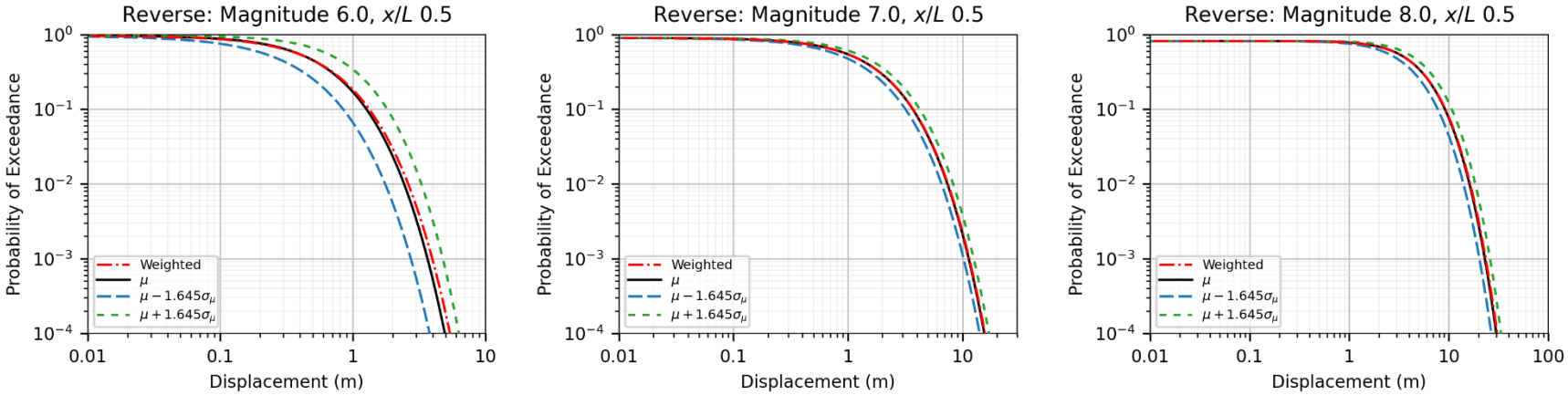

Figure 6.18. Comparison of LA22 within-model epistemic uncertainty at rupture midpoints for reverse events.

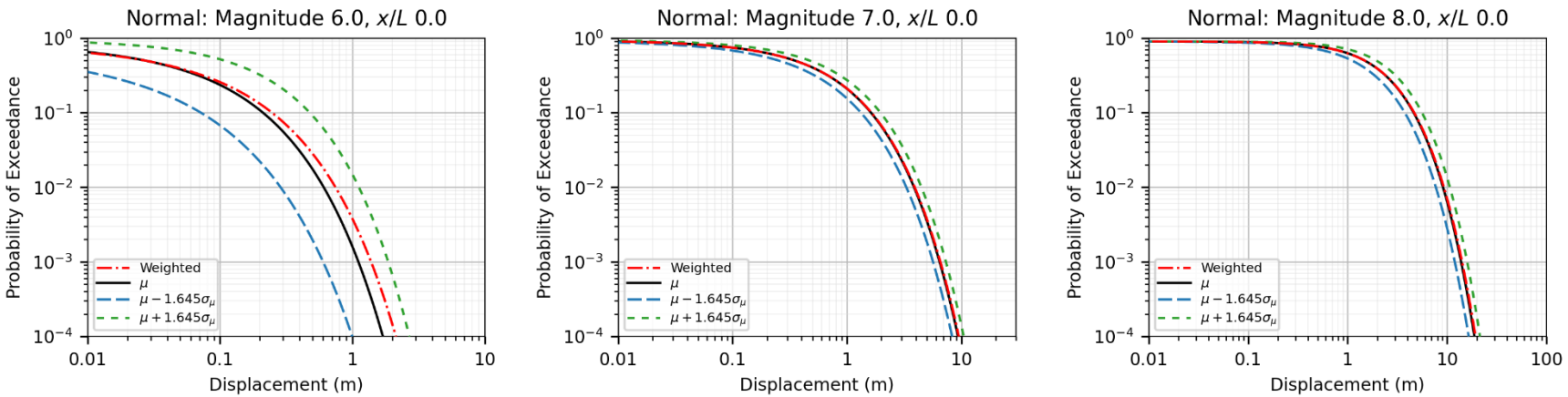

Figure 6.19. Comparison of LA22 within-model epistemic uncertainty at rupture endpoints for normal events.

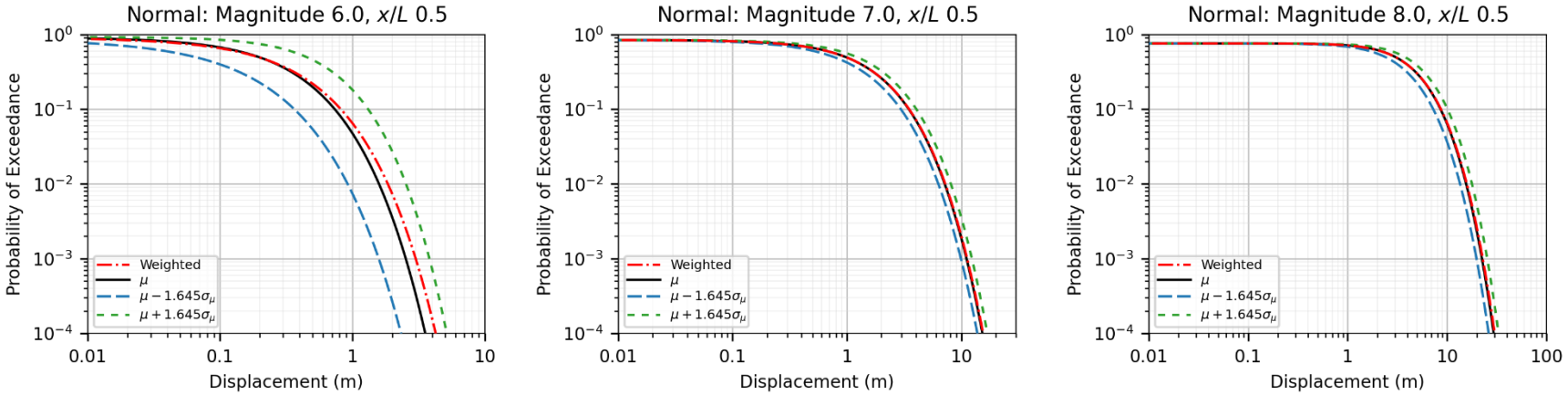

Figure 6.20. Comparison of LA22 within-model epistemic uncertainty at rupture midpoints for normal events.

7 Summary

Four new fault displacement amplitude prediction models were developed for principal ruptures through the FDHI Project. The models predict displacement as a function of moment magnitude, normalized position along rupture length, and style of faulting. Additionally, a new surface rupture length model by Lavrentiadis et al. (2022b) can be used to convert normalized rupture positions to absolute lengths for practical applications.

The new FDMs are a significant improvement over existing models in several ways:

1. The new database development included an extensive and systematic data quality review that was completed in coordination with the model developers. The use of a common and comprehensive database makes individual models more stable and comparisons between models more robust.
2. Most of the new models include magnitude scaling breakpoints to better capture magnitude dependence of the median predictions.
3. The new models use advanced statistical modeling techniques to better capture aleatory variability. For example, most new models partition the aleatory variability into between- and within-event components, which avoids bias towards better-sampled events. In most cases, the aleatory variability models are magnitude- and location-dependent, which improves hazard estimates because data dispersion is not constant for all magnitudes or positions along the rupture.
4. All new models provide some form of within-model epistemic uncertainty. The KEA22 and LA22 models provide epistemic uncertainty in the median prediction, and the KEA22 model also provides epistemic uncertainty in the standard deviation prediction. The CEA22 and MEA22 models provide alternative formulations to capture within-model epistemic uncertainty.
5. Finally, developing models through a coordinated research program allowed for extensive interaction and fruitful technical discussions between modeling teams and database developers that improved individual models and would otherwise be unavailable on an isolated team.

This report provides a comparison of the four new FDMs and three existing FDMs. Each FDM predicts displacement or normalized displacement as a probability distribution, and the prediction is a function of earthquake size and normalized position along the rupture length. Accordingly, each FDM consists of three key elements: (1) the prescribed shape of the median profile; (2) scaling of the profile amplitude with earthquake size; and (3) the statistical distribution selected to predict displacement, including the treatment of aleatory variability. These are technical decisions made by the model developers, and differences between the model results are due to differences in these elements of the models. For example, the end-of-rupture tapering in profile shape can lead to significant differences in predictions within ±15% of the rupture endpoints as well as the average displacement. The bi-linear magnitude scaling used in the new KEA22 and CEA22 models for strike-slip and normal faulting produces significantly lower displacements at the magnitude extremes (i.e., **M** 5.0 and 8.5) relative to the existing models that use linear scaling. The FDMs that use non-normal distributions generally have broader lower tails and narrower upper tails compared to those that use normal distributions, which has a first order impact on hazard analysis. These generalizations provide an idea of how models compare, but the trade-off between the different model elements may be more nuanced for a given scenario (i.e., style, magnitude, and rupture position).

Model results are presented in several ways in this report to provide a comprehensive comparison between the FDMs. For example, median profile shapes and magnitude scaling with average and maximum displacement are shown in Chapter 4. Aleatory variability is compared with cumulative displacement distribution curves (paired with fractile plots) in Chapter 5.1 and in hazard space in the form of probability of exceedance curves in Chapter 5.2. Additionally, plots of the logarithmic ratios of 84^{th}-to-median and median-to-16^{th} percentiles are provided in Appendix B. Direct comparisons between the models are not straightforward for two reasons. First, some models use different displacement metrics (Chapter 2.1). While this impact is generally small, comparisons between some models is technically inexact or not commensurable. Second, the models use different statistical distributions to characterize the aleatory variability. As a result, comparing statistical parameters (e.g., standard deviation) between models is not meaningful. Instead, the aleatory variability is best compared between models on a scenario basis with probability distributions or fractiles.

The median predictions for all new models are within a factor of three or better for $\mathbf{M} \geq 6.0$ for all styles of faulting and all normalized rupture positions. (Chapter 5.1). The largest differences are at the rupture endpoints ($x/L = 0$) due to different profile shapes (particularly the end-of-rupture tapering) used in the models and data set limitations at the ends of ruptures. The smallest differences correspond with magnitudes that are best represented in the FDHI Database. For example, median predictions in the new models are most similar around **M** 7.0 for strike-slip and normal events (within factors of 1.5 and 1.2, respectively) and $\mathbf{M} \leq 6.5$ for reverse events (within a factor of 1.5).

Comparisons to existing models vary based on style of faulting. For strike-slip events, median predictions in the new models are generally higher than PEA11 for **M** 6.7 to 7.8 for all rupture positions due to the piecewise (bi-linear or tri-linear) magnitude scaling in the new models (Figure 4.2a). For normal events, median predictions in the new models are lower than YEA03 for most magnitudes and rupture positions, and the magnitude scaling used in the KEA22 model produces median displacement that are significantly lower than YEA03 at the magnitude extremes (i.e., **M** 6.0 and 8.0). The new reverse models produce median displacements that are similar to the MR11 model for all magnitudes and rupture positions.

Improved aleatory variability modeling in the new FDMs captures the upper and lower tails of the data distributions better than previously published models. The 95th percentile predictions between all new models are within a factor of about 2.5 or better for **M** $\geq$ 6.0 for all styles of faulting and all normalized rupture positions. The displacements are within a factor two for all magnitudes in reverse events and within a factor of 1.2 for **M** $\geq$ 6.5 in normal events.

Compared to existing models, all new FDMs produce lower 95th percentile predictions at the rupture midpoint ($x/L = 0.5$) for **M** $\geq$ 7.2 and all styles of faulting. For example, the 95th percentile displacements in the new models for a **M** 8.0 strike-slip earthquake range from 12 to 19 meters, whereas the PEA11 prediction is 40 meters. Similarly, 95th percentile displacements for reverse faulting range from 7 to 12 meters in a **M** 8.0 earthquake, while the MR11 prediction is 17 meters. For normal events, the new FDMs predict 95th percentile displacements between 9 and 12 meters at the rupture midpoint of a **M** 8.0 event, and the YEA03 prediction is 38 meters.

Within-model epistemic uncertainty in the new FDMs is evaluated with probability of exceedance curves in Chapter 6. Each model handles epistemic uncertainty differently. The impact of including epistemic uncertainty in each model depends on the hazard level of interest and scenario (i.e., style, magnitude, and rupture position). The within-model epistemic uncertainty should be assessed on a case-by-case basis, depending on the specific application. Most model developers recommend including within-model epistemic.

The four new fault displacement amplitude prediction models summarized in this report represent the state-of-the-art in fault displacement model development, and we anticipate widespread implementation of these models by hazard analysts. The comparisons in this report span a range of scenarios defined by style of faulting, magnitude, rupture position, and percentile. While the range is sufficiently broad to provide end-users with an understanding of the performance of each model, it is not exhaustive, and we recommend hazard analysts evaluate the impact of the new models in their specific application.

REFERENCES

Abrahamson, N., Atkinson, G., Boore, D., Bozorgnia, Y., Campbell, K., Chiou, B., Idriss, I., Silva, W., and Youngs, R. (2008). "Comparisons of the NGA ground-motion relations." *Earthquake Spectra*, 24(1), 45–66.

Atik, L. A. and Youngs, R. R. (2014). "Epistemic uncertainty for NGA-West2 models." *Earthquake Spectra*, 30(3), 1301–1318.

Chiou, B. S.-J., Chen, R., Thomas, K., Milliner, C. W. D., Dawson, T., and Petersen, M. D. (2022). "Surface Fault Displacement Models for Strike-Slip Faults." *Report in preparation for The B. John Garrick Institute for the Risk Sciences at UCLA Engineering*.

Coppersmith, K. and Youngs, R. (2000). "Data needs for probabilistic fault displacement hazard analysis." *Journal of Geodynamics*, 29(3-5), 329–343.

Gregor, N., Abrahamson, N. A., Atkinson, G. M., Boore, D. M., Bozorgnia, Y., Campbell, K.W., Chiou, B. S.-J., Idriss, I., Kamai, R., Seyhan, E., et al. (2014). "Comparison of NGA-West2 GMPEs." *Earthquake Spectra*, 30(3), 1179–1197.

Gregor, N., Addo, K., Abrahamson, N. A., Al Atik, L., Atkinson, G. M., Boore, D. M., Bozorgnia, Y., Campbell, K.W., Chiou, B. S., G¨ulerce, Z., et al. (2022). "Comparisons of the NGA-subduction ground motion models." *Earthquake Spectra*, 38(4), 2580–2610.

Hemphill-Haley, M. A. and Weldon, R. J. (1999). "Estimating prehistoric earthquake magnitude from point measurements of surface rupture." *Bulletin of the Seismological Society of America*, 89(5), 1264–1279.

Keefer, D. L. and Bodily, S. E. (1983). "Three-point approximations for continuous random variables." *Management Science*, 29(5), 595–609.

Kuehn, N., Kottke, A., Madugo, C., Sarmiento, A., and Bozorgnia, Y. (2022). "UCLA-PG&E Fault Displacement Model." Report No. GIRS-2022-06, *The B. John Garrick Institute for the Risk Sciences at UCLA Engineering*, <https://www.risksciences.ucla.edu/girs-reports/2022/06>.

Lavrentiadis, G. and Abrahamson, N. (2022). "Fault Surface-Rupture Model for Probabilistic Hazard Analysis." *Manuscript submitted to Earthquake Spectra*.

Lavrentiadis, G. and Abrahamson, N. (2019). "Generation of surface-slip profiles in the wavenumber domain." *Bulletin of the Seismological Society of America*, 109(3), 888-907.

Lavrentiadis, G. et al. (2022a). "An Event-Specific Coordinate System Developed for Fault Rupture and Displacement Data." *Report in preparation for The B. John Garrick Institute for the Risk Sciences at UCLA Engineering*.

Lavrentiadis, G., Wang, Y., Abrahamson, N. A., Bozorgnia, Y., and Goulet, C. (2022b). "A Seismologically Consistent Surface Rupture Length Model for Unbounded and Width-Limited Events." Report No. GIRS-2022-09, *The B. John Garrick Institute for the Risk Sciences at UCLA Engineering*, <https://www.risksciences.ucla.edu/girs-reports/2022/09>.

Litchfield, N. J., Van Dissen, R. J., Hornblow, S., Quigley, M., and Archibald, G. C. (2014). "Detailed analysis of Greendale Fault ground surface rupture displacements and geometries." *GNS Science*.

Manighetti, I., Perrin, C., Gaudemer, Y., Dominguez, S., Stewart, N., Malavieille, J., and Garambois, S. (2020). "Repeated giant earthquakes on the Wairarapa fault, New Zealand, revealed by Lidar-based paleoseismology." *Scientific Reports*, 10(1), 2124.

Manighetti, I., Campillo, M., Sammis, C., Mai, P. M., and King, G. (2005). "Evidence for self-similar, triangular slip distributions on earthquakes: Implications for earthquake and fault mechanics." *Journal of Geophysical Research: Solid Earth*, 110(B5).

McCalpin, J. P. and Slemmons, D. B. (1998). "Statistics of Paleoseismic Data: Final Technical Report Submitted to US Geological Survey." Report No. USGS-NEHRP Contract 1434-HQ-96-GR-02752, GEO-HAZ Consulting, Inc.

Moss, R., Thompson, S., Kuo, C.-H., Younesi, K., and Chao, S.-H. (2022). "Reverse Fault PFDHA." Report No. GIRS-2022-05, *The B. John Garrick Institute for the Risk Sciences at UCLA Engineering*, <https://www.risksciences.ucla.edu/girs-reports/2022/05>.

Moss, R. E. S. and Ross, Z. E. (2011). "Probabilistic Fault Displacement Hazard Analysis for Reverse Faults." *Bulletin of the Seismological Society of America*, 101(4), 1542–1553.

Petersen, M. D., Dawson, T. E., Chen, R., Cao, T., Wills, C. J., Schwartz, D. P., and Frankel, A. D. (2011). "Fault displacement hazard for strike-slip faults." *Bulletin of the Seismological Society of America*, 101(2), 805– 825.

Rodgers, D. and Little, T. (2006). "World's largest coseismic strike-slip offset: The 1855 rupture of the Wairarapa Fault, New Zealand, and implications for displacement/length scaling of continental earthquakes." *Journal of Geophysical Research*: Solid Earth, 111(B12).

Sarmiento, A., Madugo, D., Bozorgnia, Y., Shen, A., Mazzoni, S., Lavrentiadis, G., Dawson, T., Madugo, C., Kottke, A., Thompson, S., Baize, S., Milliner, C., Nurminen, F., Boncio, P., and Visini, F. (2021). "Fault Displacement Hazard Initiative Database." Report No. GIRS-

2021-08, Revision 3 dated 19 July 2022, *The B. John Garrick Institute for the Risk Sciences at UCLA Engineering*, <https://www.risksciences.ucla.edu/girs-reports/2021/08>.

Spudich, P. and Chiou, B. (2015). "Strike-Parallel and Strike-Normal Coordinate System Around Geometrically Complicated Rupture Traces – Use by NGA-West2 and Further Improvements." Report No. OFR 2015-1028, US Department of the Interior, *US Geological Survey*.

Stepp, J. C., Wong, I., Whitney, J., Quittmeyer, R., Abrahamson, N., Toro, G., Youngs, R., Coppersmith, K., Savy, J., Sullivan, T., and Yucca Mountain PSHA Project Members (2001). "Probabilistic seismic hazard analyses for ground motions and fault displacement at Yucca Mountain, Nevada." *Earthquake Spectra*, 17(1), 113–151.

Thomas, K., Milliner, C. W., Chen, R., Chiou, B. S.-J., Dawson, T., and Petersen, M. D. (2022). "Least Cost Path Analysis as an Objective and Automated Method to Define the Primary Fault Trace for Probabilistic Fault Displacement Hazard Analysis." *Manuscript submitted to Earthquake Spectra*.

Valentini, A., Fukushima, Y., Contri, P., Ono, M., Sakai, T., Thompson, S. C., Viallet, E., Annaka, T., Chen, R., Moss, R. E., et al. (2021). "Probabilistic fault displacement hazard assessment (PFDHA) for nuclear installations according to IAEA safety standards." *Bulletin of the Seismological Society of America*, 111(5), 2661–2672.

Wells, D. L. and Coppersmith, K. J. (1994). "New empirical relationships among magnitude, rupture length, rupture width, rupture area, and surface displacements." *Bulletin of the Seismological Society of America*, 84(4), 974–1002.

Wells, D. L. and Coppersmith, K. J. (1993). "Likelihood of surface rupture as a function of magnitude." *Seismological Research Letters*, 64(1), 54.

Wesnousky, S. G. (2008). "Displacement and geometrical characteristics of earthquake surface ruptures: Issues and implications for seismic-hazard analysis and the process of earthquake rupture." *Bulletin of the Seismological Society of America*, 98(4), 1609–1632.

Youngs, R. R., Arabasz, W. J., Anderson, R. E., Ramelli, A. R., Ake, J. P., Slemmons, D. B., McCalpin, J. P., Doser, D. I., Fridrich, C. J., Swan, F. H., Rogers, A. M., Yount, J. C., Anderson, L. W., Smith, K. D., Bruhn, R. L., Knuepfer, P. L. K., Smith, R. B., DePolo, C. M., O'Leary, D. W., Coppersmith, K. J., Pezzopane, S. K., Schwartz, D. P., Whitney, J. W., Olig, S. S., and Toro, G. R. (2003). "A Methodology for Probabilistic Fault Displacement Hazard Analysis (PFDHA)." *Earthquake Spectra*, 19(1), 191–219.

Appendix A:

Preliminary Comparisons of Results from Different Displacement Aggregation Approaches

1 Introduction

This Appendix documents the results of an FDHI Working Group tasked with understanding the impact of different displacement aggregation methodologies. Three of the four new FDHI models (KEA22, CEA22, and LA22) predict an aggregated displacement that represents displacements summed across multiple (sub)parallel ruptures. This was considered to be a more stable metric by some developers to better account for displacement on complex surface rupture patterns that are not captured in the modeling. All three models use an aggregation approach that accounts for irregular spacing of displacement measurement sites. Each team (KEA22, CEA22, and LA22) used their own method to aggregate the displacements based on data in the FDHI Database.

A Working Group convened in early 2021 to review different aggregation approaches by evaluating data from six earthquakes:

- 1992 **M** 7.28 Landers, California (FDHI EQ_ID =1)
- 1999 **M** 7.13 Hector Mine, California (FDHI EQ_ID =2)
- 1987 **M** 6.54 Superstition Hills, California (FDHI EQ_ID =8)
- 2019 **M** 6.4 Ridgecrest-1, California (FDHI EQ_ID =42)
- 2019 **M** 7.1 Ridgecerest-2, California (FDHI EQ_ID =43)
- 1995 **M** 7.0 Neftegorsk, Russia (FDHI EQ_ID =65)

These events were selected to capture a range of surface rupture complexity (i.e., overlapping or parallel segments) and measurement site density and spacing. All are strike-slip earthquakes because the CEA22 model did not consider dip-slip events. Section 2 of this Appendix presents the plots and discussion for each event, and the Section 3 provides summarizes the results.

2 Evaluations

The results from the evaluations for each earthquake (Landers, Hector Mine, Superstition Hills, Ridgecrest-1, Ridgecrest-2, and Neftegorsk) are presented separately below. The KEA22 and LA22 models aggregate displacements from both principal and distributed measurements in the FDHI Database, whereas the CEA22 model only aggregates principal measurements. The KEA22 model applies a custom algorithm that computes an aggregated displacement value for each principal measurement in the database (referred to as "seed" measurement herein), using an hourglass-shaped search window and linearly interpolating displacements on the same rupture. The LA22 model computes the aggregate displacements on a segment basis. It uses geologic judgment to determine key rupture segments and applies the ECS algorithm to create a Segment Coordinate System (SCS) for each key segment. The SCS ordinates are used to identify (sub)parallel ruptures, and the displacements on each (sub)parallel rupture are linearly interpolated at the location of interest and summed to compute the aggregate slip. The CEA22 aggregates displacements based on geologic judgment and limited linear interpolation between measurement sites.

Four figures were used to qualitatively compare aggregation results from different modeling teams for each event. The first figure shows the spatial distribution and amplitude of observations (measurement sites) from the FDHI Database. The observations are color-coded based on classification or rank (i.e., cumulative, principal, or distributed). Marginal density plots are shown for each model to visually compare the spatial distribution and amplitude of displacements between each model. In the second figure, aggregated values for the same "seed" measurement site are compared directly on pair plots with 1:1 identity lines. The third figure shows model-to-model differences between aggregated values (in natural log units) with surface rupture maps to better understand how differences relate to rupture patterns. The last figure presents seed-to-aggregated log ratios as a function of seed displacement understand how aggregated amplitude depends on seed amplitude.

Results from a new wide-aperture fault displacement model (i.e., discrete displacement and inelastic deformation) by Milliner et al. (2020 and in prep.)[1] were also available to the Working

[1] Milliner, C., Avouac, J.-P., Chen, R., Aati, S., Chiou, B., Donnellan, A., Dawson, T., Madugo, C., and Dolan, J. F. (2020). "Development of a geodetic-based probabilistic fault displacement hazard analysis using near-field geodetic imaging data." *AGU Fall Meeting Abstracts*, Vol. 2020, T042–07.

Group for several of the events considered in this Appendix. For the purposes of this discussion, the wide-aperture results are omitted from the plots because the displacement metric is not equivalent to the aggregated value as the former also includes continuous deformation components such as warping.

2.1 LANDERS

The 1992 **M** 7.28 Landers, California event was selected because it is a complex and well-documented event in the FDHI Database. Additionally, preliminary results from a new dynamic rupture model validation study by Wang and Goulet (2021)[2] were available.

The results of the SCEC simulations (Wang and Goulet, 2021) are shown on Figure A.1. Their results are provided with uniform spacing along the rupture; accordingly, the results are not readily correlated with the FDHI Database measurement sites and are therefore omitted from the other plots.

The marginal density plot (Figure A.1) shows strong agreement in the spatial distribution of measurements along the rupture length, suggesting the different aggregation approaches do not significantly down-sample the number of measurements. (An exception is the SCEC model, which provides uniformly-sampled locations.) The displacement amplitude densities for the KEA, CEA, and SCEC models are in strong agreement. The LA results are generally similar but show more contribution from smaller values.

Generalized model comparisons can be made from the pair plots (Figure A.2) and are consistent with the trends in the displacement density plots. For example, the KEA and CEA aggregated values are generally higher than the LA values.

Visual inspection of the differences in aggregated values between models as a function of mapped ruptures (Figure A.3) reveals the largest differences are spatially associated with rupture complexity. The results are consistent with the pair plots; for example, aggregated values in the KEA model are systematically higher than the LA model. The CEA aggregated values are generally lower than the KEA and LA models where more distributed ruptures are mapped.

The seed-to-aggregated log ratios (Figure A.4) reveal some consistent trends. The ratios decrease as the seed (single-site measurement) increases. We infer this is due to a combination of spatial concentration of displacement for larger displacements (i.e., less complex rupture patterns) and the (numerically) relatively reduced effect of including smaller, distributed displacements. Additionally, the KEA ratios are systematically lower than the others, which we infer is due to inclusion of more distributed displacements and the use of an hourglass-shaped search window.

[2] Wang, Y., and Goulet, C. (2021). "Validation of fault displacements from dynamic rupture simulations against the observations from the 1992 Landers earthquake." *Bulletin of the Seismological Society of America*, 111(5), 2574-2594.

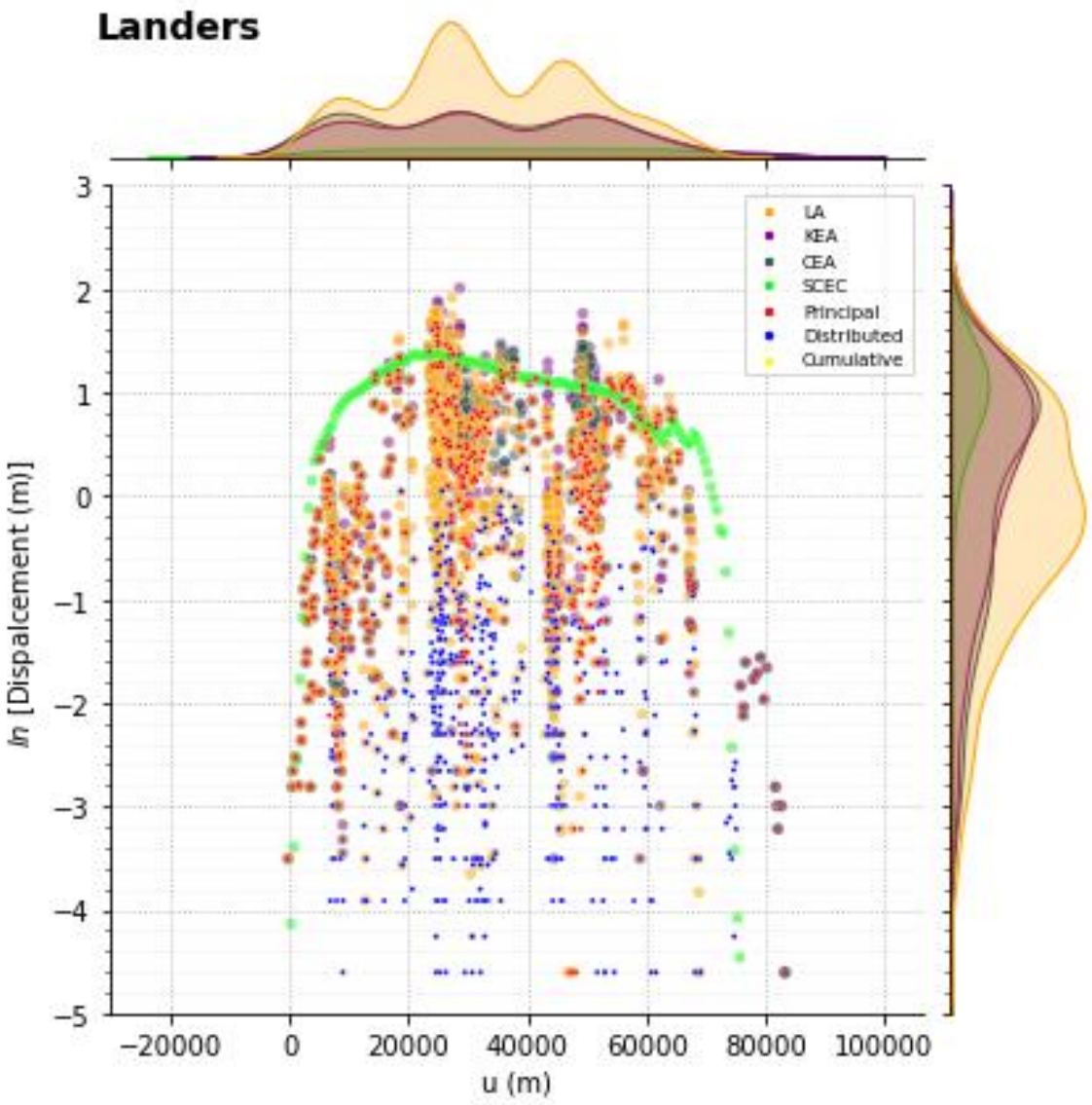

Figure A.1. Displacement measurements (Cumulative, Principal, and Distributed rank) from FDHI Database for 1992 **M** 7.28 Landers, California (FDHI EQ_ID =1) earthquake and aggregated displacements from KEA22, CEA22, and LA22 models. Marginal density plots shown for each model.

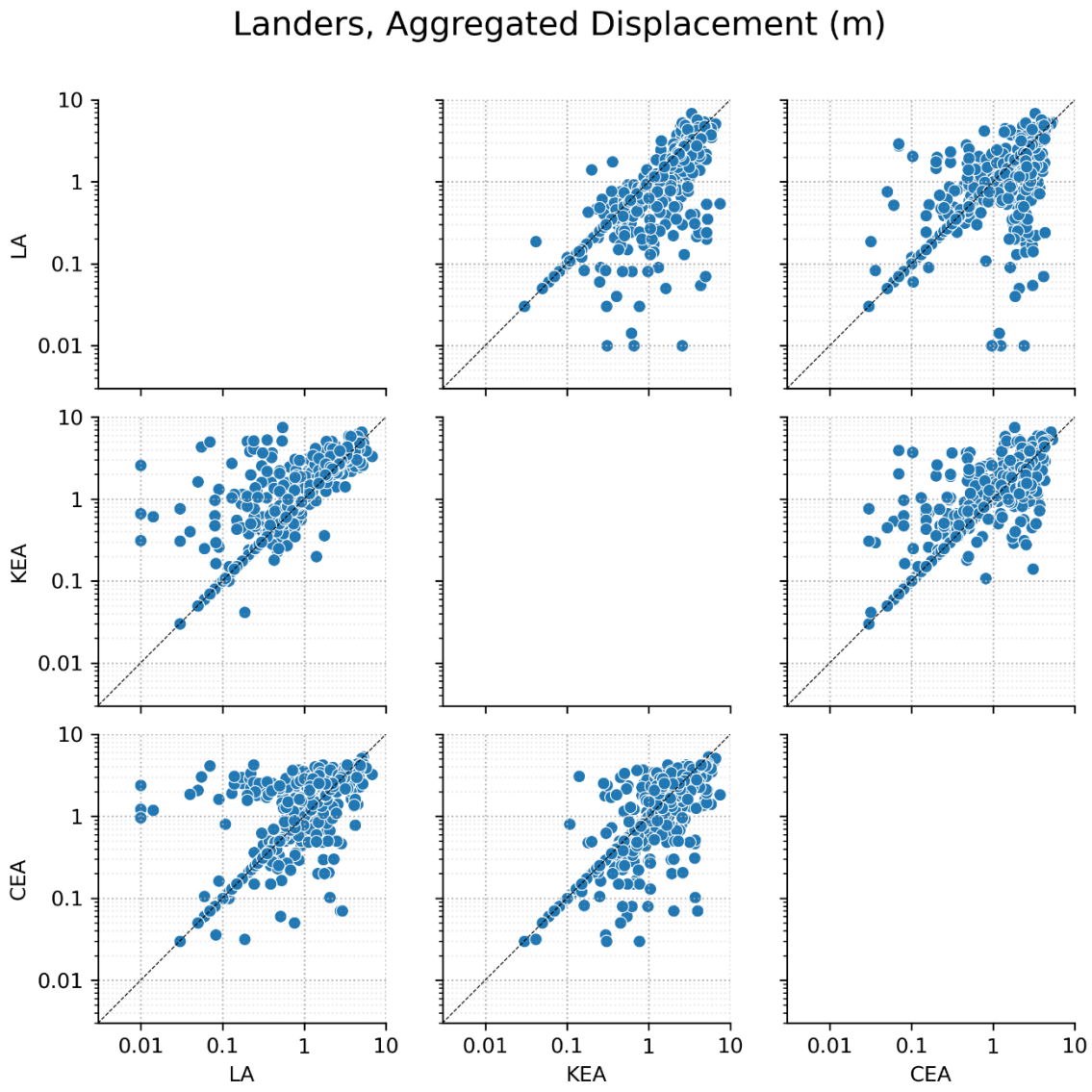

Figure A.2. Comparison of aggregated displacement results for each model (KEA22, CEA22, and LA22) based on measurement site for 1992 **M** 7.28 Landers, California earthquake.

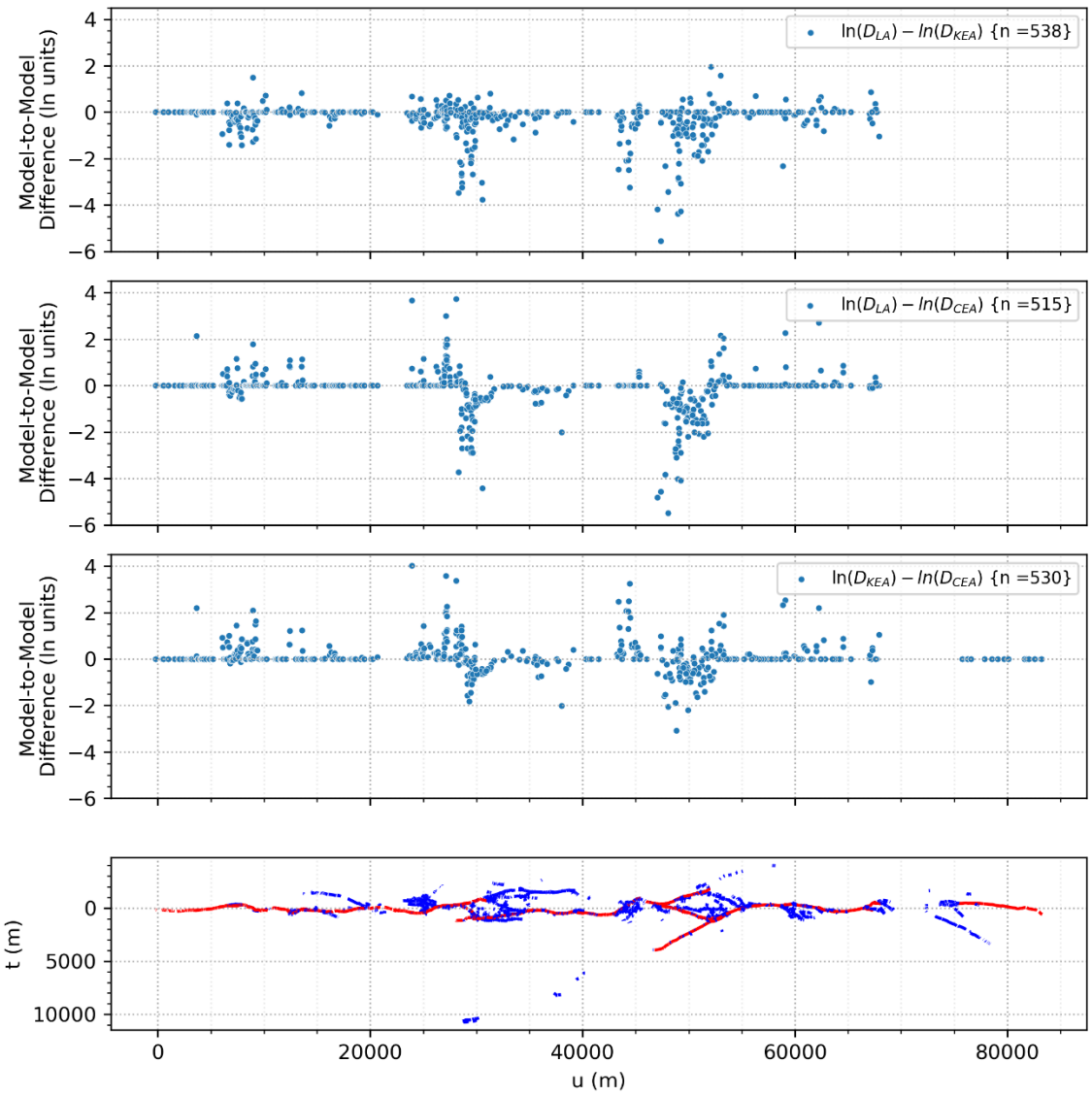

Figure A.3. Comparison of aggregated displacement results for each model (KEA22, CEA22, and LA22) as a function of rupture length for 1992 **M** 7.28 Landers, California earthquake. Principal (red) and distributed (blue) ruptures shown in projected (ECS) coordinated in bottom panel.

Figure A.4. Comparison of aggregated displacement results for each model (KEA22, CEA22, and LA22) as a function of seed (un-aggregated) measurement for 1992 **M** 7.28 Landers, California earthquake.

2.2 HECTOR MINE

The 1999 **M** 7.13 Hector Mine, California event was selected because it is a well-documented event with some rupture complexity. Additionally, Dr. Beth Arcos from Wood, PLC provided aggregation results for this event based on a manual geologic assessment performed for the California High Speed Rail (HSR) project.

The marginal density plot (Figure A.5) shows strong agreement in the spatial distribution of measurements along the rupture length for the KEA and LA models. The CEA and HSR models have more contribution from the southern end of the rupture (larger u-axis values) because both teams treated the Mesquite Lake Fault as a principal rupture. This is a technically-defensible alternative interpretation of the rankings in the FDHI Database. The displacement amplitude densities are in strong agreement for all models. The HSR results show a slightly higher contribution from smaller values is due to treating the Mesquite Lake Fault as a principal rupture. Over a dozen measurements are available on this fault and they are all relatively low, which affects the displacement amplitude density distribution.

Generalized model comparisons can be made from the pair plots (Figure A.6) and are consistent with the trends in the displacement density plots. For example, the KEA and CEA aggregated values are systematically higher than the LA values. The KEA results are also generally higher than the CEA results. The HSR results are generally higher than the CEA and LA results.

Visual inspection of the differences in aggregated values between models as a function of mapped ruptures (Figure A.7) reveals the largest differences are spatially associated with principal rupture complexity (particularly the bifurcation of the Bullion Fault near $u = 34{,}000$). Other key differences are at the southern end of the rupture ($u > 40{,}000$) where the CEA and HSR models treated the Mesquite Lake Fault as a principal rupture and therefore have more measurements in this area. The results are consistent with the pair plots; for example, aggregated values in the HSR model are systematically higher than the CEA and LA models, and the KEA results are higher than the CEA results.

The seed-to-aggregated log ratios (Figure A.8) reveal some consistent trends. The ratios decrease as the seed (single-site measurement) increases. Additionally, the KEA ratios are systematically lower than the others. Both of these trends were observed for the Landers evaluation and are discussed in more detail at the end of Section 2.1.

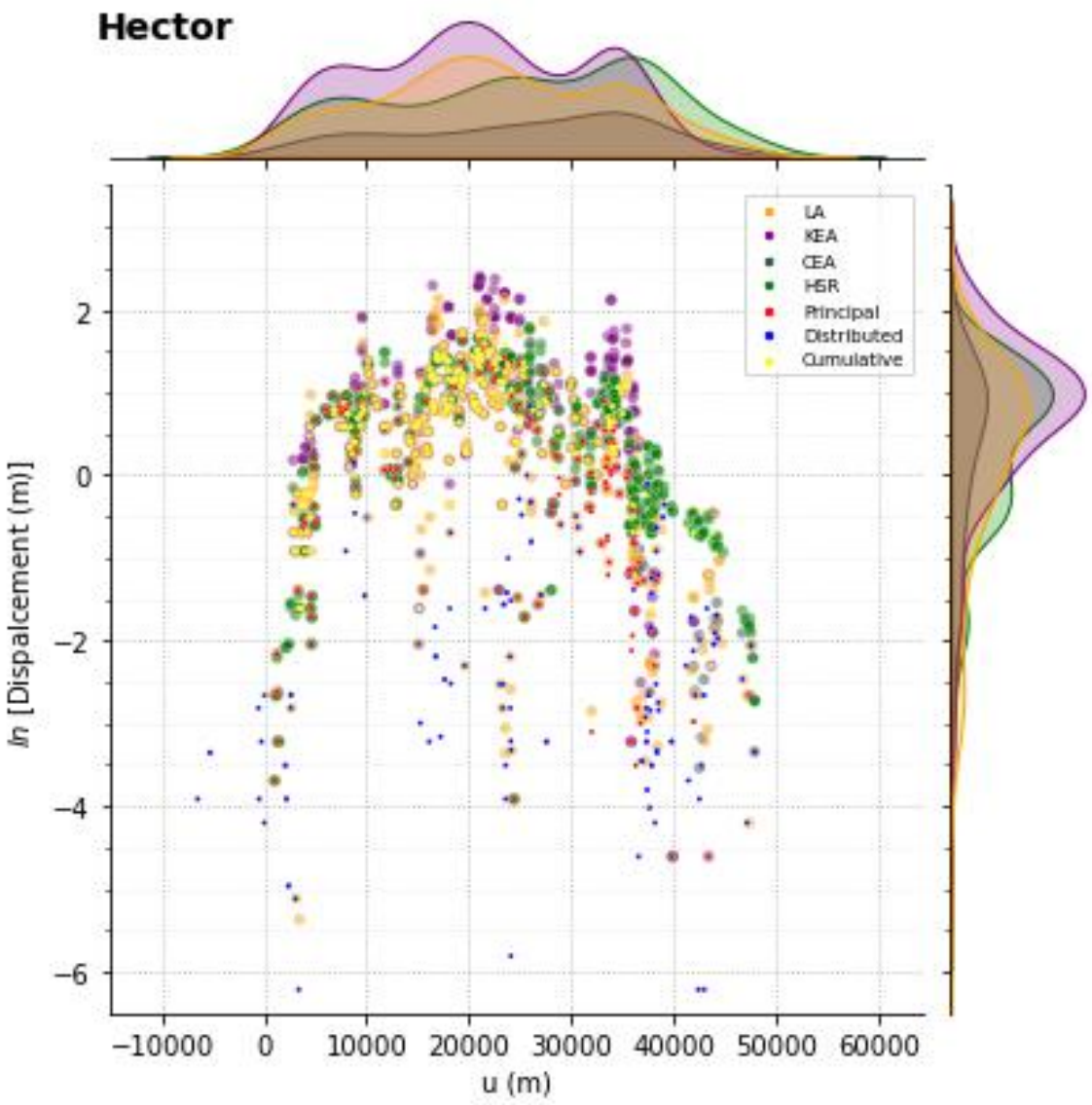

Figure A.5. Displacement measurements (Cumulative, Principal, and Distributed rank) from FDHI Database for 1999 **M** 7.13 Hector Mine, California (FDHI EQ_ID =2) earthquake and aggregated displacements from KEA22, CEA22, and LA22 models. Marginal density plots shown for each model.

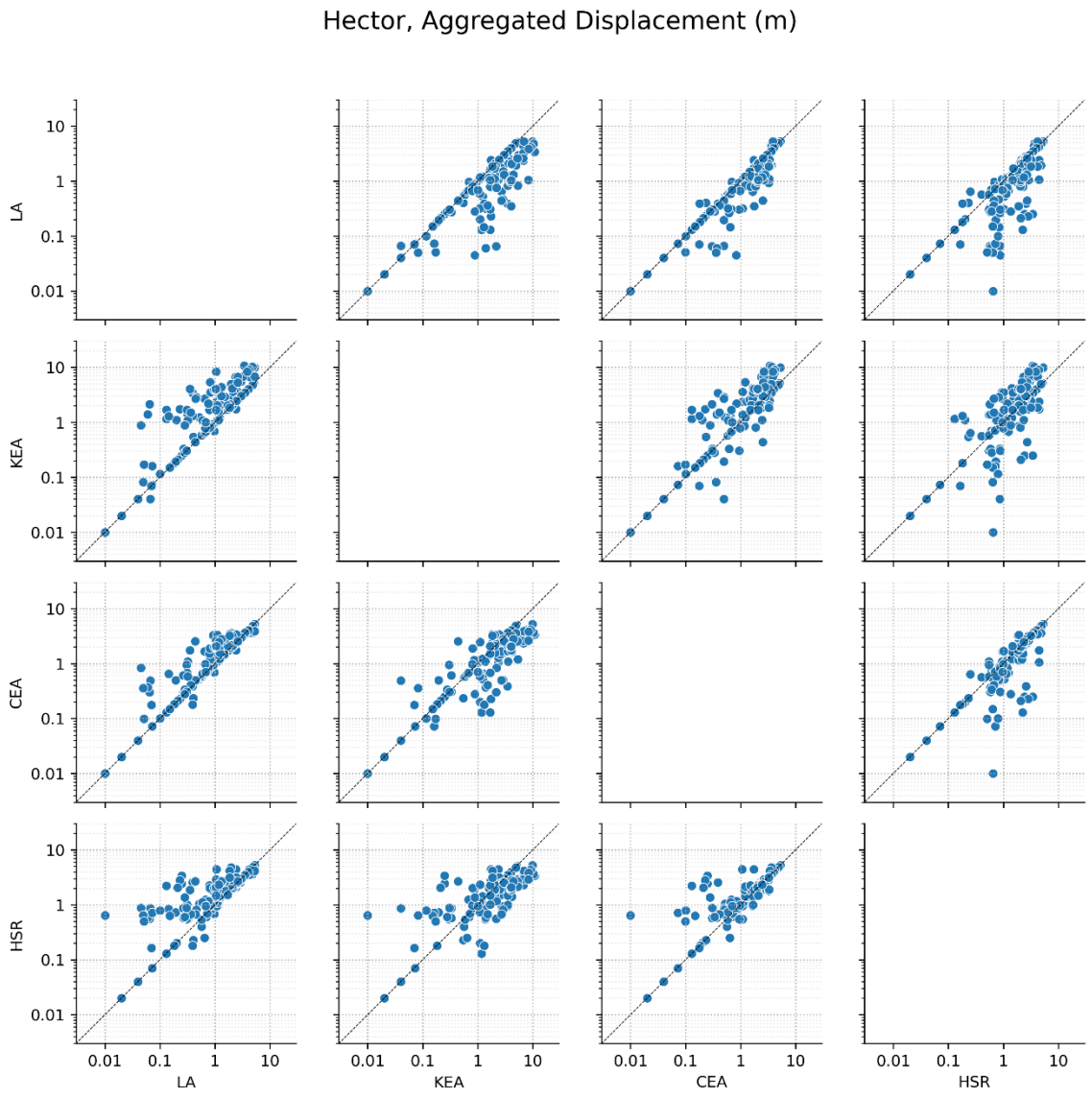

Figure A.6. Comparison of aggregated displacement results for each model (KEA22, CEA22, and LA22) based on measurement site for 1999 **M** 7.13 Hector Mine, California earthquake.

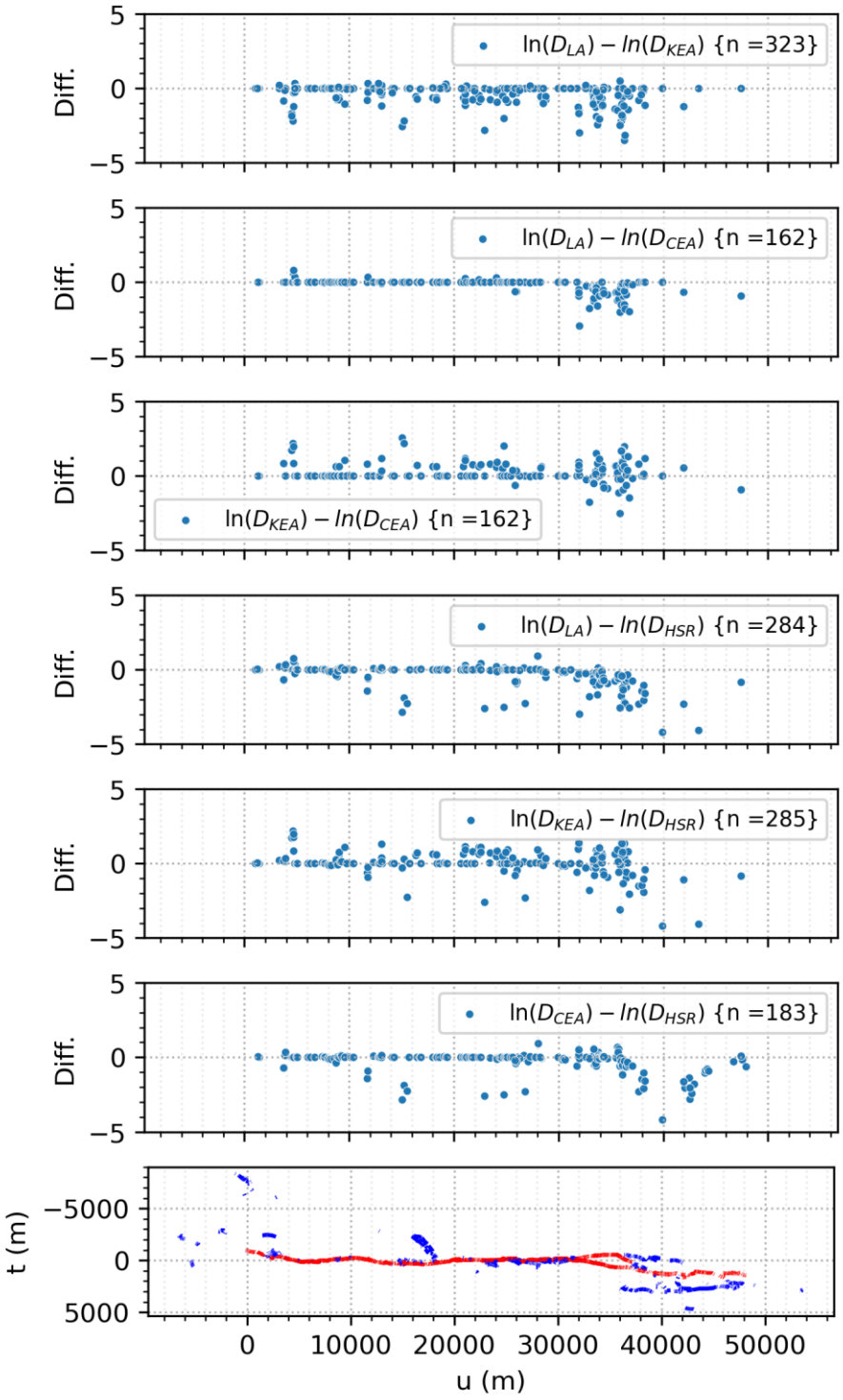

Figure A.7. Comparison of aggregated displacement results for each model (KEA22, CEA22, and LA22) as a function of rupture length for 1999 **M** 7.13 Hector Mine, California earthquake. Principal (red) and distributed (blue) ruptures shown in projected (ECS) coordinated in bottom panel.

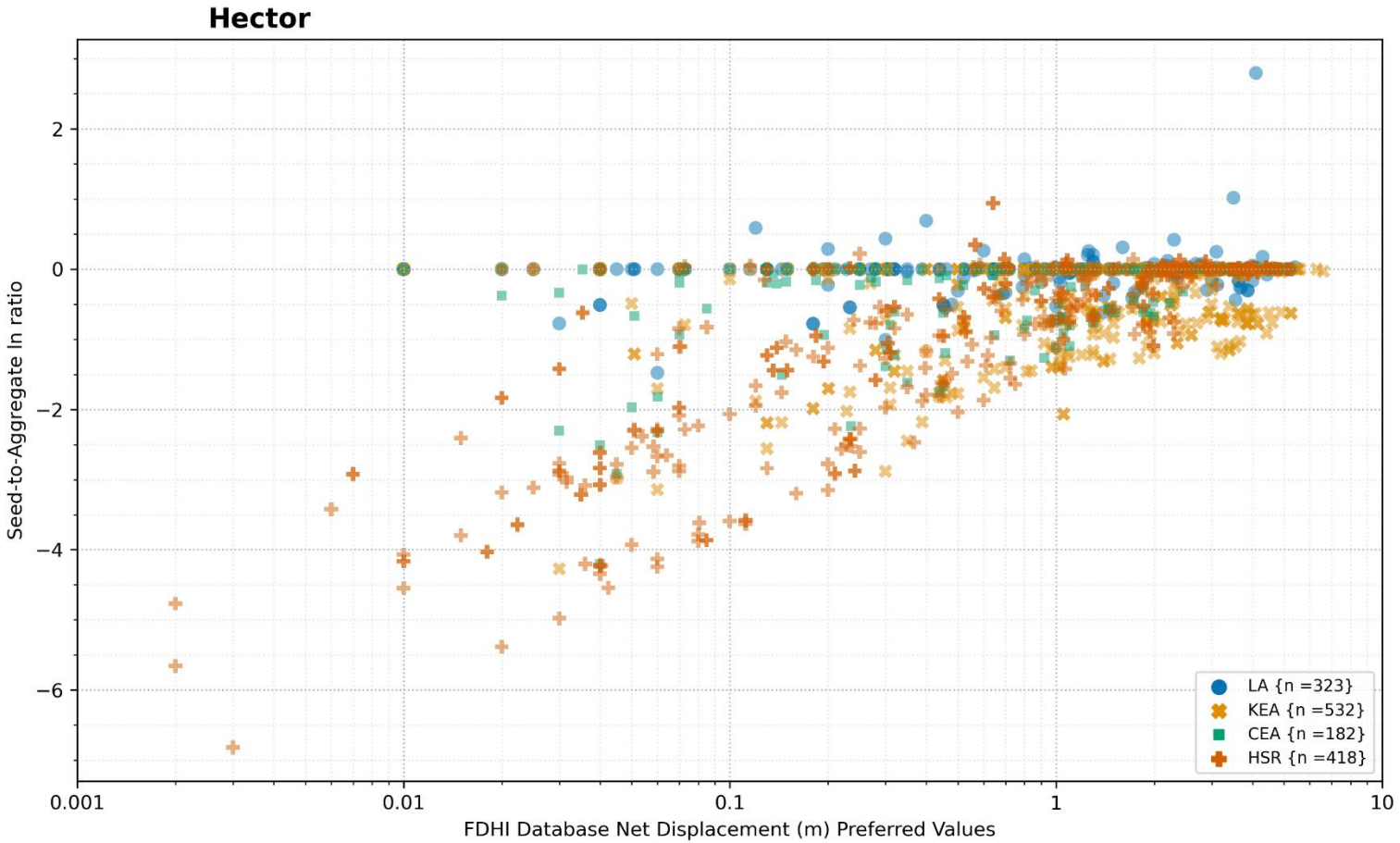

Figure A.8. Comparison of aggregated displacement results for each model (KEA22, CEA22, and LA22) as a function of seed (un-aggregated) measurement for 1999 **M** 7.13 Hector Mine, California earthquake.

2.3 SUPERSTITION HILLS

The 1987 **M** 6.54 Superstition Hills, California event was selected because it is a well-documented event with relatively simple but multi-stranded ruptures.

The marginal density plot (Figure A.9) shows strong agreement in the spatial distribution of measurements along the rupture length for the KEA and CEA models. The displacement amplitude densities are in strong agreement for all models.

Generalized model comparisons can be made from the pair plots (Figure A.10) and are consistent with the trends in the displacement density plots. For example, most of the values fall on the 1:1 equality line for each comparison. Where they differ, the CEA and LA results are generally higher than the KEA results.

Visual inspection of the differences in aggregated values between models as a function of mapped ruptures (Figure A.11) reveals that the largest differences are spatially associated with rupture complexity, particularly at the southern end of the rupture ($u > 21{,}000$), where the CEA results are higher than both KEA and LA.

The seed-to-aggregated log ratios (Figure A.12) reveal some consistent trends. The ratios decrease as the seed (single-site measurement) increases (as observed for other events; see discussion at the end of Section 2.1). The LA ratios are generally lower than the others.

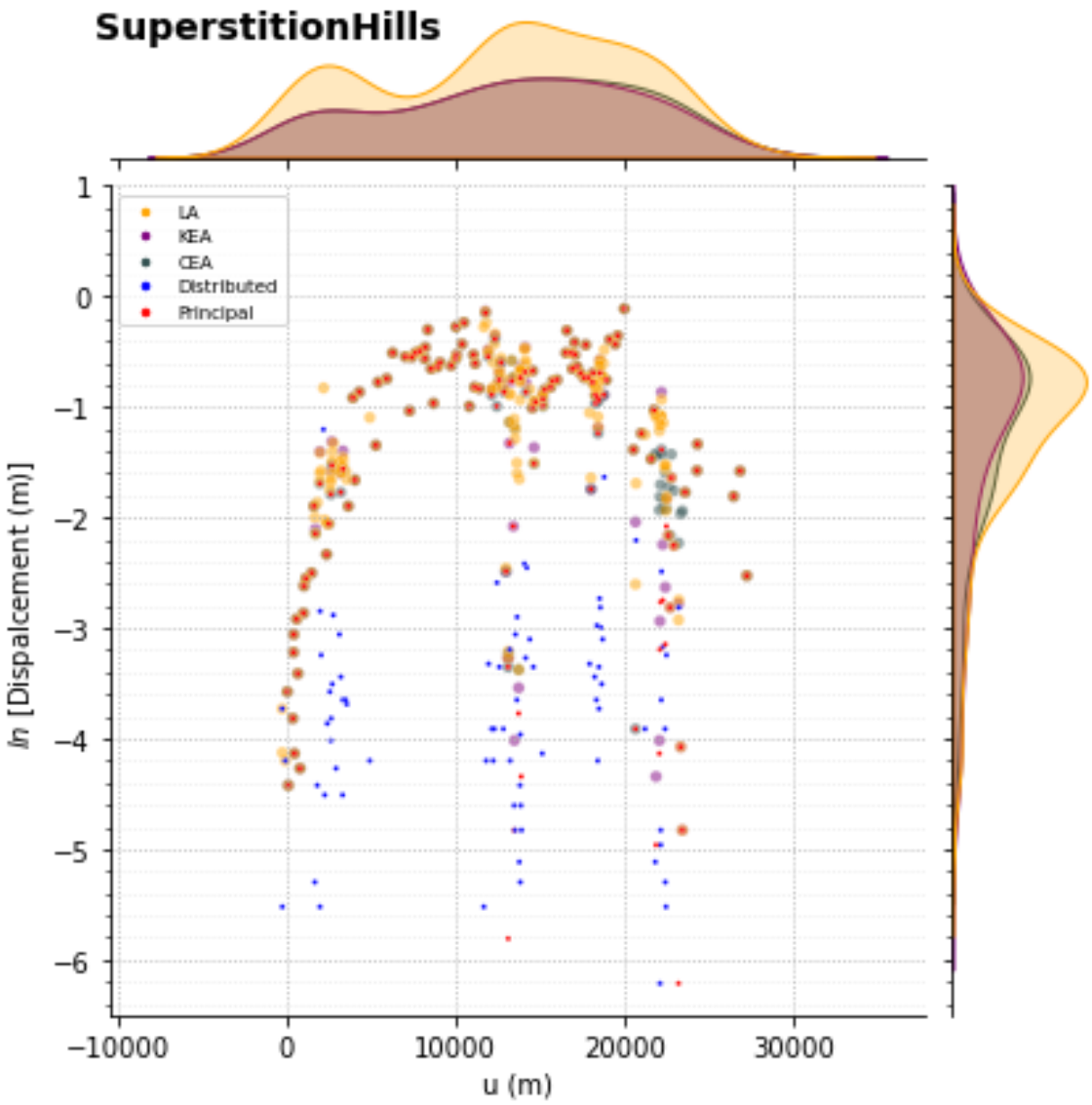

Figure A.9. Displacement measurements (Cumulative, Principal, and Distributed rank) from FDHI Database for 1987 **M** 6.54 Superstition Hills, California (FDHI EQ_ID =8) earthquake and aggregated displacements from KEA22, CEA22, and LA22 models. Marginal density plots shown for each model.

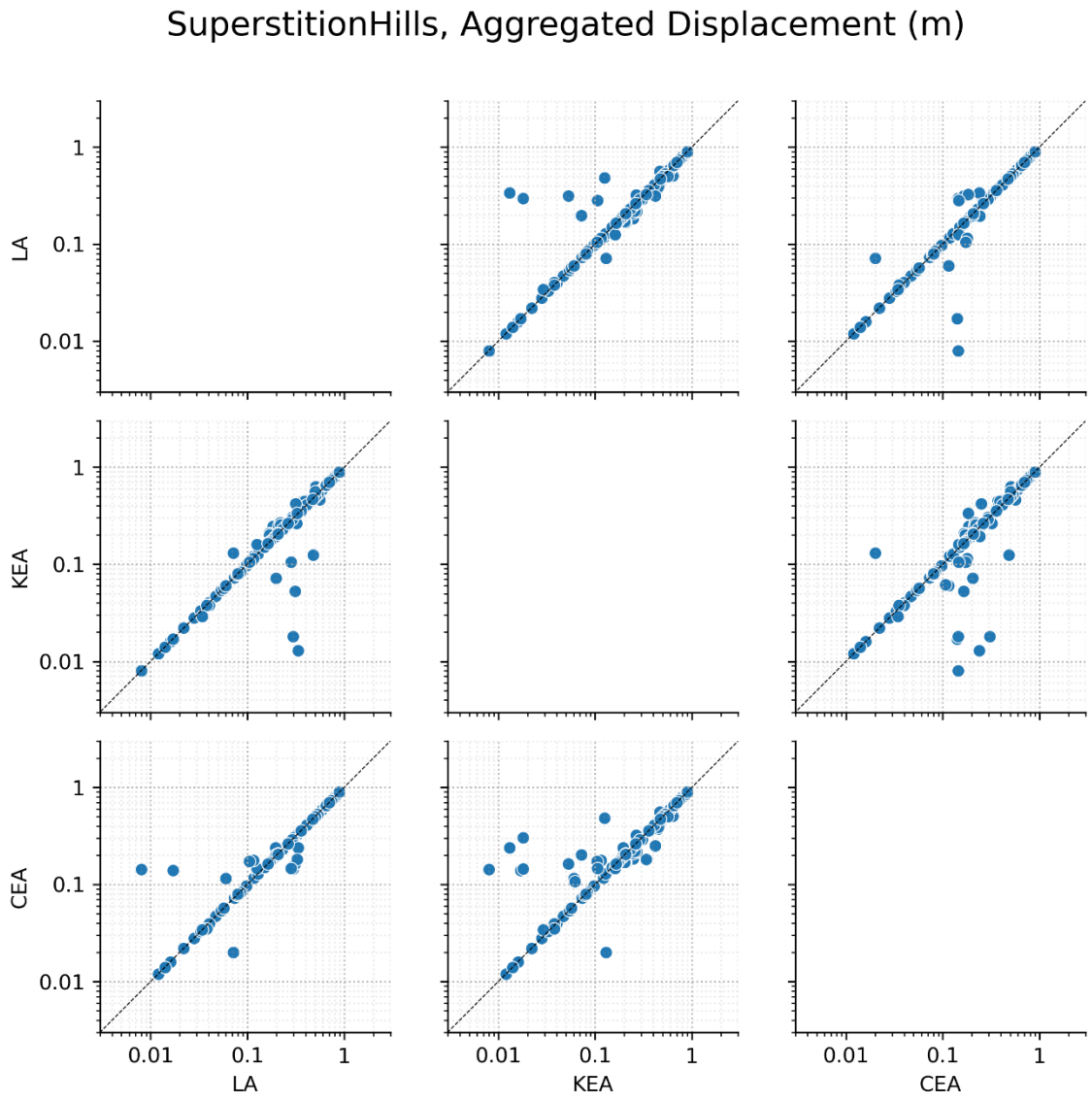

Figure A.10. Comparison of aggregated displacement results for each model (KEA22, CEA22, and LA22) based on measurement site for 1987 **M** 6.54 Superstition Hills, California earthquake.

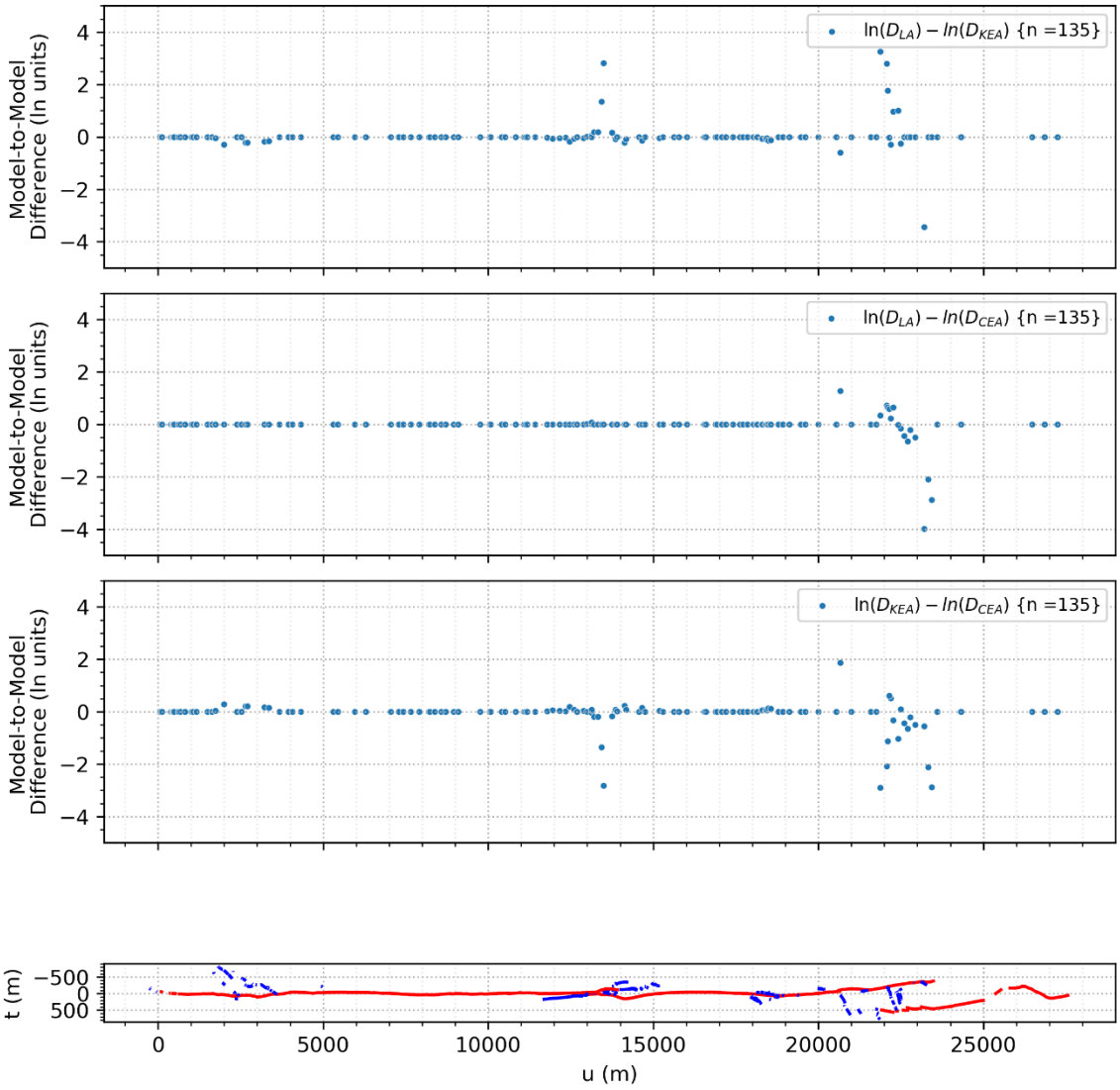

Figure A.11. Comparison of aggregated displacement results for each model (KEA22, CEA22, and LA22) as a function of rupture length for 1987 **M** 6.54 Superstition Hills, California earthquake. Principal (red) and distributed (blue) ruptures shown in projected (ECS) coordinated in bottom panel.

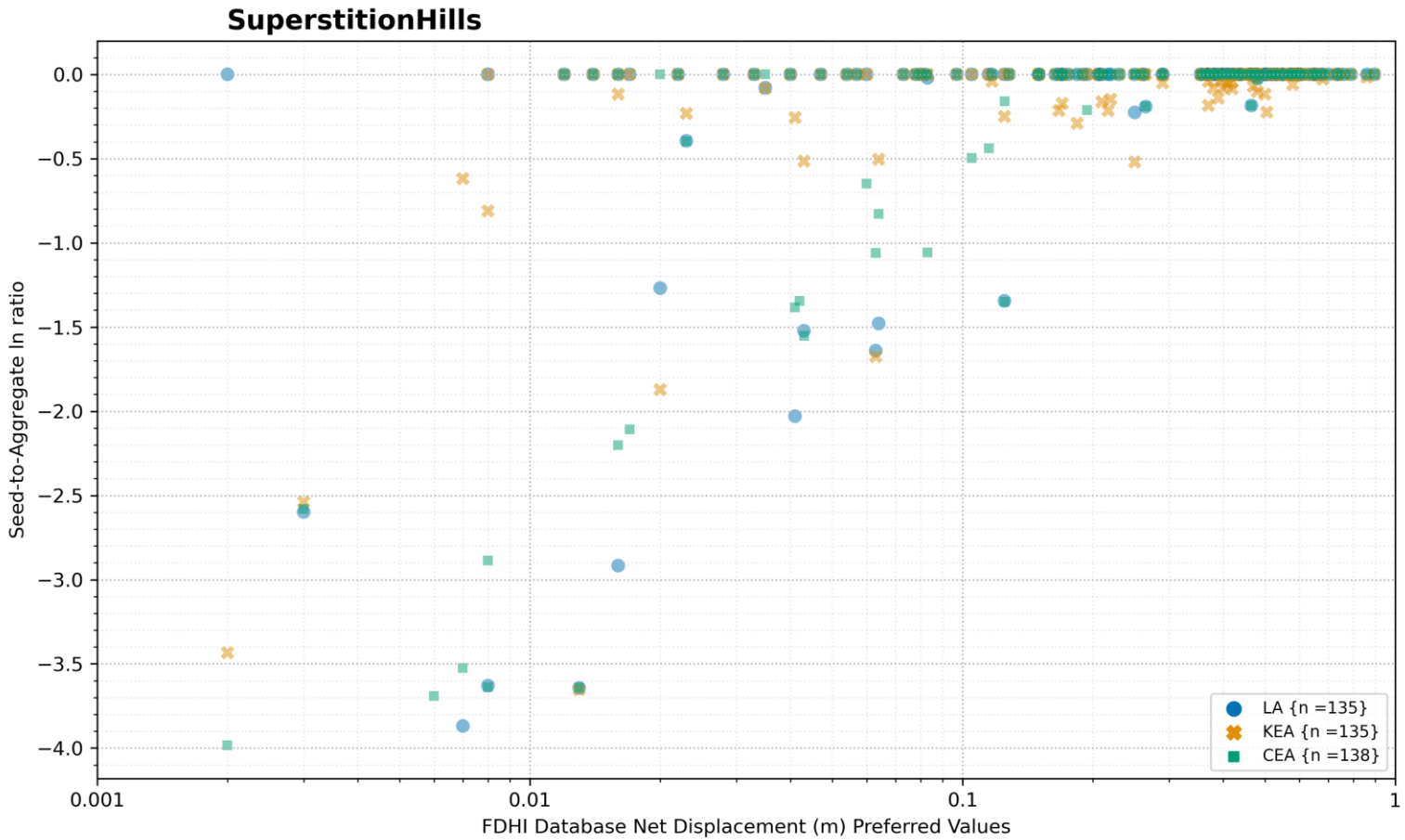

Figure A.12. Comparison of aggregated displacement results for each model (KEA22, CEA22, and LA22) as a function of seed (un-aggregated) measurement for 1987 **M** 6.54 Superstition Hills, California earthquake.

2.4 RIDGECREST-1

The 2019 **M** 6.4 Ridgecrest-1, California event was selected because it is a well-documented event.

The marginal density plot (Figure A.13) shows strong agreement in the spatial distribution of measurements along the rupture length for all models. The displacement amplitude densities are in strong agreement for the KEA and LA models. The CEA model shows more contribution from smaller values. This is a technically-defensible alternative interpretation of the rankings in the FDHI Database.

Generalized model comparisons can be made from the pair plots (Figure A.14) and are consistent with the trends in the displacement density plots. For example, the KEA and LA results are in very strong agreement.

Visual inspection of the differences in aggregated values between models as a function of mapped ruptures (Figure A.15) reveals the largest differences are spatially associated with the northeast reach of the rupture ($u < 2{,}500$), where the CEA model treated some of the ruptures as principal instead of distributed. We infer that their approach for linear interpolation between measurement sites is contributing to the differences because both the KEA and LA models include distributed measurements.

The seed-to-aggregated log ratios (Figure A.16) reveal some consistent trends. The ratios decrease as the seed (single-site measurement) increases (as observed for other events; see discussion at the end of Section 2.1). The KEA and CEA ratios are generally lower than the LA ratios.

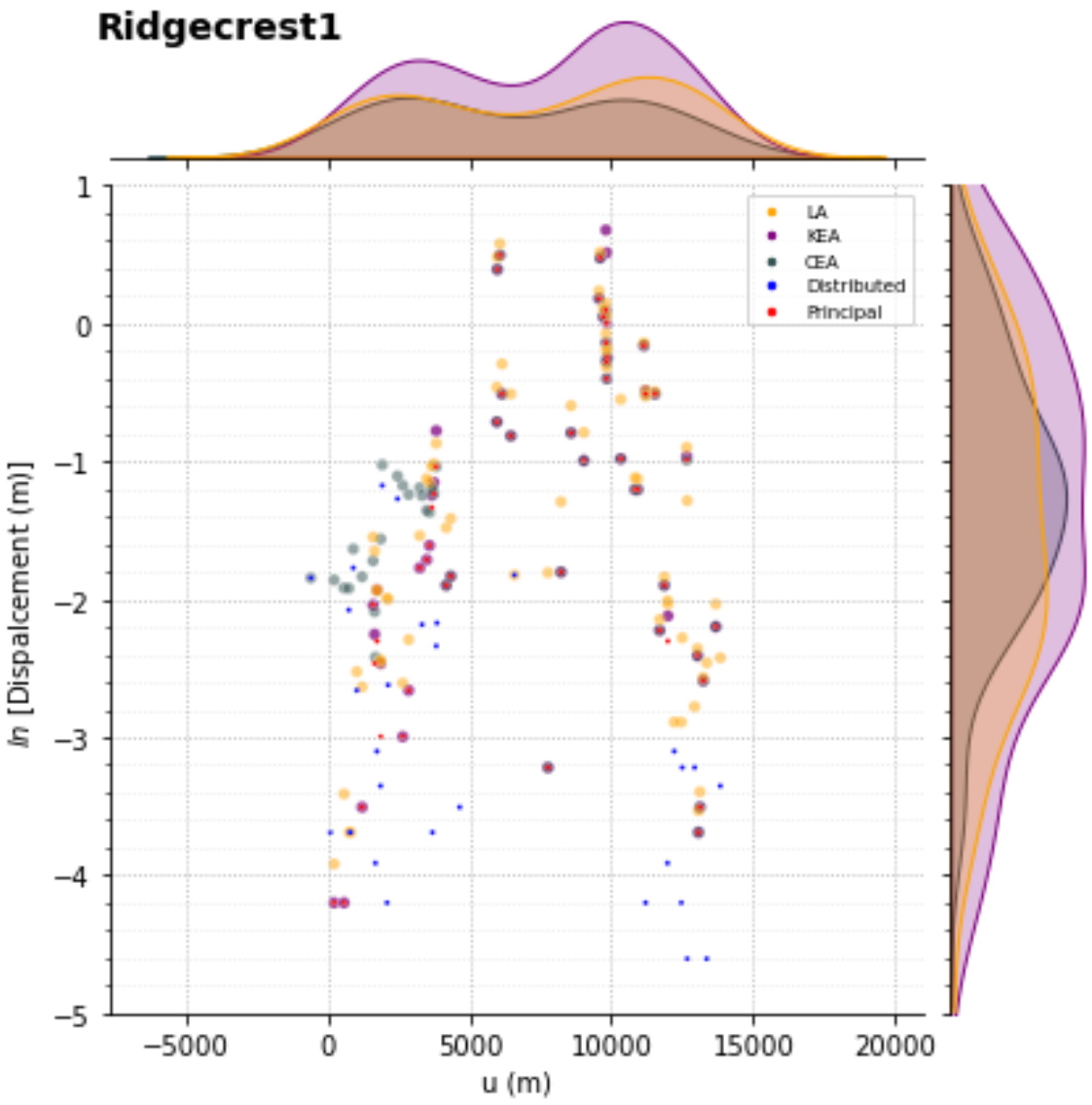

Figure A.13. Displacement measurements (Cumulative, Principal, and Distributed rank) from FDHI Database for 2019 **M** 6.4 Ridgecrest-1, California (FDHI EQ_ID =42) earthquake and aggregated displacements from KEA22, CEA22, and LA22 models. Marginal density plots shown for each model.

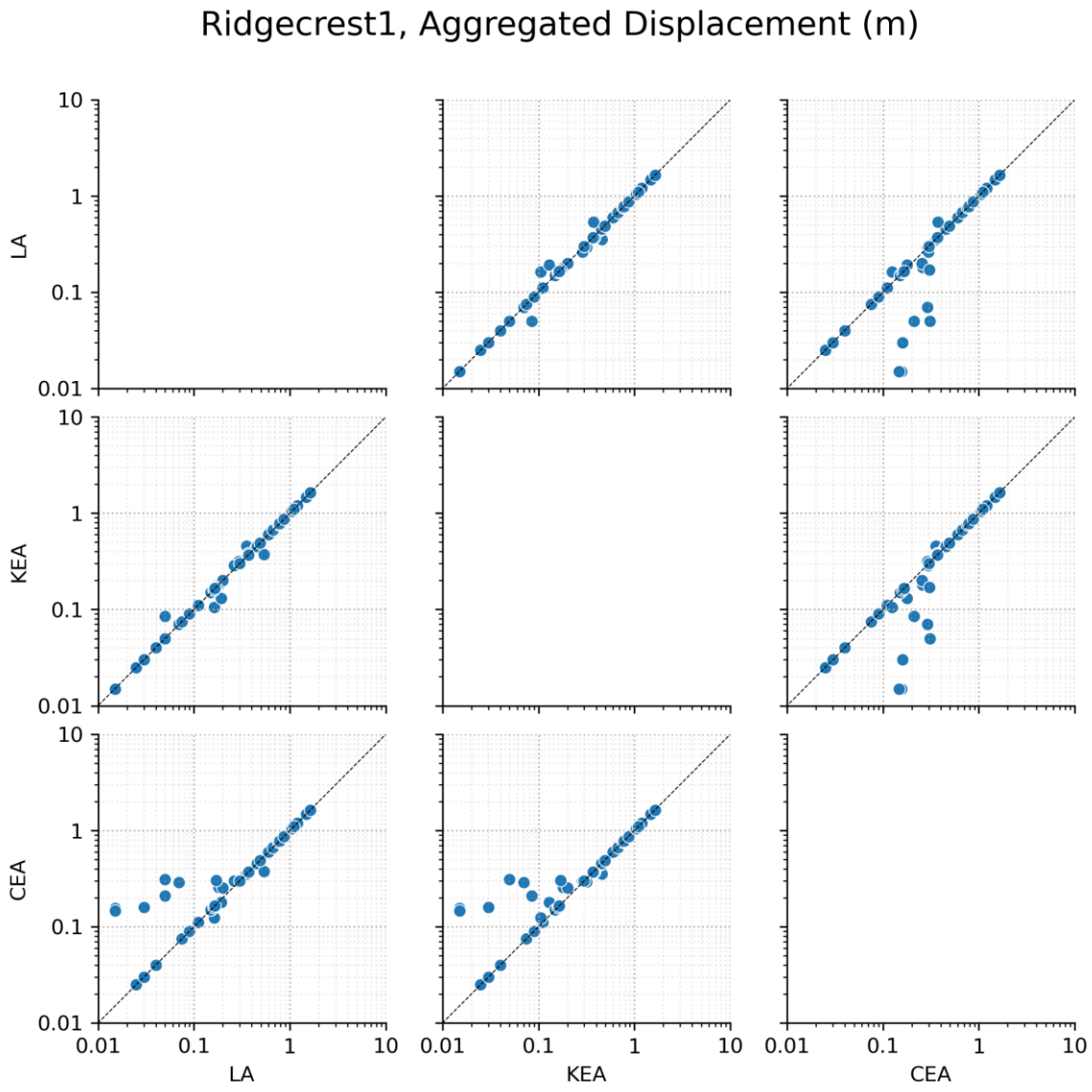

Figure A.14. Comparison of aggregated displacement results for each model (KEA22, CEA22, and LA22) based on measurement site for 2019 **M** 6.4 Ridgecrest-1, California earthquake.

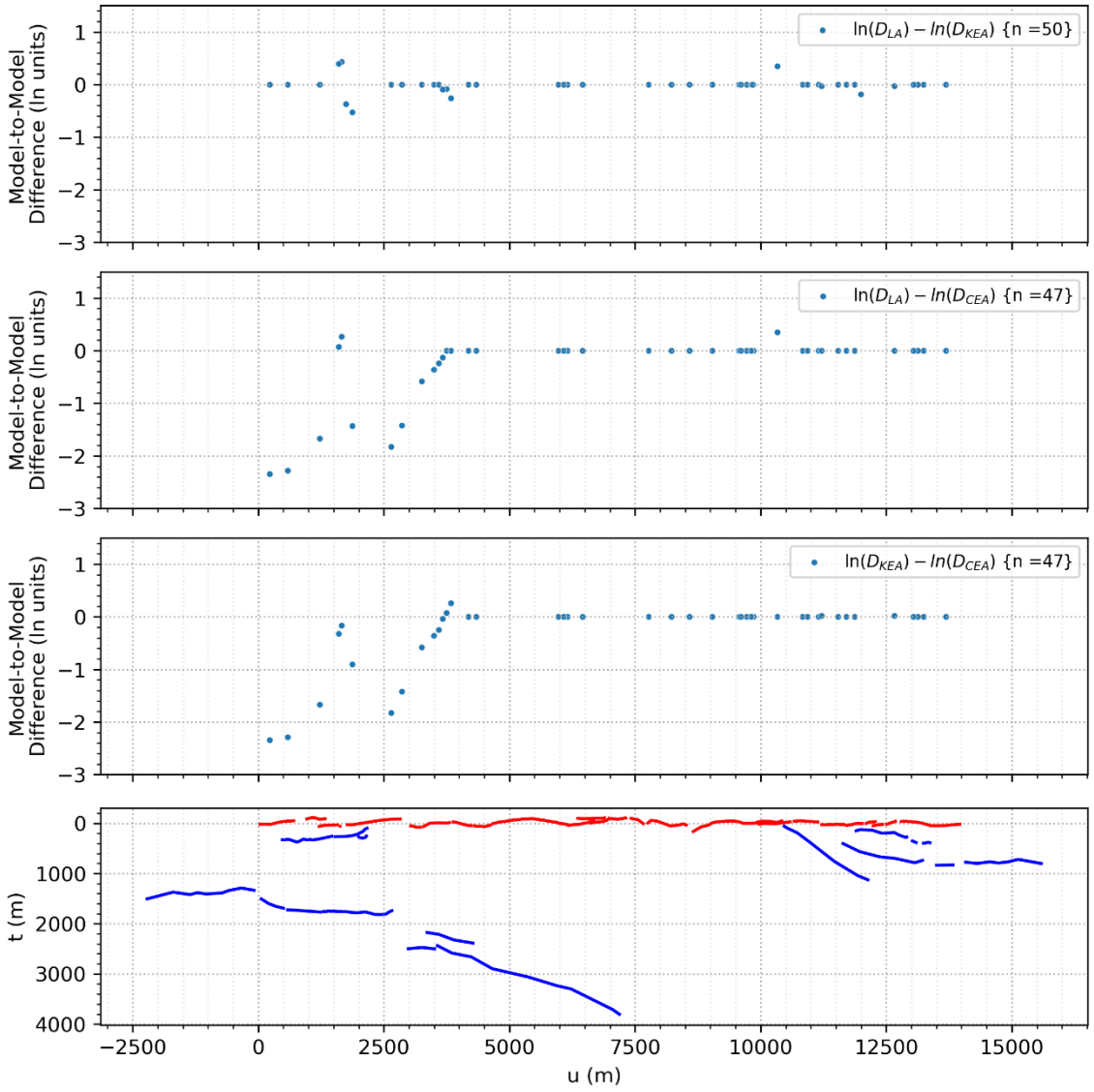

Figure A.15. Comparison of aggregated displacement results for each model (KEA22, CEA22, and LA22) as a function of rupture length for 2019 **M** 6.4 Ridgecrest-1, California earthquake. Principal (red) and distributed (blue) ruptures shown in projected (ECS) coordinated in bottom panel.

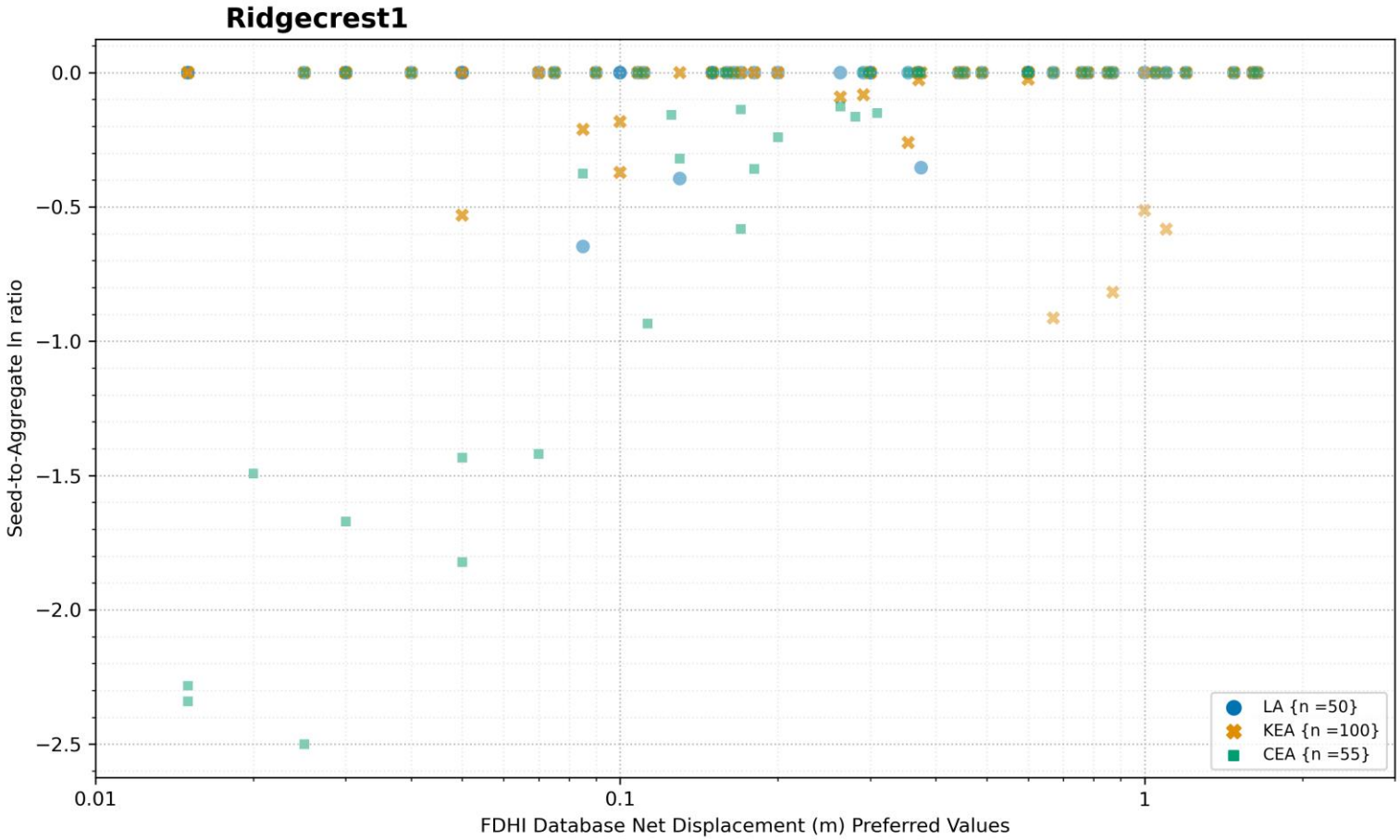

Figure A.16. Comparison of aggregated displacement results for each model (KEA22, CEA22, and LA22) as a function of seed (un-aggregated) measurement for 2019 **M** 6.4 Ridgecrest-1, California earthquake.

2.5 RIDGECREST-2

The 2019 **M** 7.1 Ridgecerest-2, California event was selected because it is a well-documented event with multi-stranded ruptures.

The marginal density plot (Figure A.17) shows strong agreement in the spatial distribution of measurements along the rupture length for all models. As well, the displacement amplitude densities are in strong agreement for all models. Similarly, the results of the pair plots (Figure A.18) show all three models are in strong agreement.

Visual inspection of the differences in aggregated values between models as a function of mapped ruptures (Figure A.19) reveals the largest differences are spatially associated with increased rupture complexity. However, the overall differences are minor, consistent with the plots on Figures A.17 and A.18.

The seed-to-aggregated log ratios (Figure A.20) reveal some consistent trends. The ratios decrease as the seed (single-site measurement) increases (as observed for other events; see discussion at the end of Section 2.1). The CEA and LA ratios are generally lower than the KEA ratios.

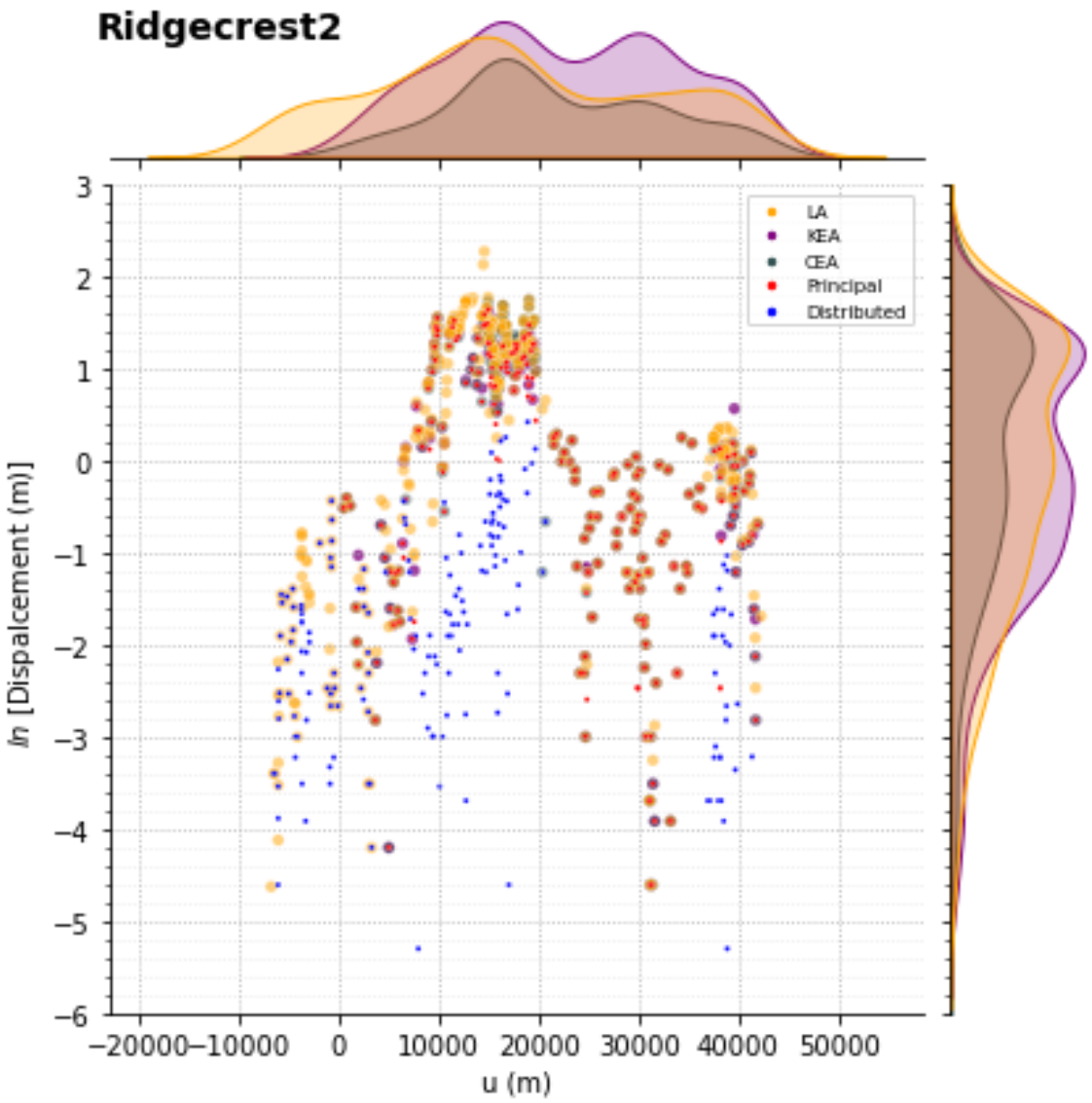

Figure A.17. Displacement measurements (Cumulative, Principal, and Distributed rank) from FDHI Database for 2019 **M** 7.1 Ridgecerest-2, California (FDHI EQ_ID =43) earthquake and aggregated displacements from KEA22, CEA22, and LA22 models. Marginal density plots shown for each model.

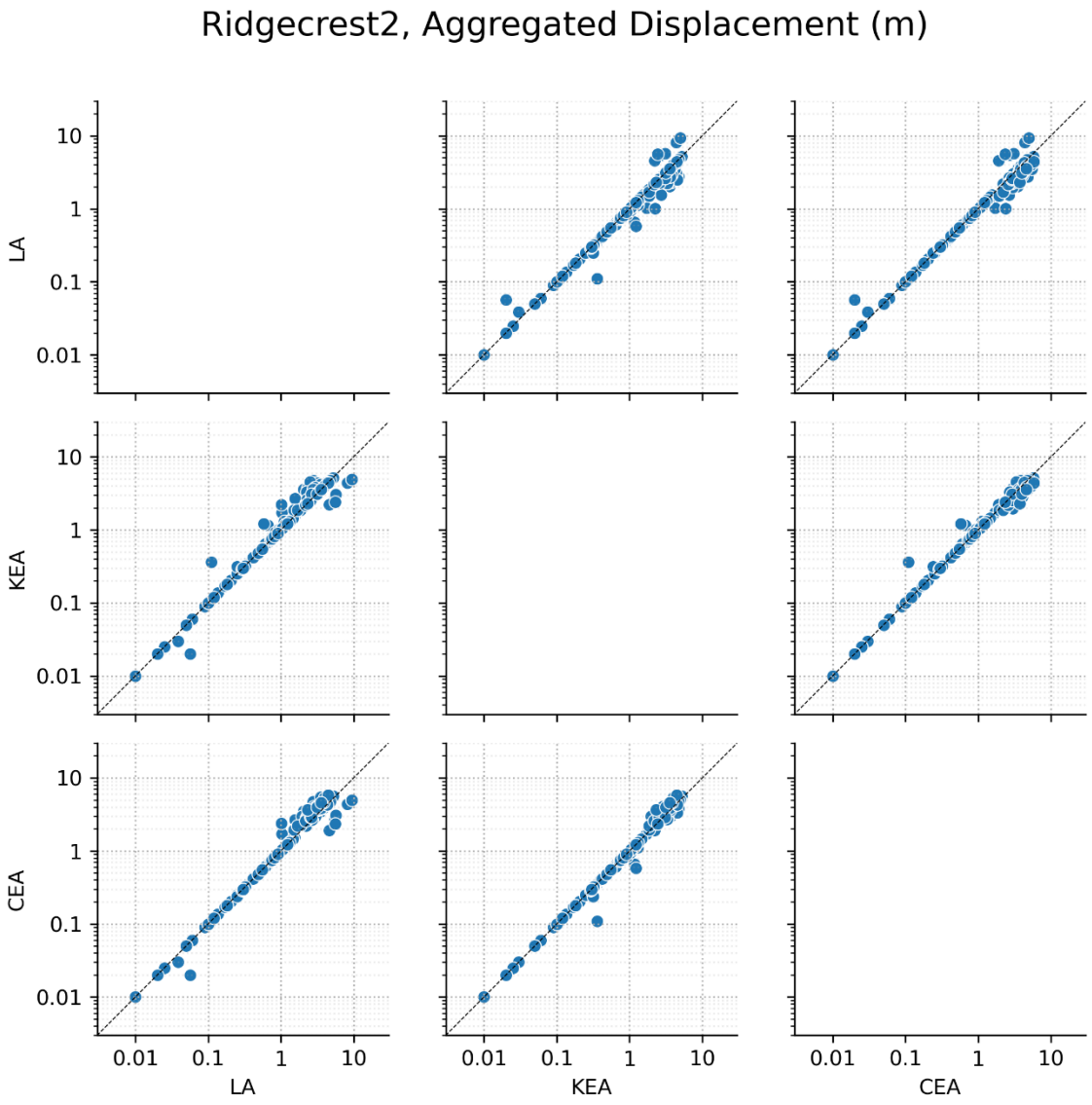

Figure A.18. Comparison of aggregated displacement results for each model (KEA22, CEA22, and LA22) based on measurement site for 2019 **M** 7.1 Ridgecerest-2, California earthquake.

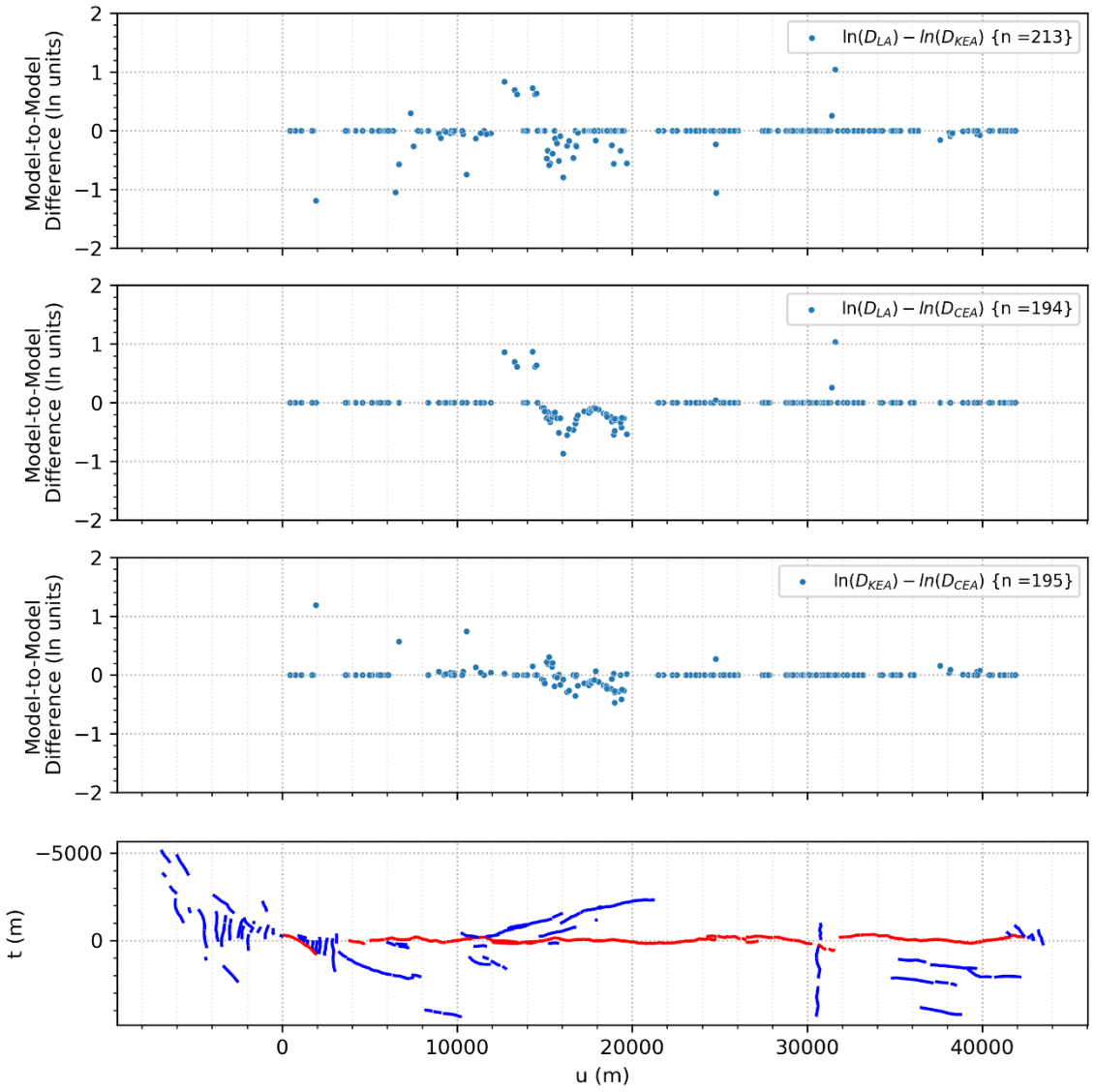

Figure A.19. Comparison of aggregated displacement results for each model (KEA22, CEA22, and LA22) as a function of rupture length for 2019 **M** 7.1 Ridgecrest-2, California earthquake. Principal (red) and distributed (blue) ruptures shown in projected (ECS) coordinated in bottom panel.

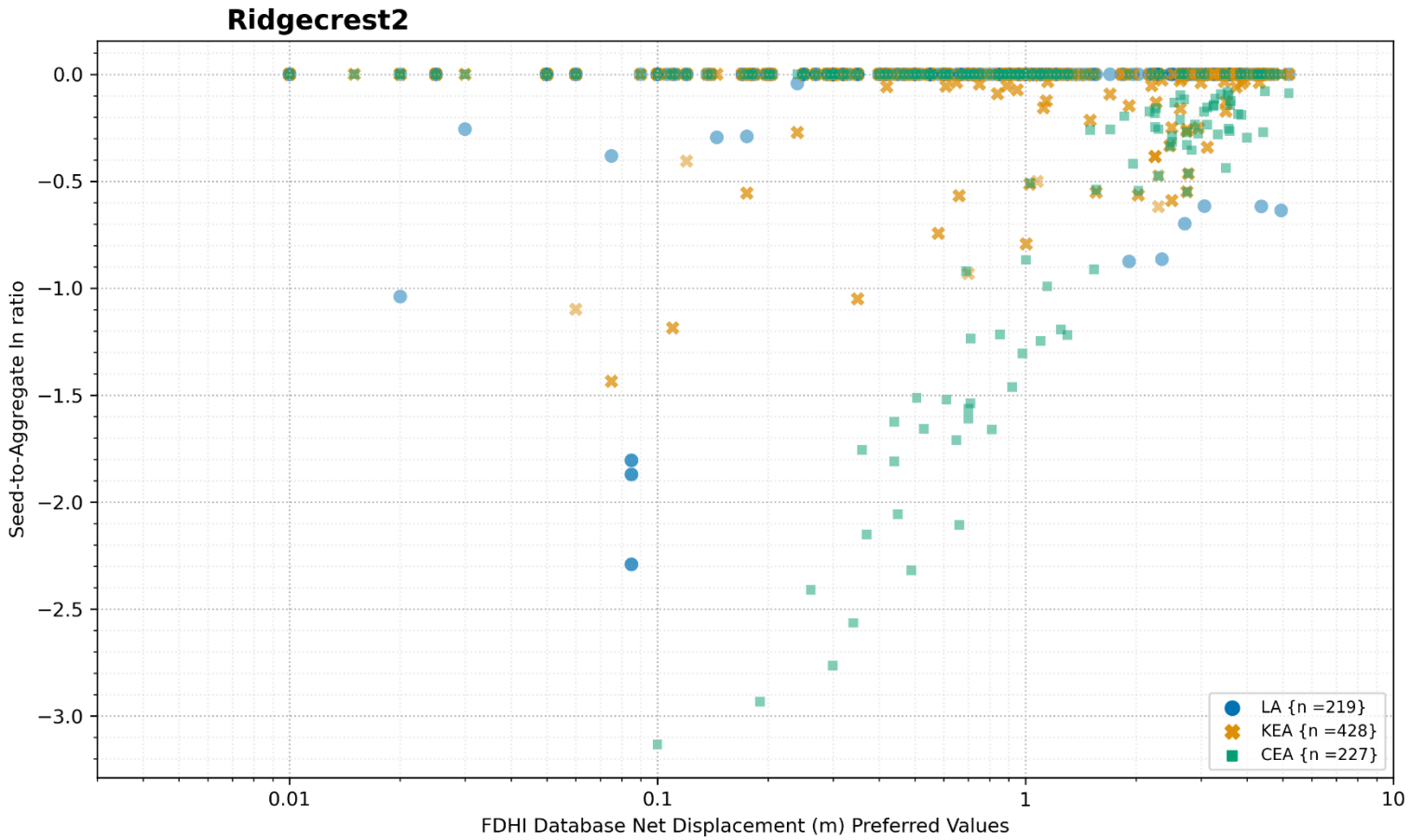

Figure A.20. Comparison of aggregated displacement results for each model (KEA22, CEA22, and LA22) as a function of seed (un-aggregated) measurement for 2019 **M** 7.1 Ridgecerest-2, California earthquake.

2.6 NEFTEGORSK

The 1995 **M** 7.0 Neftegorsk, Russia event was selected the surface rupture patterns are relatively simple.

The marginal density plot (Figure A.21) shows strong agreement in the spatial distribution of measurements along the rupture length for all models. The displacement amplitude densities are also in strong agreement for all models.

Generalized model comparisons can be made from the pair plots (Figure A.22) and are consistent with the trends in the displacement density plots. Where there are differences, the CEA model results are almost always slightly higher.

Visual inspection of the differences in aggregated values between models as a function of mapped ruptures (Figure A.23) reveals the largest differences are spatially associated with the northeast reach of the rupture ($u < 9{,}000$), where the CEA model treated some of the ruptures as principal instead of distributed. We infer that their approach for linear interpolation between measurement sites is contributing to the differences because both the KEA and LA models include distributed measurements. In this area, the CEA results are higher than the other models, and the KEA results are higher than the LA model results.

The seed-to-aggregated log ratios (Figure A.24) reveal some consistent trends. The ratios decrease as the seed (single-site measurement) increases (as observed for other events; see discussion at the end of Section 2.1). The CEA ratios are generally the lowest.

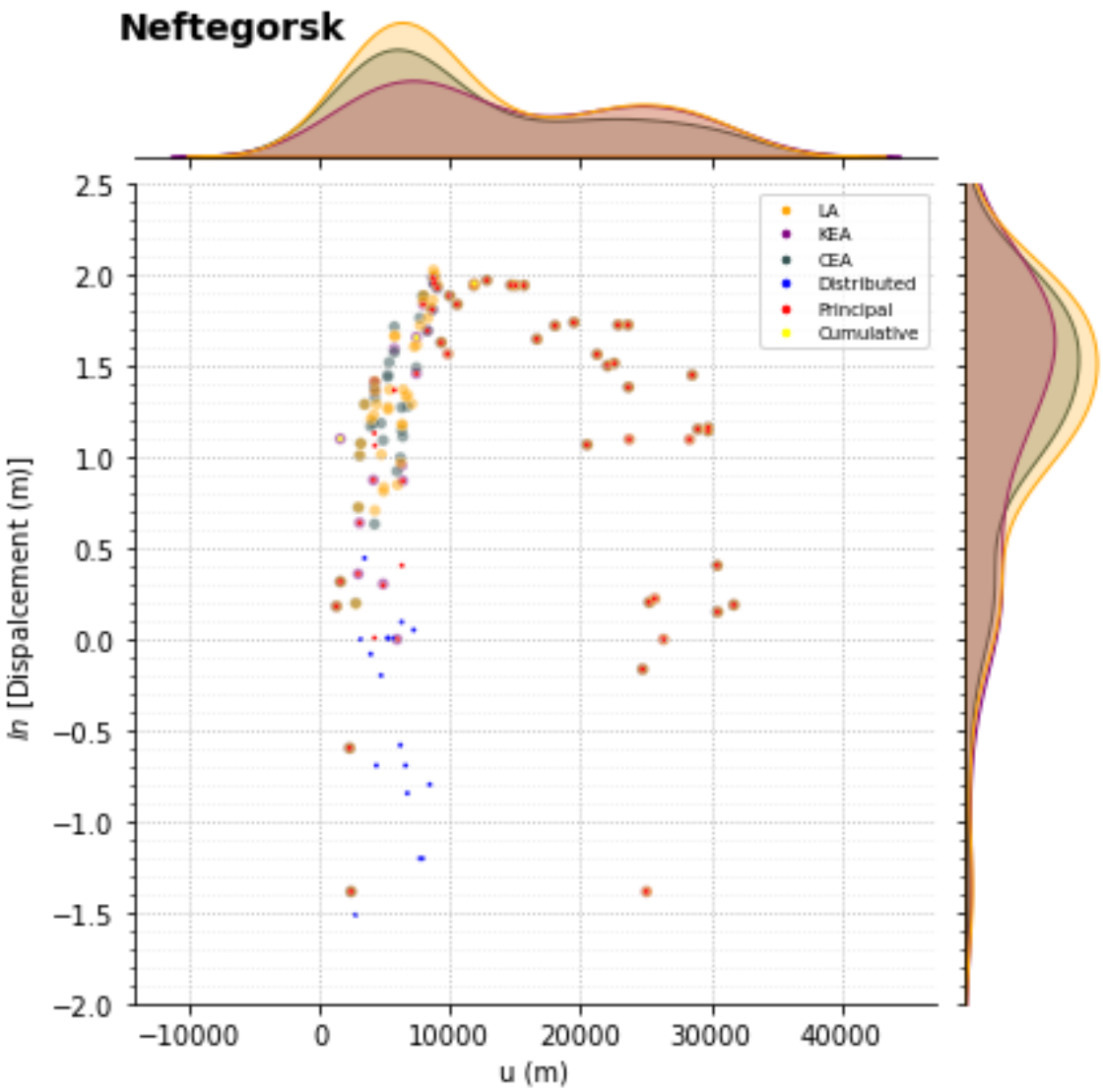

Figure A.21. Displacement measurements (Cumulative, Principal, and Distributed rank) from FDHI Database for 1995 **M** 7.0 Neftegorsk, Russia (FDHI EQ_ID =65) earthquake and aggregated displacements from KEA22, CEA22, and LA22 models. Marginal density plots shown for each model.

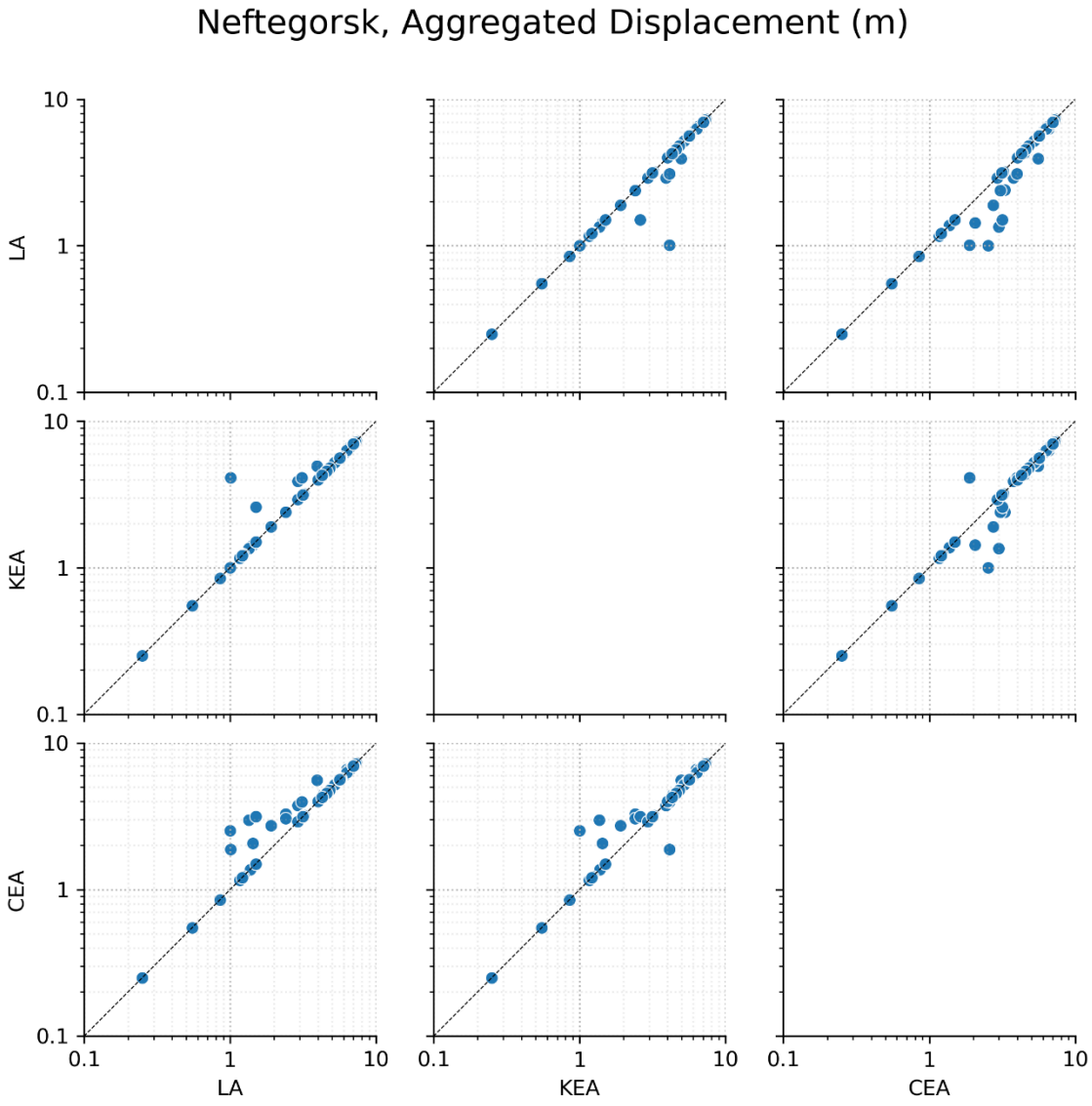

Figure A.22. Comparison of aggregated displacement results for each model (KEA22, CEA22, and LA22) based on measurement site for 1995 **M** 7.0 Neftegorsk, Russia earthquake.

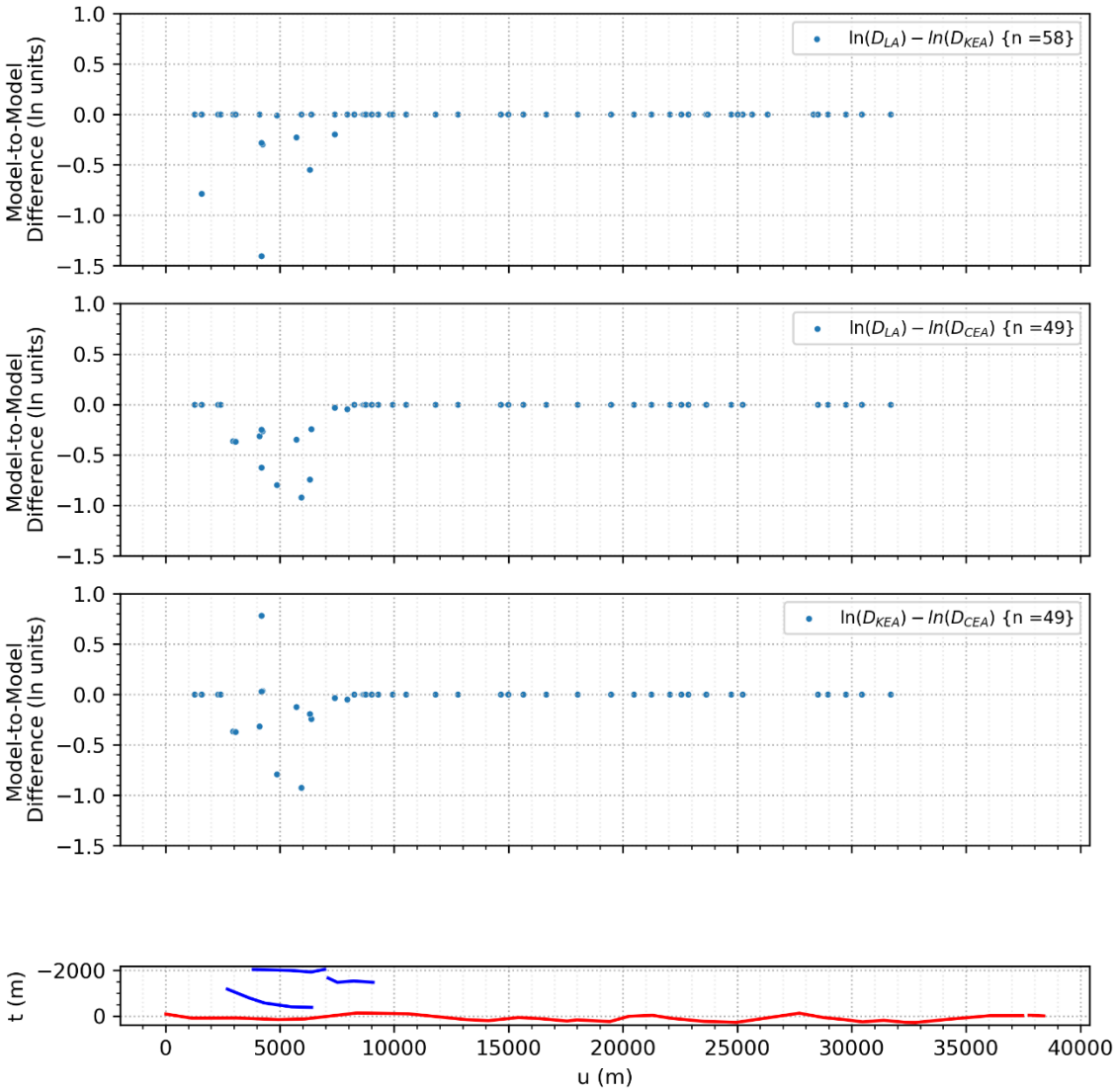

Figure A.23. Comparison of aggregated displacement results for each model (KEA22, CEA22, and LA22) as a function of rupture length for 1995 **M** 7.0 Neftegorsk, Russia earthquake. Principal (red) and distributed (blue) ruptures shown in projected (ECS) coordinated in bottom panel.

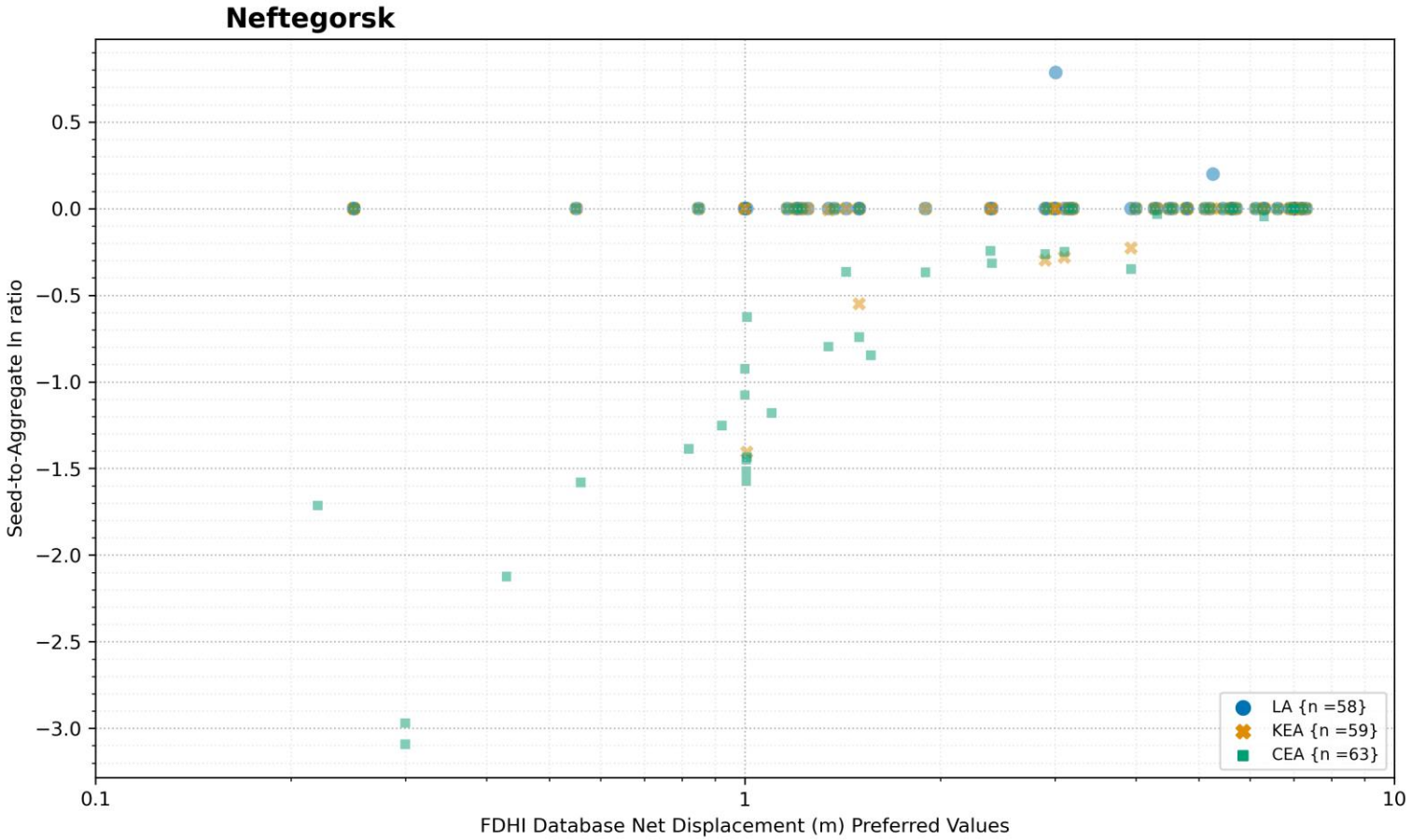

Figure A.24. Comparison of aggregated displacement results for each model (KEA22, CEA22, and LA22) as a function of seed (un-aggregated) measurement for 1995 **M** 7.0 Neftegorsk, Russia earthquake.

3 Summary

A Working Group convened in early 2021 to review results from different aggregation approaches for six earthquakes. This appendix documents comparisons in the form of measurement site and displacement amplitude density distributions, as well direct comparisons of the aggregated displacement amplitudes used in each model for each seed measurement site.

Overall, we find reasonable agreement between the three aggregation models. The differences are generally modest and are due to different methods used to aggregate or sum measurements across (sub)parallel faults or using alternative rank classifications. For example, the CEA22 model does not include distributed displacement measurements in their aggregation, unlike the KEA22 and LA22 models. The selection of a stable response variable (i.e., displacement metric) is a modeler decision and represents a component of epistemic uncertainty. While the KEA22 and LA22 models do include distributed measurements, they use different techniques for aggregating the values, which is a component of modeling epistemic uncertainty. However, based on the findings of this Appendix, the differences in the chosen displacement metric or aggregation methodology are modest.

Appendix B:

Additional Aleatory Variability Comparisons

This Appendix documents additional aleatory variability comparisons to supplement Chapter 5 in the main report. Specifically, logarithmic ratios of 84^{th}-to-median and median-to-16^{th} percentiles are presented as a function of normalized position along rupture for a set of magnitudes to approximate the variability in each model. For the FDMs that use lognormal distributions (KEA22 and PEA11), these ratios are equivalent, and equal to, the standard deviation. For the other models, these ratios are not equivalent and are incomplete descriptions of the aleatory variability. However, taken together, the ratios provide some insight on the skewness in the model. The ratios also provide information about the amount of aleatory variability, where lower ratios indicate less variability.

The ratios are shown on Figures B.1, B.2, and B.3 for strike-slip, reverse, and normal styles of faulting, respectively. For a given model, differences between the left ($84^{th}/50^{th}$) and right ($50^{th}/16^{th}$) panels in each figure are due to skewness in the probability distribution. (Lognornal distributions, such as KEA22 and PEA11, are symmetrical in log space.) Differences for a given model within a panel capture magnitude-dependent aleatory variability. Similarly, changes along the x-axis generally represent location-dependent aleatory variability. An exception is the LA22 model, for which the within-event component is constant, but earthquake size is used in the location scaling; therefore, for the LA22 model, changes along the x-axis reflect magnitude dependence. Aleatory variability in the PEA11 model is constant and not dependent on magnitude or location.

Overall, the ratios are lowest at the rupture midpoint for all magnitudes in all FDMs (except PEA11, for which aleatory variability is constant) and all styles of faulting. Similarly, both ratios are highest at the rupture endpoint in all cases. The ratios also decrease with increasing magnitude for most FDMs and most styles of faulting.

In general, the $84^{th}/50^{th}$ percentile ratios for the new strike-slip models are very similar for $\mathbf{M} \geq 6.8$ at folded normalized locations greater than about 0.2 (Figure B.1). Within-model comparisons between the two percentile ratios highlight the left-skewed probability distributions used in the CEA22 and LA22 models. In these models, higher lower tail ($50^{th}/16^{th}$ ratio) aleatory variability is higher by a factor of about 1.2 to 1.5, depending on the magnitude an location. In most cases, the variability in the new models is reduced relative to the existing PEA11 model.

The $84^{th}/50^{th}$ percentile ratios for the new reverse models are also very similar for all magnitudes (Figure B.2). Three of the models (MEA22, KEA22, and MR11) found no magnitude dependence on the aleatory variability for reverse faults; therefore, the ratios are the same (for a given percentile ratio) regardless of magnitude. The location dependence is minimal in the new models for $x/L > 0.1$, and the MEA22 location dependence approaches constant. Within-model comparisons between the two percentile ratios highlight the left-skewed probability distributions used in the MEA22, LA22, and MR11 models. The variability in the new models is reduced relative to the existing MR11 model.

The $84^{th}/50^{th}$ percentile ratios for the new normal models are generally similar for $\mathbf{M} \geq 7.2$ at folded normalized locations greater than about 0.2 (Figure B.3). The location scaling for both new models is minimal in the new models for $x/L > 0.1$. The variability in the new models is generally reduced relative to the existing YEA03 model for $\mathbf{M} \geq 6.8$.

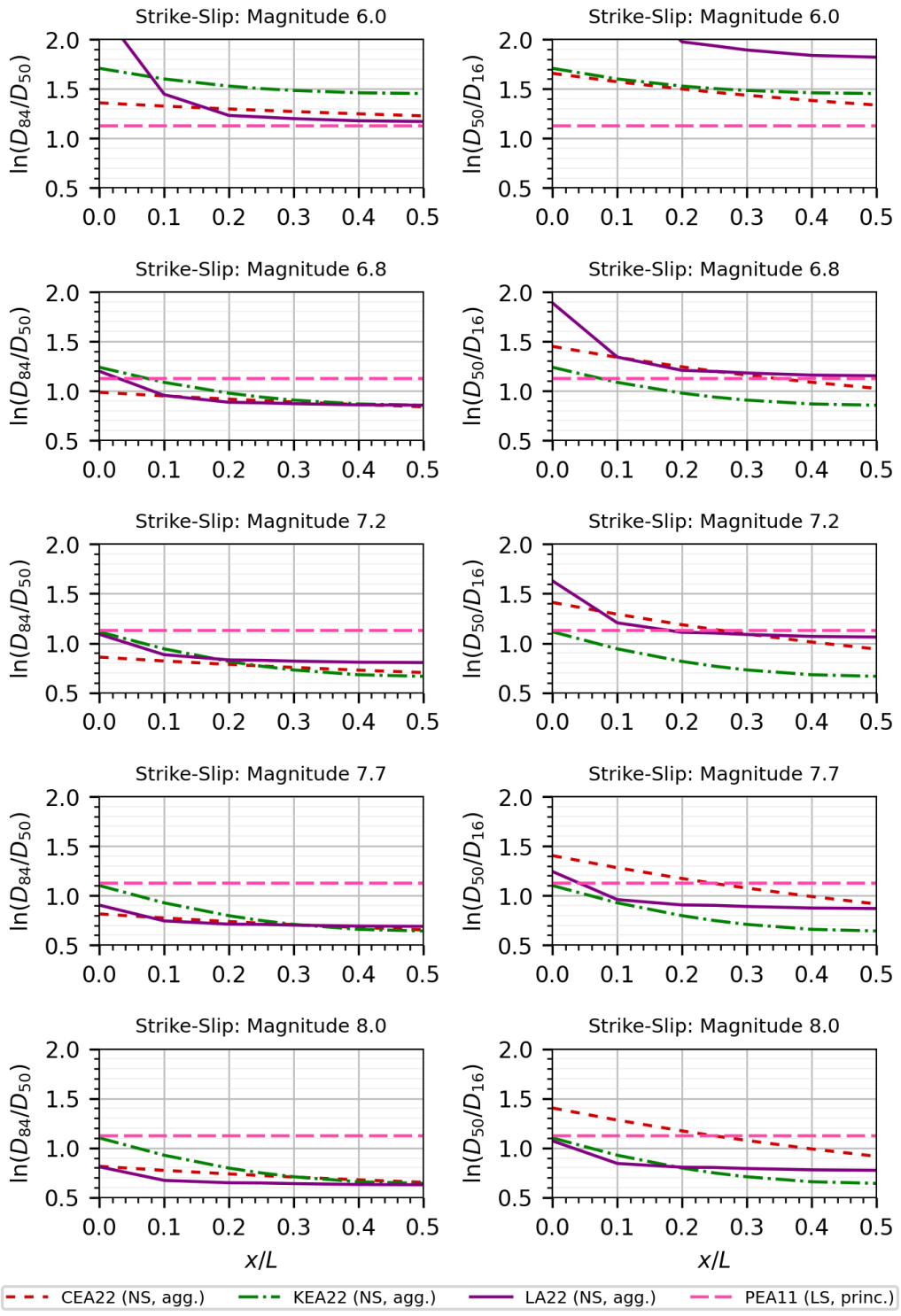

Figure B.1. Comparison of 84th-to-50th (left) and 50th-to-16th (right) percentile displacement ratios for strike-slip faulting. ND = net displacement; LD = lateral displacement; VD = vertical displacement (abbreviations apply to all plots).

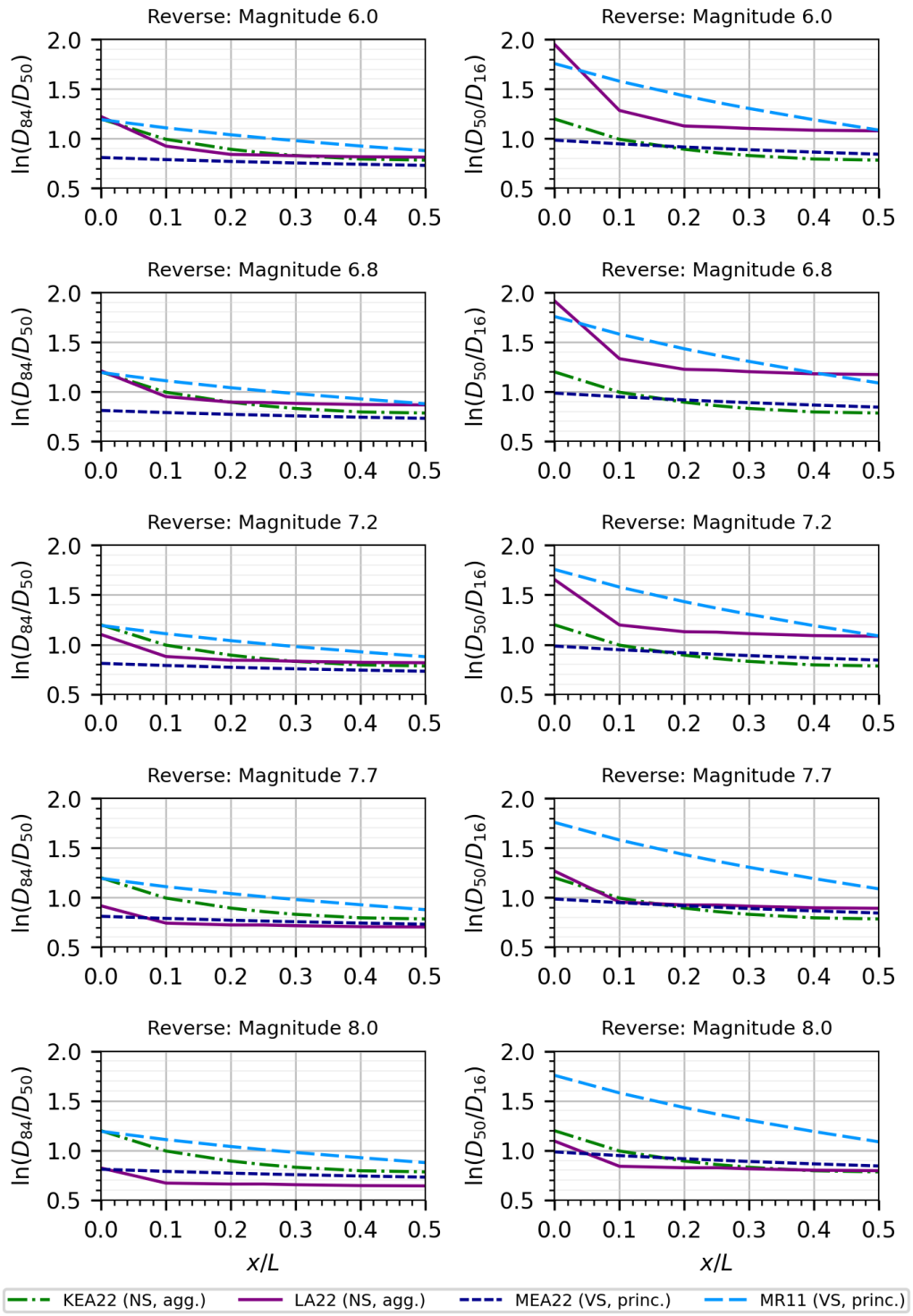

Figure B.2. Comparison of 84th-to-50th (left) and 50th-to-16th (right) percentile displacement ratios for reverse faulting.

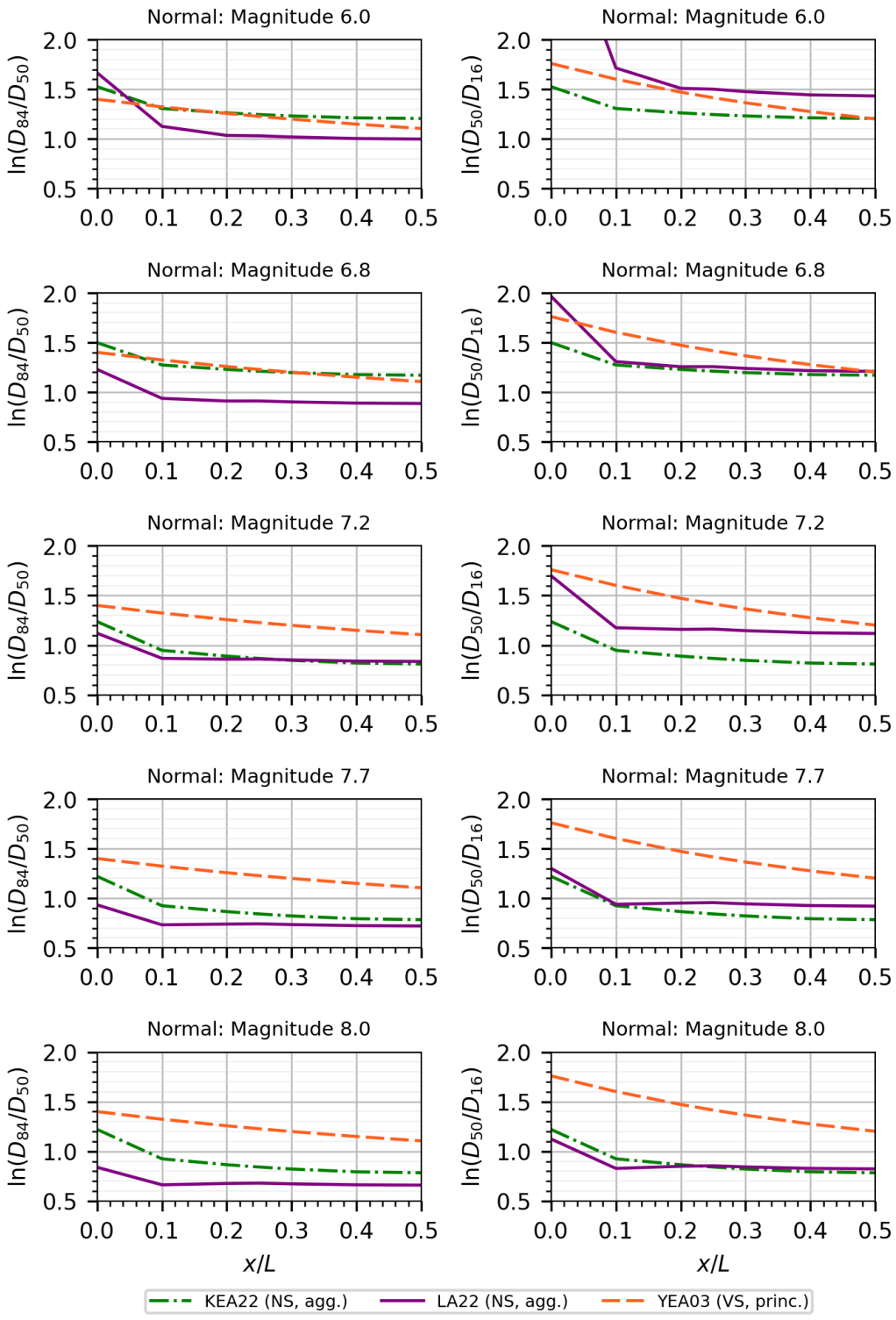

Figure B.3. Comparison of 84th-to-50th (left) and 50th-to-16th (right) percentile displacement ratios for normal faulting.